JOHANNES KEPLER
UNIVERSITY LINZ

Submitted by
Felix Mayr

Submitted at
Linz Institute of Organic Solar Cells,
Institute of Physical Chemistry

Supervisor
Assoc. Univ.-Prof. DI Dr.
Markus Clark Scharber

August 2020

Optical Characterization of Organic and Perovskite Semiconductors by Photothermal Deflection Spectroscopy

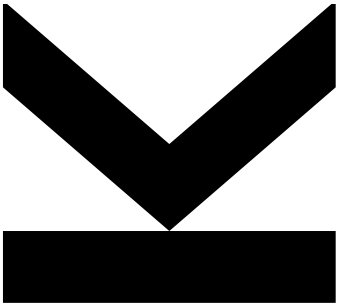

Master Thesis
to obtain the academic degree of
Diplom-Ingenieur
in the Master's Program
Chemistry and Chemical Technology

JOHANNES KEPLER
UNIVERSITY LINZ
Altenbergerstraße 69
4040 Linz, Österreich
www.jku.at
DVR 0093696

Statutory Declaration

I hereby declare that the thesis submitted is my own unaided work, that I have not used other than the sources indicated, and that all direct and indirect sources are acknowledged as references. This printed thesis is identical with the electronic version submitted.

Linz, 05.08.2020
Place, date

Felix Mayr
Signature

Acknowledgements

First and foremost, I want to express my deepest gratitude towards my supervisor Assoc. Prof. DI Dr. Markus Clark Scharber for his great and kind guidance, encouragement and support throughout this work. His immense knowledge and experience, which were reflected by the highly competent and helpful advice on any scientific problem, were essential to overcome any major difficulties during the experimental work for this thesis. I am also grateful for all the interesting discussions.

I also want to express my deep gratitude towards o. Univ.-Prof. Mag. Dr. DDr. h.c. Niyazi Serdar Sariciftci for his helpful advice, encouragement and the great inspiration to pursue science.

Furthermore, I want to particularly thank my colleague and friend Jakob Hofinger for the important preliminary work on the PDS setup, the invaluable help and guidance during the experimental work for the preparation of this thesis and for always taking time for discussion of the measurement results and for helping me with any problem. I very much enjoyed the time working together with him on the measurement setup and all scientific and non-scientific conversations.

I would also like to specifically thank my very good friend Katarina Gugujonovic for her great support and advice on any kind of problem and the numerous very interesting discussions.

I am very grateful to every member of the great team at LIOS for providing such a welcoming and joyful working atmosphere and for the kind support. For the nice time we had together, the great helpfulness and interesting discussions I want to particularly thank Christoph Putz, Hannah Rabl, Hathaichanok Seelajaroen, Christoph Ulbricht and Dominik Wielend. Moreover, I want to thank Bianca Ratzenböck, Munise Cobet, Patrick John-Denk, Gerda Kalab, Gabriele Hinterberger, Birgit Paulik, Sara Gusner and Isolde Wandling for their great help with technical and bureaucratic issues. Additionally, I want to especially thank Bekele Hailegnaw Teklemariam, Anna Jancik Prochazkova, Yolanda Salinas and Elisabeth Leeb for the preparation of the perovskite films and Cigdem Yumusak for the help with the preparation of the CuPc films.

I also want to express my gratitude towards all my friends and study colleagues who made the last few years an unforgettable experience. In this regard I want to especially thank my dear friends Alexander Kirisits, Andreas Koppenberger, Daniel Köpruner, Dominik Kutsam, Karina Mayer, Raphael Mosaner and Magdalena Muhr for being friends to count on, their continuous great support and advice, all the great and fun times we had together and their invaluable help to overcome difficult situations in my life. I also want to particularly thank my fellow students Farzad Abdallah, Gregor Hacker and Patrick Rettenwander for their help and for the good times we had throughout the studies.

My deepest gratitude also goes to my family, particularly my parents and my sister and her family. They have been doing all in their power to support me throughout my whole life and to allow me to pursue my dreams. Without their help and encouragement I would not be where I am today.

Abstract

The detailed characterization of the light absorption properties of materials is of fundamental importance for many applications, including their use in optoelectronic devices, such as solar cells, light-emitting diodes, photodetectors or lasers. While simple and commonly used techniques like spectrophotometry allow straightforward and comparatively easy absorption measurements, they often lack sensitivity and suffer from other drawbacks such as the vulnerability of the measurement accuracy towards light scattering. As a consequence, these techniques are typically not applicable for the investigation of weakly-absorbing optical transitions of materials, such as the sub-bandgap absorption features of semiconductors. These absorption characteristics, however, often yield very important information on the quality of the materials and allow estimation of their performance in optoelectronic devices, which raises the need for the implementation of considerably more sensitive spectroscopic methods. One of the most advantageous techniques to fulfill this task is photothermal deflection spectroscopy (PDS).

In this work, an experimental setup for PDS was assembled. The influences of different measurement parameters, components and optimization measures on the performance of the setup were investigated to maximize the signal-to-noise ratio while providing straightforward handling of the setup in the framework of different measurement tasks. The correct functionality of the setup was validated by comparison of absorption spectra measured for a reference sample with spectra reported for the material in the literature. Furthermore, the built PDS setup was used in conjuction with standard reflectance and transmittance measurements, as well as photoluminescence spectroscopy to investigate different perovskite-based and organic semiconductor materials.

Measurements on highly photoluminescent films of methylammonium lead(II) bromide ($MAPbBr_3$) perovskite nanoparticles and a film of a fluorescent perylene diimide derivative dispersed in a polystyrene matrix demonstrated the reliable application of PDS for the determination of the photoluminescene quantum yields of different materials. The investigation of a mixed-halide methylammonium lead(II) ($MAPbI_{3-x}Cl_x$) perovskite film by PDS allowed the measurement of its band tail absorption and determination of its Urbach energy. Moreover, PDS measurements of the electron donor-acceptor blends PBDB-T-2F:IT-4F, PBDB-T-2F:$PC_{71}BM$ and PTB7-Th:IT-4F, used in high-performance bulk-heterojunction organic solar cells, allowed the measurement of the charge transfer absorption bands arising from electronic interaction of donor and acceptor molecules at their interfaces which play a pivotal role for the device performance. The obtained results clearly demonstrate the usefulness of photothermal deflection spectroscopy for the sensitive characterization of weak optical transitions in semiconductor materials.

Kurzfassung

Die genaue Kenntnis der Lichtabsorptionseigenschaften von Materialien ist von fundamentaler Bedeutung für ihre Anwendung in optoelektronischen Geräten, wie beispielsweise Solarzellen, Leuchtdioden, Photodetektoren oder Lasern. Weitverbreitete Messmethoden wie etwa klassische spektrophotometrische Messungen ermöglichen eine vergleichsweise einfache Messung der Lichtabsorption, zeigen jedoch meist den Nachteil einer eher schlechten Messempfindlichkeit und der starken Anfälligkeit gegenüber Lichtstreuung. Diese Messungen können daher üblicherweise nicht für die Charakterisierung von Absorptionsbanden mit niedrigem Absorptionskoeffizenten, wie etwa die Absorptionseigenschaften von Halbleitern im spektralen Bereich unterhalb ihrer Bandlückenenergie, eingesetzt werden. Da diese Absorptionseigenschaften jedoch wichtige Aufschlüsse über die Materialqualität und die Eignung der Materialien für bestimmte optoelektronische Anwendungen geben, besteht ein hoher Bedarf für deren Charakterisierung durch den Einsatz empfindlicherer Absorptionsmessmethoden. Eine vorteilhafte Messmethode für hochempfindliche Absorptionsmessungen stellt die photothermische Ablenkungsspektroskopie (PDS) dar.

Im Zuge dieser Masterarbeit wurde ein Messaufbau zur Durchführung von PDS zusammengesetzt. Die Einflüsse verschiedener Messparameter, der Variation von Komponenten des Aufbaus sowie verschiedener Optimierungsmaßnahmen wurden untersucht, um das Signal-Rausch-Verhältnis des Setups zu optimieren und eine problemlose Durchführung von Messungen zu ermöglichen. Die korrekte Funktion des Messaufbaus wurde mittels eines Vergleichs des experimentell ermittelten Absorptionsspektrums eines Referenzmaterials mit Spektren aus der Literatur verifiziert. Der PDS Messaufbau wurde anschließend in Verbindung mit spektrophotometrischen Reflexions- und Transmissionmessungen, sowie Photolumineszenzspektroskopie zur optischen Charakterisierung von verschiedenen Perowskit-basierten und organischen Halbleitermaterialien eingesetzt.

Anhand von Messungen an stark photolumineszierenden Filmen von Methylammoniumblei(II)-bromid ($MAPbBr_3$)-Perowskitnanopartikeln und eines Perylendiimid-basierten Fluoreszenzfarbstoffs, dispergiert in einer Polystyrolmatrix, konnte die Anwendung des PDS-Aufbaus zur Bestimmung der Photolumineszenzquantenausbeute an verschiedenen Materialien gezeigt werden. PDS-Messungen an Mischhalogenid-Methylammoniumblei(II)-Perowskitfilmen ($MAPbI_{3-x}Cl_x$) erlaubten die Charakterisierung des Absorptionsprofils der Bandkante und die Bestimmung der Urbach-Energie des Films. Weiters wurden Messungen an den Donor-Akzeptor-Mischungen PBDB-T-2F:IT-4F, PBDB-T-2F:$PC_{71}BM$ und PTB7-Th:IT-4F, welche in hocheffizienten organischen Solarzellen mit Bulk-Heteroübergang eingesetzt werden, durchgeführt. Dabei konnten die schwachen Ladungstransfer-Absorptionsbanden gemessen werden, welche durch elektronische Wechselwirkung der Donor- und Akzeptormoleküle an deren Grenzflächen entstehen und deren Eigenschaften eine essentielle Rolle für die Leistungsfähigkeit der entsprechenden organischen Solarzellen spielen. Die gemessenen Ergebnisse demonstrieren die erfolgreiche Anwendung der photothermischen Ablenkungsspektroskopie für die Charakterisierung von schwachen optischen Übergängen in Halbleitermaterialien.

Contents

List of Symbols and Abbreviations

List of Symbols

$h = 4.136 \times 10^{-15}\,\mathrm{eV\,s}$	Planck constant
$c = 2.998 \times 10^{8}\,\mathrm{m\,s^{-1}}$	Speed of light in vacuum
i	Imaginary unit
E	Photon energy
λ	Photon wavelength
n'	Complex refractive index
n	Real part of the complex refractive index
k	Extinction coefficient
Φ	Radiant power of light
R	Reflectance
T	Transmittance
A	Absorptance
α	Absorption coefficient
Q	Heat per unit time
ΔT	Temperature difference
ω	Pump beam modulation frequency
r	Pump beam radius
z_0	Probe beam-sample offset in transverse PDS
L	Sample-detector distance in transverse PDS
Θ	Deflection angle
d	Film thickness
$\frac{dn}{dT}$	Thermo-optical coefficient
μ_t	Thermal diffusion length
μ_α	Optical absorption length
ρ	Density
κ	Thermal conductivity
C	Specific heat
η_NR	Quantum yield of non-radiative recombination
η_PL	Photoluminescence quantum yield
$\overline{E}_\mathrm{PL}$	Mean emission photon energy of photoluminescence
S	Deflection signal
B, B'	Proportionality constants

E_{g}	Bandgap energy
E_{U}	Urbach energy
E_{CT}	Energy difference between ground state and charge-transfer state
V_{OC}	Open-circuit voltage
$q = 1.6022 \times 10^{-19}\,\mathrm{C}$	Elementary charge
M_{W}	Mass average of the molar mass
f	Focal length
I	Current
V	Voltage
γ_{PD}	Photodiode responsivity (in A W^{-1})
C_{BS}	Beamsplitter correction factor
X_{Diff}	x-axis difference signal of quandrant photodiode
Y_{Diff}	y-axis difference signal of quandrant photodiode
SUM	Total voltage signal of quandrant photodiode
Z_{f}	Transimpedance gain
τ	Lock-in amplifier measurement time constant
N	Number of averaged data points at the lock-in amplifier
t_1, t_2	Waiting times between readouts at the lock-in amplifier
X	Lock-in amplifier in-phase component of the deflection signal
Y	Lock-in amplifier quadrature component of the deflection signal
S_{Corr}	Corrected deflection signal
θ	Deflection signal phase
a	Relative absorptance
σ	Standard deviation of a Gaussian distribution

List of Abbreviations

A	Acceptor in bulk-heterojunction organic solar cells
AOTF	Acousto-optic tunable filter
BHJ	Bulk-heterojunction
CT	Charge-transfer
CuPc	Copper(II) phthalocyanine
D	Donor in bulk-heterojunction organic solar cells
DMF	N,N-Dimethylformamide
DMSO	Dimethyl sulfoxide
EQE	External quantum efficiency in solar cells
FWHM	Full width at half maximum
IQE	Internal quantum efficiency in solar cells

IT-4F	3,9-bis(2-methylene-((3-(1,1-dicyanomethylene)-6,7-difluoro)-indanone))-5,5,11,11-tetrakis(4-hexylphenyl)-dithieno[2,3-d:2',3'-d']-s-indaceno[1,2-b:5,6-b']dithiophene
ITO	Indium tin oxide
LIA	Lock-in amplifier
$MAPbBr_3$	Methylammonium lead(II) bromide
$MAPbI_{3-x}Cl_x$	Mixed-halide methylammonium lead(II) perovskite
OD	Optical density
OSC	Organic solar cell
P3HT	Poly(3-hexylthiophene)
PBDB-T-2F	Poly[(2,6-(4,8-bis(5-(2-ethylhexyl-3-fluoro)thiophen-2-yl)-benzo[1,2-b:4,5-b']dithiophene))-alt-(5,5-(1',3'-di-2-thienyl-5',7'-bis(2-ethylhexyl)benzo[1',2'-c:4',5'-c']dithiophene-4,8-dione))]
$PC_{61}BM$	[6,6]-phenyl-C61-butyric acid methyl ester
$PC_{71}BM$	[6,6]-phenyl-C71-butyric acid methyl ester
PDI	*N*,*N*'-Bis(2,6-diisopropylphenyl)-3,4,9,10-perylene diimide
PDS	Photothermal deflection spectroscopy
PE	Polyethylene
PEDOT	Poly(3,4-ethylenedioxythiophene)
PL	Photoluminescence
PLE	Photoluminescence excitation
PLQY	Photoluminescence quantum yield
PMMA	Poly(methyl methacrylate)
PS	Polystyrene
PSD	Position sensing detector
PSS	Polystyrene sulfonate
PTB7-Th	Poly[4,8-bis(5-(2-ethylhexyl)thiophen-2-yl)benzo[1,2-b;4,5-b']dithiophene-2,6-diyl-alt-(4-(2-ethylhexyl)-3-fluorothieno[3,4-b]thiophene-)-2-carboxylate-2-6-diyl]
PTFE	Poly(tetrafluoroethylene)
rpm	revolutions per minute
SNR	Signal-to-noise ratio

List of Figures

List of Tables

1. Introduction

1.1. Interaction of Materials with Light

Since the development of the first commercial light-emitting diodes in the early 1960s, the usage and relevance of optoelectronic devices has increased tremendously [1]. Nowadays, these devices are an ubiquitous part of modern society and essential components of many indispensable technologies such as telecommunication, data storage, domestic lighting, displays and numerous other applications [1, 2]. The working principle of optoelectronic instruments, such as photovoltaic devices, light-emitting diodes (LEDs), photodetectors, optical modulators and laser diodes is based on the interaction of light with solids, primarily semiconductor materials [2]. Thus, the investigation and understanding of the optical properties of semiconductors is essential for the development and optimization of these devices and can yield insight into the basic physical properties of the materials, such as the fundamental bandgap, band structure, energy levels and concentrations of defect states and impurities, as well as properties of excitations such as excitons, plasmons and phonons [2, 3].

The principal modes of interaction of incident light with an optically homogeneous solid medium are reflection, transmission and absorption and are governed on a macroscopic level by the complex refractive index of the material, displayed in eq. (1.1), where n is the real part of the refractive index, k is the extinction coefficient and i is the imaginary unit, as can be derived from the Maxwell equations for the propagation of electromagnetic waves [2, 4, 5].

$$n' = n - ik \tag{1.1}$$

The ratios of the radiant power of reflected, transmitted and absorbed light, Φ_R, Φ_T and Φ_A, respectively, to the radiant power of the incident light Φ_i as shown in eq. (1.2) define the fundamental spectroscopic quantities reflectance R, transmittance T and absorptance A of a finite medium [6].

$$R = \frac{\Phi_R}{\Phi_i} \qquad T = \frac{\Phi_T}{\Phi_i} \qquad A = \frac{\Phi_A}{\Phi_i} \tag{1.2}$$

Due to the conservation of energy, the sum of the three quantities must amount to a value of one, as stated in eq. (1.3) [2].

$$1 = R + T + A \tag{1.3}$$

In addition to the three described processes, scattering of light can take place at optical inhomogeneities in the medium via different mechanisms including inelastic scattering by time-

dependent inhomogeneities such as acoustic phonons (Brillouin scattering) and optical phonons (Raman scattering) and elastic scattering at time-independent, local inhomogeneites such as nanostructures, defects or precipitates of comparable size (Mie scattering) or smaller size (Rayleigh scattering) than the wavelength of light [2, 4]. The discussed material interactions with light are typically dependent on the photon energy of the incident light and can be probed by a vast number of different spectroscopic techniques [2].

1.1.1. Light Absorption Measurements

Among the described processes, light absorption is one of the most frequently investigated optical properties of materials. The absorption of light with a wavelength λ in a homogeneous material is governed by the attenuation of the electromagnetic wave in the medium and its radiant power $\Phi(x)$ at the position x along its propagation path depends on its initial power Φ_0 at entrance in the medium and is related to the extinction coefficient k of the medium as described by Lambert's law, shown in eq. (1.4) [4, 7].

$$\Phi(x) = \Phi_0 \, e^{-\frac{4\pi k}{\lambda} x} \tag{1.4}$$

From the exponent in eq. (1.4) the absorption coefficient α, which is used as a fundamental parameter to describe the light absorption properties of a material, is derived according to eq. (1.5) [4, 7].

$$\alpha = \frac{4\pi k}{\lambda} \tag{1.5}$$

The light absorption properties of semiconductors are typically examined in the visible and near-visible regimes of the electromagnetic spectrum [4]. In the photon energy range of the UV, Vis and NIR spectrum, light absorption in semiconductors can occur through different electronic transitions such as band-to-band transitions, excitons, free carrier absorption or absorption by defects [2, 4]. Depending on the energy of the absorbed light, the resulting excited state possesses a higher potential energy (energy of the transition) than the ground state and often excess kinetic energy, which is typically dissipated by fast thermalization, releasing the excess energy as heat [2, 8]. The excess potential energy of the excited state is typically released either analogously by thermal relaxation and generation of heat, or by radiative recombination under emission of a photon (photoluminescence, PL) (see Fig. 1.1) [8].

Based on these relaxation pathways, different spectroscopic techniques can be used to probe the wavelength-dependent light absorption of materials. The three principal measurement methods to determine the absorptance A, namely reflectance and transmittance measurements (spectrophotometry), emissometry and calorimetry are schematically shown in Fig. 1.1 [8, 9].

The determination of the absorptance of a sample via R & T measurements is a simple and fast method that can be performed on conventional UV/Vis/NIR spectrophotometers [8]. The method suffers, however, from a limited sensitivity with minimal measureable absorptance values of typically $10^{-2} - 10^{-3}$ [9–12]. Limiting factors of the accuracy of the method are its

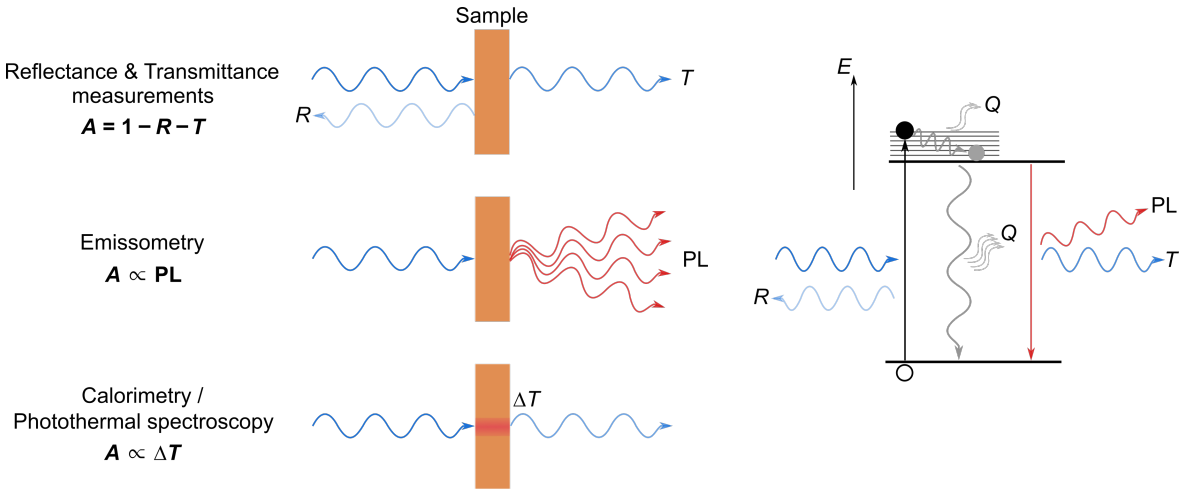

Figure 1.1. Schematic overview of different general approaches for the measurement of the light absorption spectrum of a sample showing the quantity which is measured in each method. The right panel schematically shows the electronic transitions which the methods are based on. Q refers to heat generated via thermal relaxation. Figure adapted from ref. [8].

sensitivity towards light scattering and spurious reflections [8, 12], which also restricts its usefulness for absorption measurements of samples with optical inhomogeneities such as a high surface roughness [11, 13]. The sensitivity limit typically restricts the use of spectrophotometry for the measurement of optical transitions with low absorption coefficients. Thus, significantly more sensitive absorption measurement techniques are required for important tasks such as the characterization of absorption losses in transparent optical coatings [10, 14], spectroscopic trace chemical detection [15] and measurements of sub-bandgap absorption features of semiconductors, including the absorption from band tail states (e.g. determination of the Urbach energy) or defects [12, 16, 17] and the characterization of trap states or charge-transfer interactions in organic semiconductors [18, 19].

Emissometry uses the light emission from a sample as a measure for its absorption properties. This can be conducted by measurement of the thermal radiation emitted from the sample in thermal equilibrium at a known temperature [9] or by measurement of its photoluminescence [21–23]. Since the thermal emission of materials at room temperature is typically in the mid-infrared with a maximum at wavelengths of ca. 10 µm and quickly declines towards the Vis/NIR regime [9], it is not applicable for the UV/Vis/NIR regions. Photoluminescence measurements can be used to deduce the absorption spectra of materials in these spectral regions in two ways:

- Quantitative measurement of the photoluminescence at a fixed excitation energy and calculation of the relative absorptance spectrum from the emitted radiant power density according to formulas given in refs. [23, 24].
- Measurement of the photoluminescence excitation (PLE) spectrum at a fixed emission energy. The PLE spectrum of a material reflects its absorptance spectrum with the photoluminescence quantum yield (PLQY) as a proportionality factor [22, 25]. A direct proportionality over a certain spectral range is thus provided if the PLQY of the material is constant versus the excitation photon energy, as is generally implied for materials by the widely accepted

Table 1.1. Overview of different photothermal absorption measurement techniques with the corresponding measured sample property which reflects the change of a thermodynamic parameter as a result of the temperature increase upon optical heating [20].

Parameter	Measured property	Measurement technique
Temperature	Temperature	(Photothermal) Calorimetry
	Themal radiation	Photothermal radiometry
Pressure	Acoustic wave	Photoacoustic spectroscopy (PAS)
Density	Refractive index	Photothermal lens spectroscopy (PTL)
		Photothermal deflection spectroscopy (PDS)
		Photothermal interferometry
	Surface deformation	Photothermal mirror (PTM)

rule of Vavilov (also known as Kasha-Vavilov rule) [26, 27].

While the absorption measurements based on PL potentially offer a very high sensitivity, with reported absorption coefficients of down to 10^{-14} cm^{-1} [24], they can only be used to probe states which recombine radiatively, such as band-to-band transitions in semiconductors, and are not generally applicable to all optically active transitions [8, 21].

Calorimetric or photothermal techniques are based on the measurement of the generated heat and the corresponding thermal changes in a material by the absorption of light and subsequent thermal relaxation [9, 20]. The measurement methods are typically based on the direct measurement of temperature change or the measurement of some quantity related to the temperature change of the sample [8, 9, 20]. Direct calorimetric absorption measurements can be conducted by attaching a thermocouple to the sample and directly measuring the temperature change under illumination at a certain photon energy. However, the direct method suffers from several disadvantages such as the requirement for high light power for sensitive measurements, accurate control of ambient temperature and careful alignment to avoid the incidence of scattered light on the temperature sensor [9]. Other photothermal methods involve measurement of the changes in pressure or density of the surrounding medium or the sample itself upon temperature change. An overview of the measureable thermal parameter changes induced by the temperature increase and the related meaurement techniques is given in Table 1.1. Most photothermal spectroscopic methods, such as PAS, PTM, PTL and PDS are typically insensitive towards light scattering as only absorbed light contributes to the photothermal signal and can routinely detect temperature changes as small as 1 μK and thus offer high measurement sensitivity [20, 28, 29]. Additionally, in comparison to PL-based techniques the measureable optical transitions are not limited to those which show radiative recombination.

Among the photothermal methods, photothermal deflection spectroscopy is one of the most frequently used techniques as it offers high versatility for different types of samples, very high sensitivity with detectable absorptance values as low as $10^{-6} - 10^{-7}$ and an often simpler alignment in comparison with other photothermal spectroscopic techniques [10, 17, 20, 28]. Thus, in this work the implementation of an experimental setup for PDS was carried out to allow the sensitive investigation of the absorption characteristics of different semiconductor materials.

1.2. Photothermal Deflection Spectroscopy

The operation principle of photothermal deflection spectroscopy (PDS) is based on the absorption of light (pump light) by a sample material and the thermal relaxation of the thereby generated excited states, which induces a local temperature gradient in the sample due to the released heat. Since the refractive index of a material is a function of temperature, the photothermally induced temperature gradient leads to a refractive index gradient in the irradiated region of the sample and, to a certain extent, in the surrounding medium due to heat transfer [20, 28]. A second light beam, referred to as probe beam, is then used to probe the gradient by measuring the deflection of its propagation direction due to the refractive index differences [30]. The deflection is measured on a position-sensitive detector and is proportional to the absorptance of the sample [8]. The use of frequency-modulated pump light allows the implementation of lock-in detector for the measurement of the beam deflection, which drastically filters noise and heavily increases the sensitivity of PDS [8, 11]. By using a spectrally tunable pump light source, the pump light wavelength-dependent beam deflection can be measured and used to determine the absorption spectrum of the investigated sample.

1.2.1. PDS Setup Configurations

Two different experimental configurations are most commonly used for the execution of PDS measurements, namely collinear and transverse photothermal deflection spectroscopy.

In the collinear geometry, as shown in Fig. 1.2 (a), the pump and probe beams are arranged in a way that they are nearly parallel to each other and show a large degree of overlap within the sample [28, 31]. Practically, such a geometry can be realized by using a beamsplitter on which the beams are incident on opposite sides [31] or by using suitable optical filters [15, 32]. In other reported collinear PDS setups larger angels of up to 30° between pump and probe beam were used [10, 14, 33]. In this measurement configuration, the refractive index gradient is generated and probed inside the sample [8]. Thus, the tolerance towards different sample properties is limited as the sample has to be sufficiently transparent at the wavelengths of the pump and probe beams [8]. The advantage of the collinear PDS configuration is the typically large interaction length of pump

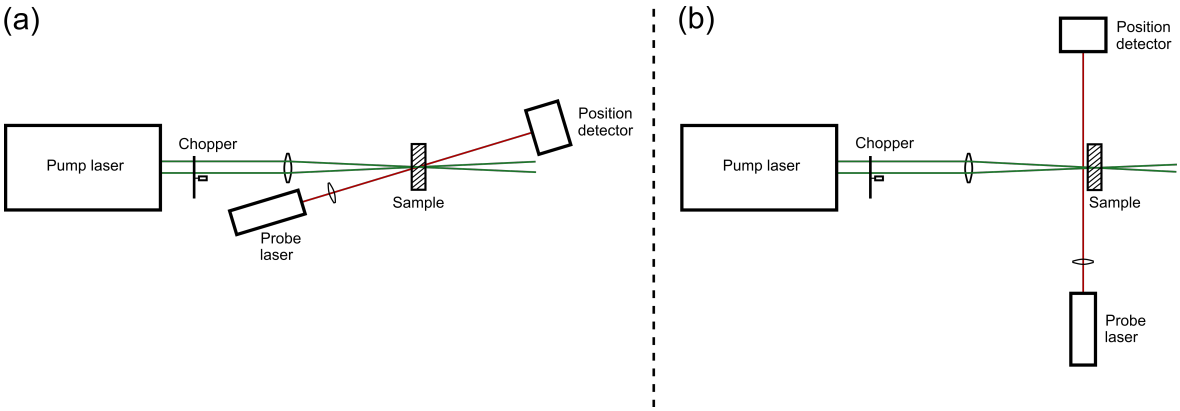

Figure 1.2. Simplified schematic representation of the two most commonly used configurations for photothermal deflection spectroscopy: **(a)** collinear PDS and **(b)** transverse PDS. Adapted from ref. [28].

and probe beam, resulting in a higher achievable deflection signal [31]. Additionally, collinear PDS can be used for depth profiling of the absorption properties of the sample [10]. The collinear configuration is typically used for PDS measurements of solutions or dispersions [15, 31, 34], (semi-)transparent bulk solids [10, 32, 33] and gases [35].

In the transverse PDS configuration, shown in Fig. 1.2 (b), pump and probe beam are arranged perpendicular to each other. The probe beam is typically aligned parallel to the sample with a very small offset to the sample surface which is photothermally heated by the incident pump beam [28]. Thus, the refractive index gradient is probed in a thin layer of the medium surrounding the sample adjacent to its surface. As a consequence, the measureable deflection is also highly dependent on the properties of the surrounding medium. In transverse PDS the sample materials are typically immersed in a transparent fluid with a high thermo-optical coefficient dn/dT (deflection fluid) to amplify the refractive index gradient [8, 20]. In comparison to the collinear configuration, transverse PDS is suitable for the analysis of opaque samples and has a high tolerance towards different sample properties and shapes. Transverse PDS has been used in the analysis of solutions [36, 37] and bulk solid materials [30, 38]. Predominantly, however, it is used for the investigation of thin films [8, 16, 19, 39, 40].

Due to its high versatility and perfect suitability for the analysis of thin films, the transverse measurement configuration was chosen for the PDS setup used in this work.

1.2.2. Theoretical Principles

1.2.2.1. Theoretical Model for Transverse PDS

A detailed theoretical description of the temperature distribution in a fluid upon frequency-modulated optical heating of an adjacent solid material was first developed by Rosencwaig and Gersho in 1976 for a simple one-dimensional model [41]. The model was used for the description of photoacoustic spectroscopy but is applicable to PDS as well. The first general description of the theoretical basics of collinear and transverse photothermal deflection spectroscopy on the basis of a three-dimensional model was developed by Jackson *et al.* in 1981 [28].

The derivation is based on a 3-D model with the three regions transparent deflection medium

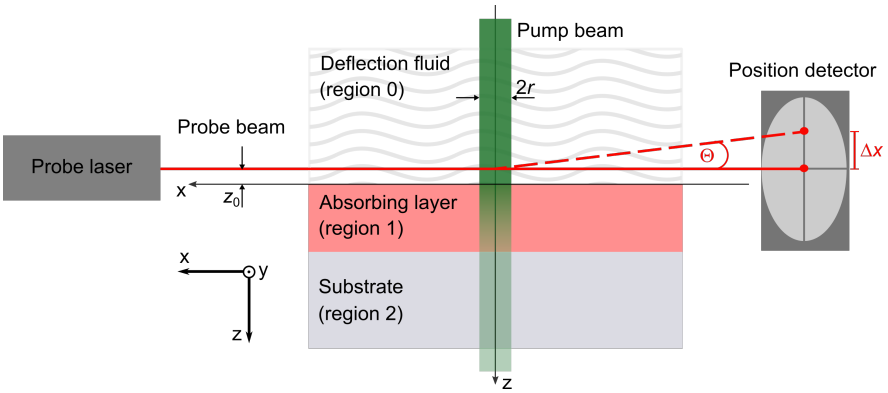

Figure 1.3. Schematic representation of the 3-d model used for the derivation of a theoretical model for transverse PDS by Jackson *et al.* [28]. Θ is the deflection angle, Δx is the distance the probe beam spot moves on the position detector due to the deflection, z_0 is the probe beam-sample offset and r is the pump beam radius.

(region 0), absorbing layer (e.g. thin film; region 1) with thickness d and transparent substrate (region 2), as shown in Fig. 1.3. All three regions are assumed to extend infinitely in the x- and y-direction, which is a valid approximation since typically the radial sample dimensions are much larger than the pump beam diameter and the thermal diffusion lengths of the materials [28]. For the derivation it is additionally assumed that: (i) all absorbed light is converted into heat (photoluminescence is neglected); (ii) the relative temperature change due to the absorbed light is sufficiently small to assume a linear change of refractive index with temperature; (iii) pump and probe beam have ideal Gaussian profiles [8, 28, 41]. In the first step, the periodically varying temperature distribution, due to the deposited heat per unit time, Q, is determined. The heat is induced by absorption of the pump light, modulated with the frequency ω, in region 1. The temperature distribution is determined by solving the set of heat diffusion equations for all three regions with the boundary conditions of equal temperature and equal heat flux at the interfaces of the regions [28, 41]. From the temperature distribution function and the equation for the propagation of the probe beam through a medium with position-dependent refractive index, an equation for the periodic angular deviation Θ of the probe beam from its path can be derived [28]. For the full derivation the interested reader is pointed to ref. [28]; in the following only some important proportionalities that can be extracted from the developed model and are relevant for the experimental design of a transverse PDS setup, are discussed and are shown in eq. (1.6) [17, 28].

$$\Theta \propto \Phi_0 \left(1 - e^{-\alpha d}\right) \frac{1}{n_0} \frac{dn}{dT} \frac{1}{r} e^{-|z_0|\, \mu_{\mathrm{t}_0}^{-1}} e^{i\omega t} \tag{1.6}$$

Here, μ_{t_0} represents the thermal diffusion length of the deflection fluid which is dependent on ω and the thermal conductivity κ_0, density ρ_0 and specific heat C_0 of the fluid according to eq. (1.7) [28, 41]:

$$\mu_{\mathrm{t}_0} = \frac{1}{\sqrt{\omega \frac{\rho_0 C_0}{2\,\kappa_0}}} \tag{1.7}$$

The deflection angle is directly proportional to the absorbed radiant power Φ_A as represented by the term $\Phi_0 \left(1 - e^{-\alpha d}\right)$, where Φ_0 is the initial radiant power incident in region 1 and α is the absorption coefficient of the absorbing film. $\frac{1}{n_0} \frac{dn}{dT}$ represents the relative change of the refractive index n_0 of the deflection medium due to the temperature change and shows the direct dependency of the deflection on the thermo-optical coefficient of the fluid. An indirect proportionality by $\frac{1}{r}$ is also observed for the pump beam radius r. This results from an increase of the probe beam-temperature gradient interaction length with r, but a decrease of the temperature gradient with r^{-2} [28]. The term $e^{-|z_0|\, \mu_{\mathrm{t}_0}^{-1}}$ demonstrates the exponential decrease of the deflection angle with increasing probe beam-sample offset z_0 and increasing chopping frequency ω (with $e^{-\sqrt{\omega}}$), as well as its dependence on the thermal parameters of the deflection fluid. The term $e^{i\omega t}$ describes the periodic oscillation of the deflection with the pump beam modulation.

The movement Δx of the probe beam spot on the position-sensitive detector resulting from

the deflection angle is dependent on the distance L from the sample to the detector as $\Delta x = \Theta L$. If a quadrant photodiode (see section 2.5.1.4) is used as detector, the periodic voltage difference signal induced by the deflected beam is inversely dependent on the beam diameter. Thus, the dependence of the measured signal on L disappears, as the beam diameter increases approximately linear with L [28].

1.2.2.2. Signal saturation

In cases of large values of αd (e.g. at $\alpha d > 1$) a saturation of the measurable deflection signal can occur which obscures the absorption profile of the film as smaller pump light wavelength-dependent changes of α have no significant impact on the radiant power absorbed within the film anymore. Whether a signal saturation can occur depends also on the thermal parameters of the system. For the consideration of different possible situations, the optical absorption length μ_α and the thermal diffusion length μ_t of the film in relation to its thickness d must be considered. The defintions of the two characteristic lengths are as follows [41]:

$$\mu_\alpha = \frac{1}{\alpha} \qquad\qquad \mu_\mathrm{t} = \frac{1}{\sqrt{\omega \frac{\rho C}{2\kappa}}} \tag{1.8}$$

Where ρ, C and κ are the density and thermal constants of the film material (see eq. (1.7)). Signal saturation can occur at certain combinations of the parameters in relation to the film thickness d. Key cases are discussed in the following.

For optically thin films ($\mu_\alpha > d$), a significant portion of the incident light is not absorbed in the layer and any change in the absorption coefficient results in a different amount of deposited heat. In this case, no signal saturation is expected for both thermally thin ($\mu_\mathrm{t} > d$) and thermally thick ($\mu_\mathrm{t} \ll d$) films. In the former case, all the heat generated throughout the thickness d will contribute to the deflection signal, thus reflecting any change in α. In the latter case, only heat generated within the length μ_t will contribute to the signal and no signal saturation is expected as the amount of heat deposited over this length of the film still depends on α due to $\mu_\alpha \gg \mu_\mathrm{t}$ [41].

For optically thick films ($\mu_\alpha \ll d$), almost all incident pump light is absorbed in the film with the largest portion already absorbed within a length much smaller than d. If the film is thermally thin ($\mu_\mathrm{t} > d$), saturation of the deflection signal is expected as heat generated throughout the full thickness of the film will contribute to the signal; however, the total absorbed light power does not change significantly upon change of α as long as μ_α is substantially smaller than the film thickness. For $\mu_\mathrm{t} \ll d$, signal saturation is expected for the case of $\mu_\mathrm{t} > \mu_\alpha$ as this resembles the case of a thermally thin film, while no signal saturation is expected in the case of $\mu_\mathrm{t} < \mu_\alpha$ as this will roughly resemble the case of an optically thin and thermally thick absorbing layer as discussed above [41].

The dependence of μ_t on ω must be considered, however, as a variation of the modulation frequency can alter the "thermal depth" to which the sample is probed and can influence a possible signal saturation. For comparison, the μ_t values of several common materials were estimated

Table 1.2. Density ρ, thermal conductivity κ and specific heat C as obtained from the stated references and the thermal diffusion lengths μ_{t} calculated from the thermal parameters for chopping frequencies of 1.7 Hz and 10 Hz via eq. (1.8) for some commonly used materials.

Material	ρ / kg m^3	κ / W m^{-1} K^{-1}	C / J kg^{-1} K^{-1}	μ_{t} / µm		**Refs.**
				ω = 1.7 Hz	ω = 10 Hz	
Fused quartz	2196	1.3	739	971	400	[42–44]
Silicon	2330	124	712	9380	3870	[42, 45]
P3HT	1100	0.185	1320	387	160	[46, 47]
$PC_{61}BM$	1520	0.07	820	257	106	[48]
$MAPbI_3$	4160	0.33	310	549	226	[49–51]

based on reference thermal properties and are displayed in Table 1.2. At typically used modulation frequencies of 1 – 10 Hz, the thermal diffusion lengths are on the order of a hundred to several hundreds of micrometers. Thus, in the case of thin film samples the absorbing layers are typically thermally thin.

1.2.2.3. Influence of Photoluminescence

The models which have been developed for the theoretical description of the temperature distribution induced by the photothermal heating are typically based on the assumption of the complete conversion of absorbed light into heat, thus assuming an efficiency of non-radiative recombination of $\eta_{\mathrm{NR}} \approx 1$ [28, 41, 52]. While this is a valid assumption for non-photoluminescent materials, a significant fraction of relaxation via radiative recombination of the photoexcited states in the absorbing material can lead to a deviation from the models and require modifications of the underlying equations.

The probe beam deflection is proportional to the photothermally deposited heat per unit time, Q, which corresponds to the absorbed radiant power Φ_A as can be determined from the incident pump light radiant power and the film absorptance according to $\Phi_A = \Phi_i A$ [52]. For a film which shows photoluminescence (PL) with a mean emission photon energy $\overline{E}_{\mathrm{PL}}$ and a PL quantum yield η_{PL}, the fraction of the absorbed light with a photon energy E which is not converted to heat due to PL can be accounted for according to eq. (1.9).

$$Q = \Phi_i A\, \eta_{\mathrm{NR}} + \Phi_i A\, \eta_{\mathrm{PL}} (1 - \frac{\overline{E}_{\mathrm{PL}}}{E}) \tag{1.9}$$

The first summand in the equation accounts for the heat generated by non-radiative recombination of the excited states, while the second summand accounts for the thermalization of carriers with excess energies to the band edge [53]. If radiative and non-radiative recombination are the only relaxation pathways for the photoexcited film, η_{NR} can be substituted by $\eta_{\mathrm{NR}} = 1 - \eta_{\mathrm{PL}}$ as the sum of quantum yields must amount to one [54]. Thus, eq. (1.9) can be transformed to:

$$Q = \Phi_i A\, (1 - \eta_{\mathrm{PL}} \frac{\overline{E}_{\mathrm{PL}}}{E}) \tag{1.10}$$

Since the deposited heat is typically directly related to the deflection signal S measured on the

position-sensitive detector, equation (1.10) can be further transformed to eq. (1.11), which directly relates the deflection signal measured at a pump light photon energy E to the absorptance of the film at E and is equivalent to the expressions given in refs. [32, 36, 53]. B is a constant which relates the photothermally deposited heat to S and contains all the parameters influencing the deflection signal as discussed in section 1.2.2.1 and in ref. [28].

$$\frac{S}{\Phi_i} = B\,A\,(1 - \eta_{\mathrm{PL}}\frac{\overline{E}_{\mathrm{PL}}}{E}) \tag{1.11}$$

As can be inferred from eq. (1.11), the occurence of radiative recombination in the sample leads to a deviation of the incident light power-corrected deflection signal from the absorptance profile as a function of PLQY and mean PL energy. The term $\frac{\overline{E}_{\mathrm{PL}}}{E}$ in the equation shows that the deviation increases upon decrease of the pump light photon energy and reaches a maximum when E equals the mean PL energy.

1.2.3. Applications of Transverse PDS

Transverse PDS has been applied in various different measurement tasks; several selected examples are discussed below.

1.2.3.1. Measurement of Band Tail and Defect State Absorption

One of the most common uses of PDS is for the investigation of the band-tail and defect state absorption of semiconductors. Semiconducting materials typically do not show an abrupt decline of their absorption spectrum at photon energies below their fundamental bandgap energy E_{g} but an exponentially decaying absorption tail (Urbach tail) towards lower energies which can be quantified according to its logarithmic slope, referred to as Urbach energy E_{U} [8, 17, 55]. This band tailing is induced by disorder in the material, which can be classified into thermal disorder (displacement of lattice atoms due to vibrations) and structural disorder (lattice distortions, e.g. due to amorphous or polycrystalline regions, defects, dopands or strain) [8]. The magnitude of the band tail absorption of a semiconducting material has a large impact on the performance of corresponding photovoltaic devices as a more pronounced tailing decreases the theoretical radiative efficiency limit of the devices [8, 56, 57] and a direct correlation between the Urbach energy and the solar cell open-circuit voltage losses was reported for several photovoltaic materials by De Wolf *et al.* [58]. PDS has been used to sensitively determine the band tails of films and bulk samples of semiconductors, including a-Si:H [17, 59], c-Si [60], GaAs [60, 61], a-C:H [62], $CuGaSe_2$ [55], $MAPbI_3$ [58], CdSe quantum dots [63] and PbS quantum dots [8, 57]. Furthermore, it has been used to characterize the effect of different material fabrication methods, processing parameters and doping levels on the band tailing [17, 57]. Moreover, the absorption by defect states extending towards lower energies beyond the Urbach tail, has been measured by PDS and evaluated for the estimation of the defect state density [16, 55, 60, 61, 64]. A typical absorption coefficient spectrum of a-Si:H, showing the profiles of band tail absorption and defect state absorption, is displayed in Fig. 1.4 (a) [65].

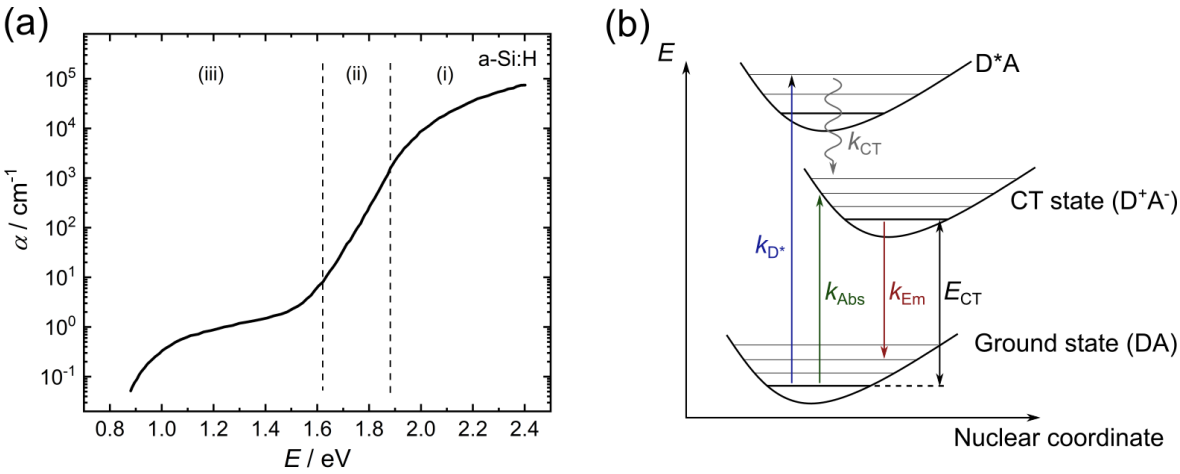

Figure 1.4. (a) Typical absorption coefficient spectrum of amorphous hydrogenated silicon (a-Si:H). The spectrum shows three different regions: (i) Region of band-to-band absorption at or above the bandgap energy, (ii) absorption from band tail states (Urbach tail) and (iii) defect-associated absorption [65]. Figure adapted from ref. [65]. **(b)** Schematic illustration of the potential energy surfaces of the donor-acceptor ground state DA, the CT state (D^+A^-) and the donor excited state D*A and the corresponding optical transitions between these states [66, 67]. E_{CT} represents the energy difference between the ground state and the CT state. The different rate constants k_i qualitatively represent different transition processes. Population of the CT state can occur via charge transfer k_{CT} from an exciton located on the donor D*, generated via photoexcitation $k_{\mathrm{D}*}$ from the donor molecules. Direct optical transitions between the ground state and the excited CT state can occur via CT absorption (k_{Abs}) or CT emission (k_{Em}) [66]. Figure adapted from ref. [66].

1.2.3.2. Optical Characterization of Organic Photovoltaic Materials

PDS has proved to be a very useful technique for the investigation of the absorption properties of organic photovoltaic (OPV) materials, particularly for the investigation of donor-acceptor interactions in bulk-heterojunction (BHJ) organic solar cells (OSCs).

The rapid photoinduced electron transfer from a conducting polymer (electron donor) to C_{60} fullerene (electron acceptor) driven by the difference of the energies of the lowest unoccupied molecular orbitals (LUMO) of the two components, as discovered by Sariciftci *et al.* [68], is a key process which helps to overcome the typically very large exciton binding energies (0.35 – 0.5 eV) in organic semiconductors that heavily impair charge separation and is the foundation for high-efficiency BHJ OSCs [69]. In these devices the active layer is composed of donor (D) and acceptor (A) molecules that are blended into a single layer which typically consists of mixed D and A domains of several tens of nanometers in size and molecularly intermixed phases [69–71]. The charge separation from the exciton formed upon photoexcitation, yielding e.g. an excited donor molecule D*, is believed to proceed via a so-called charge-transfer (CT) state, formed at the D-A interface upon electron transfer from D* to A, as an intermediate state which can dissociate into the charge separated (CS) state to yield free charge carriers [66]. The properties of this charge transfer state thus play a pivotal role for the performance of the corresponding OSC device as reviewed by Deibel *et al.* [72] and Coropceanu *et al.* [73].

At the D-A interface, the formation of a ground state complex due to electronic interaction of D and A molecules is suggested [74–76] which represents the ground state to which the excited CT state is coupled with the energy difference E_{CT} [77]. Optical transitions between ground state and

CT state can thus be observed at photon energies below the bandgap energies of D and A (CT absorption and CT emission); however, these transitions typically possess low oscillator strengths and require sensitive spectroscopic techniques such as PDS for their investigation [66]. The potential energy surfaces and transitions between the involved states are schematically shown in Fig. 1.4 (b). Since the CT interactions occur at the D-A interface, the strength of the CT absorption in a certain volume element of a blend depends on the corresponding interfacial area between D and A [76].

PDS has been used to directly measure the CT absorption in BHJ donor-acceptor blends to investigate the effects of different D-A weight ratios [19, 64, 78] and the effects of additives and annealing [76, 79] on the morphology and D-A interfacial area. The measurement of the CT absorption band allows the determination of E_{CT} from which the open-circuit voltage V_{OC} of an OSC can be estimated from the empirically found relation $E_{\mathrm{CT}} \approx qV_{\mathrm{OC}} + 0.6\,eV$, where q represents the elementary charge [75, 77, 80]. Furthermore, PDS has been used for the estimation of the trap state density from the sub-bandgap absorption to investigate the thermal stability [81], environmental stability [82] and light-induced degradation [40] of OPV materials.

The optical characterization of active layers for OSCs by PDS has also been used for the determination of the internal quantum efficiency (IQE) of the solar cells, which is defined as the ratio of collected charge carriers to the number of photons absorbed in the active layer of the device [83]. The value of the IQE thus is an important measure for the efficiency of charge generation and extraction in the device [83]. The IQE at a certain photon energy E is related to the fraction of the incident light on the solar cell which is absorbed in the active layer of the device, Λ_{AL}, and the external quantum efficiency (EQE) according to eq. (1.12) [80, 84].

$$\mathrm{EQE}(E) = \Lambda_{\mathrm{AL}}(E) \times \mathrm{IQE}(E) \tag{1.12}$$

The EQE (also referred to as incident photon to current efficiency, IPCE) is defined as the ratio of collected charge carriers to the number of incident photons on the solar cell [83] and can be measured relatively easy by photocurrent spectroscopy. PDS can be used to sensitively measure the absorptance of the active layer directly [66], which can be used for an approximation of Λ_{AL}. Alternatively, PDS can be used to determine the absorption coefficient spectrum of the active layer material which allows modelling of the absorption properties of the solar cell via a transfer matrix method under consideration of the absorptance and reflectance of its multiple layers and interfaces, if the optical parameters of the other layers of the device are known [80].

1.2.3.3. Other Applications

Transverse PDS has been used in various other applications, including measurements of the thermal diffusivity of soil samples [38] and lithium-ion battery electrodes [85], measurements of the photoluminescence quantum yields of fluorescent dye solutions [36], the optical investigation of semiconductor quantum wells [86, 87], trace analysis of pesticides in water [15], in-line concentration analysis of highly concentrated dye solutions [37] and in-situ monitoring of electrochemical reactions [88].

2. Experimental

2.1. Materials

Used solvents were obtained from commercial sources in reagent grade or higher purity and used as received. Copper(II) phthalocyanine (CuPc, 97 %) was obtained from Sigma and purified three times by vacuum sublimation (2.7×10^{-4} mbar and 390 °C) before use. Poly(methyl methacrylate) (PMMA, $M_W \approx 350{,}000\,g\,mol^{-1}$), polystyrene (PS, $M_W \approx 350{,}000\,g\,mol^{-1}$), lead(II) bromide (99.999 %), lead(II) iodide (99.9 %) and lead(II) chloride (99.9 %) were obtained from Sigma-Aldrich. Methylammonium bromide (99 %) was obtained from Greatcell Solar Materials. Hexanoic acid (98 %) was obtained from TCI. N_α-(*tert*-butyloxycarbonyl)-L-lysine (*t*boc-Lys, 97 %) was obtained from Alfa Aesar. PBDB-T-2F (PM6), PTB7-Th (PCE-10), IT-4F (ITIC-F) and $PC_{71}BM$ (see List of Abbreviations for full chemical names) were obtained from 1-Material. PEDOT:PSS (Clevios PH1000 aqueous dispersion) was obtained from Heraeus. Zonyl FS-300 fluorinated surfactant (40 % solution in water) was obtained from abcr. Indium tin oxide-coated glass substrates were obtained from Xinyan Technology. Soda lime glass microscope slides were obtained from Marienfeld. *N,N*'-Bis(2,6-diisopropylphenyl)-3,4,9,10-perylene diimide (PDI) was provided by the Institute for Chemistry and Technology of Materials of the University of Technology Graz, Austria. Methylammonium iodide was synthesized according to a published procedure [89].

2.2. Sample Preparation and Film Thickness Measurements

Thin films of sample materials were deposited on fused quartz or soda lime glass (Marienfeld microscope slides) substrates. Substrates were cleaned by consecutive treatment in an ultrasonic bath with a 2 % (v/v) aqueous solution of Hellmanex II, deionized water, acetone, isopropanol and a solution of 5 mL 25 % (w/w) ammonia and 5 mL 30 % (w/w) hydrogen peroxide in 200 mL deionized water for 10 minutes at 40°C, respectively. After ultrasonic treatment, the substrates were rinsed with deionized water and blow-dried with nitrogen. Prior to film depositions, the cleaned glass substrates were treated with an oxygen plasma at 100 W for 5 min in a Plasma Etch PE-25 plasma cleaner.

The thicknesses of deposited films were measured on a Bruker DektakXT Profilometer. For all measurements a stylus force of 2 mg was used.

2.2.1. Organic Semiconductor Films

For the fabrication of PEDOT:PSS films a solution was prepared by mixing 20 mL of Clevios PH1000 PEDOT:PSS dispersion with 1 mL of DMSO and 3 drops of Zonyl FS-300 surfactant. Films were deposited on soda lime glass substrates by spin coating at 1500 rpm for 45 s on a Süss MicroTec LabSpin spin coater, after filtration of the solution through a 0.45 µm regenerated cellulose (RC) syringe filter. The deposited films were dried for 15 min at 120 °C, followed by spin washing with isopropanol on the spin coater at 4000 rpm for 10 s and annealing at 120 °C for

Table 2.1. Overview of deposition method, temperature at the deposition and film thickness of the investigated OPV films. All films were prepared from 1.5 % (w/v) solutions in chlorobenzene; the blend films were prepared from solutions with a mass ratio of 1:1 of the donor and acceptor components. The abbreviation rt refers to room temperature.

Material	**Deposition method**	**Deposition temperature**	***d*** **/ nm**
PBDB-T-2F	Spin coating	rt	35
	Blade coating	rt	290
PTB7-Th	Blade coating	rt	1300
IT-4F	Spin coating	rt	25
	Drop casting	90 °C	≈ 4000
$PC_{71}BM$	Spin coating	rt	25
	Drop casting	90 °C	≈ 4900
PBDB-T-2F:IT-4F	Spin coating	rt	35
	Drop casting	rt	≈ 6000
PBDB-T-2F:$PC_{71}BM$	Blade coating	rt	270
PTB7-Th:IT-4F	Spin coating	rt	90
	Blade coating	rt	≈ 3000

15 min to yield PEDOT:PSS films with thicknesses of ca. 80 nm.

Films of copper(II) phthalocyanine (CuPc) were deposited on fused quartz by thermal evaporation in a Vaksis PVD system. Film deposition was carried out under high vacuum conditions with a base pressure in the vacuum chamber of 2.3×10^{-6} mbar and at a deposition rate of $1-2.5\,\text{Å}\,s^{-1}$. The substrates were kept at room temperature.

For the preparation of a film of *N,N'*-Bis(2,6-diisopropylphenyl)-3,4,9,10-perylene diimide (PDI) dispersed in a matrix of PS at a mass ratio of PDI:PS of 1:10, a mixed solution was prepared by adding 30 µL of a 5 mg mL^{-1} solution of PDI in chloroform to 50 µL of a 30 mg mL^{-1} solution of PS in chloroform and stirring the mixture for one day. Film deposition was carried out by blade coating at room temperature on 25×5 mm^2 soda lime glass substrates.

Films of the OPV materials PBDB-T-2F, PTB7-Th, IT-4F, $PC_{71}BM$ and blends thereof were deposited on fused quartz by spin coating, blade coating or drop casting from 1.5 % (w/v) solutions of the materials in chlorobenzene (CB). Films of PBDB-T-2F:IT-4F, PBDB-T-2F:$PC_{71}BM$ and PTB7-Th:IT-4F blends were prepared from solutions with a 1:1 mass ratio of the dissolved components. Spin coating was carried out on 9.7×9.7 mm^2 fused quartz substrates using a KLM spin coater. Blade coating was performed manually with a custom-built blade coating device. Depositions by drop casting and blade coating were carried out on 25×5 mm^2 fused quartz substrates. The preparation of solutions and the film depositions were carried out in a glovebox under N_2-atmosphere. An overview of the prepared OPV films including deposition method, deposition temperature and film thickness is given in Table 2.1.

2.2.2. Perovskite Films

2.2.2.1. Perovskite Nanoparticle Films

The synthesis of perovskite nanoparticles was carried out by Anna Jancik Prochazkova (Brno University of Technology, Czech Republic), Yolanda Salinas and Elisabeth Leeb (Johannes Kepler

University Linz, Austria). Methylammonium lead bromide ($MAPbBr_3$) nanoparticles with sizes of ca. 6 nm were prepared according to a published procedure [90]. The perovskite nanoparticles (PNPs) were prepared from a precursor DMF solution by ligand-assisted precipitation in toluene, using hexanoic acid and *t*boc-Lys as ligands. The PNP size and crystal growth was controlled by the addition of 16 mol equivalents of water to the precursor solution. After washing and redispersion steps, thin films of the $MAPbBr_3$ nanoparticles were deposited on $9.7 \times 9.7\,mm^2$ soda lime glass substrates by centrifugal casting [90].

2.2.2.2. Bulk Perovskite Films

The deposition of mixed-halide methylammonium lead perovskite $MAPbI_{3-x}Cl_x$ films was carried out by Bekele Hailegnaw Teklemariam (Johannes Kepler University Linz, Austria) according to a published procedure [89]. A precursor solution was prepared by dissolving PbI_2, $PbCl_2$ and methylammonium iodide in a molar ratio of 1:1:4 under stirring at 45 °C overnight in DMF to obtain a solution with a total concentration of 0.88 M. Additionally, 10 % (v/v) acetylacetone were added to the precursor solution [89]. A film of $MAPbI_{3-x}Cl_x$ with a thickness of 600 nm was deposited on a fused quartz substrate via spin coating and annealed at 115 °C for 30 min.

2.3. Transmittance and Reflectance Measurements

Transmittance (T) and reflectance (R) spectra of sample films were measured on a PerkinElmer Lambda 1050 UV/Vis/NIR spectrophotometer. For transmittance measurements the spectrometer was equipped with a three detector module (Photomultiplier tube (PMT), InGaAs detector and PbS detector). For reflectance measurements a 150 mm integrating sphere module equipped with a PMT and an InGaAs detector was used. From measured transmittance and reflectance, the absorptance A of sample films was determined according to the relation $A = 1 - T - R$.

2.4. Photoluminescence Spectroscopy

2.4.1. Photoluminescence and Photoluminescence Excitation

Photoluminescence (PL) and photoluminescence excitation (PLE) spectra of sample films were measured on a PTI QuantaMaster 40 spectrofluorometer using a double monochromator setup on the excitation and the emission channel and a PMT detector. Measurements were carried out using a 320 nm longpass filter in the excitation channel to block light of lower orders of diffraction. All recorded PL and PLE spectra are corrected for the detector response and the spectral output of the excitation light source. All spectra were recorded at room temperature.

2.4.2. Photoluminescence Quantum Yield

The external photoluminescence quantum yields (PLQY) of sample films were determined using a Hamamatsu Photonics external quantum yield measurement system, equipped with a A9924-06 integrating sphere, a L9799-01 continuous mode Xe lamp, a C8849 lamp power supply, a A10080-01 monochromator and a PMA-12 photonic multi-channel analyzer. For all samples, the PLQY was measured at room temperature. The measurements were carried out by Markus Scharber (Johannes Kepler University Linz, Austria).

2.5. Photothermal Deflection Spectroscopy

2.5.1. Setup and Components

In this work a transverse photothermal deflection spectroscopy setup was used for the optical characterization of sample films. A schematic representation of the used setup is displayed in Fig. 2.1. The PDS setup consists of four main subsystems:

- Pump beam system
- Probe beam system
- Sample and deflection medium
- Detection and data acquisition components

Each of the subsystems was subject to separate design choices and optimization in order to reach high sensitivity and a maximal signal-to-noise ratio (SNR), while meeting the specific requirements for the setup to perform the desired measurements. Pathways for achieving a high SNR are the increase of the attainable deflection signal and the decrease of the noise level. As a first approximation it can be assumed that the magnitude of the deflection signal is determined primarily by the pump beam and sample and deflection medium subsystems, while the noise level is mainly determined by the probe beam and detection subsystems [8]. Several theses and publications proved helpful resources for the design and optimization of the setup [8, 11, 28, 91, 92]. The detailed setup, used components, design principles and optimization measures for each subsystem are discussed below.

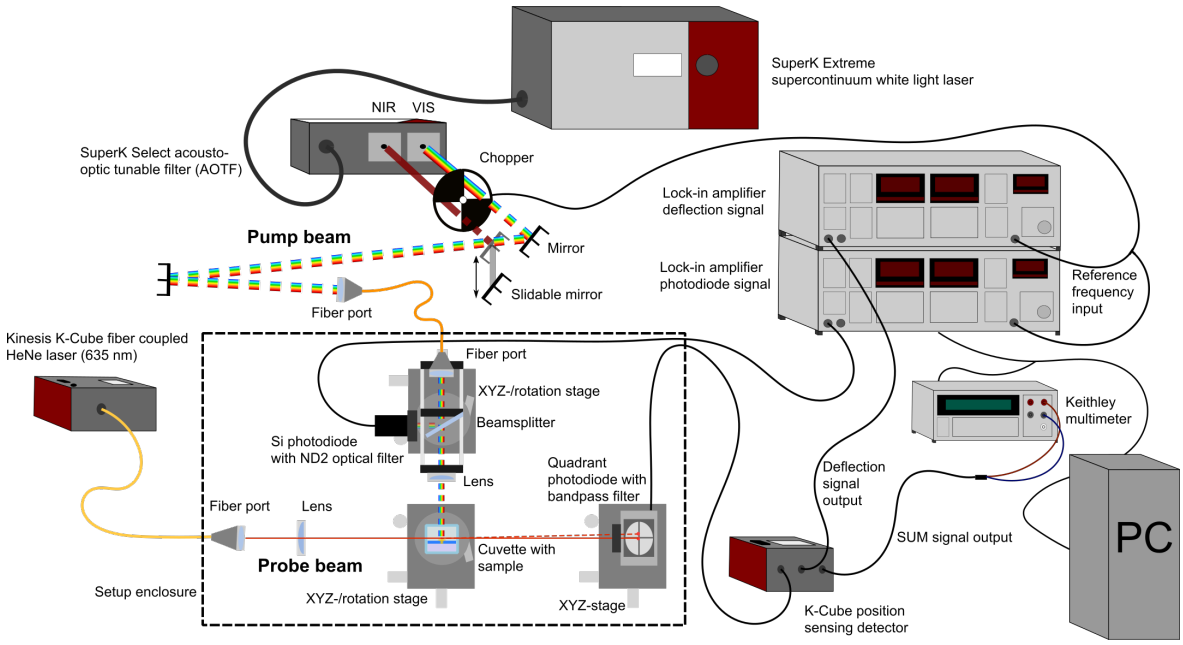

Figure 2.1. Schematic representation of the used transverse PDS setup. The pump light is provided by a supercontinuum white light laser fiber coupled to an acousto-optic tunable filter as monochromator and modulated by a mechanical chopper. The pump power spectrum is monitored by a Si photodiode. The probe beam is provided by a fiber coupled HeNe laser and its deflection is measured on a quadrant photodiode. Lock-in amplifiers and a digital multimeter are used to measure the output signals.

2.5.1.1. Pump Beam System

The pump beam system consists of the pump light source, a monochromator, a mechanical chopper as well as light guiding and focussing optics.

The most commonly utilised pump light sources for PDS are broadband sources like Xe arc lamps [8, 11, 36, 93, 94] or quartz-tungsten-halogen (QTH) lamps [11, 18, 91]. More rarely supercontinuum laser sources [95] or standard solid-state, diode or gas lasers are used [14, 34, 96]. In this work, a NKT Photonics SuperK EXTREME EXB-6 supercontinuum white light laser was used as the pump light source which offers the advantage of a high spectral brightness over a broad wavelength range and a power tunability of 15 – 100% of its maximum output power [97].

A NKT Photonics SuperK Select acousto-optic tunable filter (AOTF) was used as monochromator and connected to the output fiber of the SuperK EXTREME supercontinuum laser. The used instrument was equipped with two AOTF crystals, covering tunable wavelength ranges of 400 – 650 nm (VIS) and 690 – 1100 nm (NIR) with two separate output apertures.

The light beam output of the AOTF was modulated by a mechanical chopper (Stanford Research Systems SR540) equipped with a two-slot blade to enable lock-in detection of the deflection signal. To maximize the achievable deflection signal (see section 1.2.2.1), a low modulation frequency of 1.7 Hz was chosen which still provided smooth operation of the chopper and showed no significant negative impact on the noise level of the setup (see section 3.1.1).

Via an assembly of mirrors and a fiberport equipped with an achromatic lens (Thorlabs PAF2 A4B) the modulated pump light is coupled into a multimode optical fiber (Thorlabs M122L). The output port (Thorlabs PAF2 A4B) is mounted on a 30 mm cage system on a 3-axis translation and rotation stage. After passing a beamsplitter, which samples a fraction of the pump beam onto the pump power monitor photodiode (see section 2.5.1.4), the pump light is focussed onto the sample via a plano-convex lens (Thorlabs LA1951, focal length $f = 25.4$ mm). The pump beam spot diameter at the sample is ca. 350 µm as determined by microscopic examination of photodegraded films.

As shown in Fig. 2.2 (a), the output spectra of the AOTF at different wavelengths show full widths at half maximum (FWHM) of ca. 3.0 nm to 6.4 nm depending on the selected output wavelengths, as measured on an Andor iDus 420 CCD equipped with an Andor Shamrock 303i spectrograph. A pinhole aperture was used for the measurement to decrease the beam diameter to the size of the beam which is coupled into the optical fiber of the PDS setup. It must be noted that the light output of the AOTF additionally shows low-intensity bands of different wavelengths than the selected center wavelength that are spacially shifted from the central output. These pump light artefacts are effectively spacially filtered by the pump light guiding optics in the VIS regime, however, start to progressively appear in the pump light bands towards higher wavelengths, as observable in Fig. 2.2 (a), and slightly broaden the spectral bandwidths. A comparison of the pump light radiant power spectrum measured at the output of the AOTF and at the position of the sample is given in Fig. 2.2 (b). While the use of the optical fiber leads to the loss of spectral power in the low-wavelength part of the spectrum, it allows effortless, precise and repeatable adjustments of the pump beam position and enables an easy exchange of the pump light wavelength source.

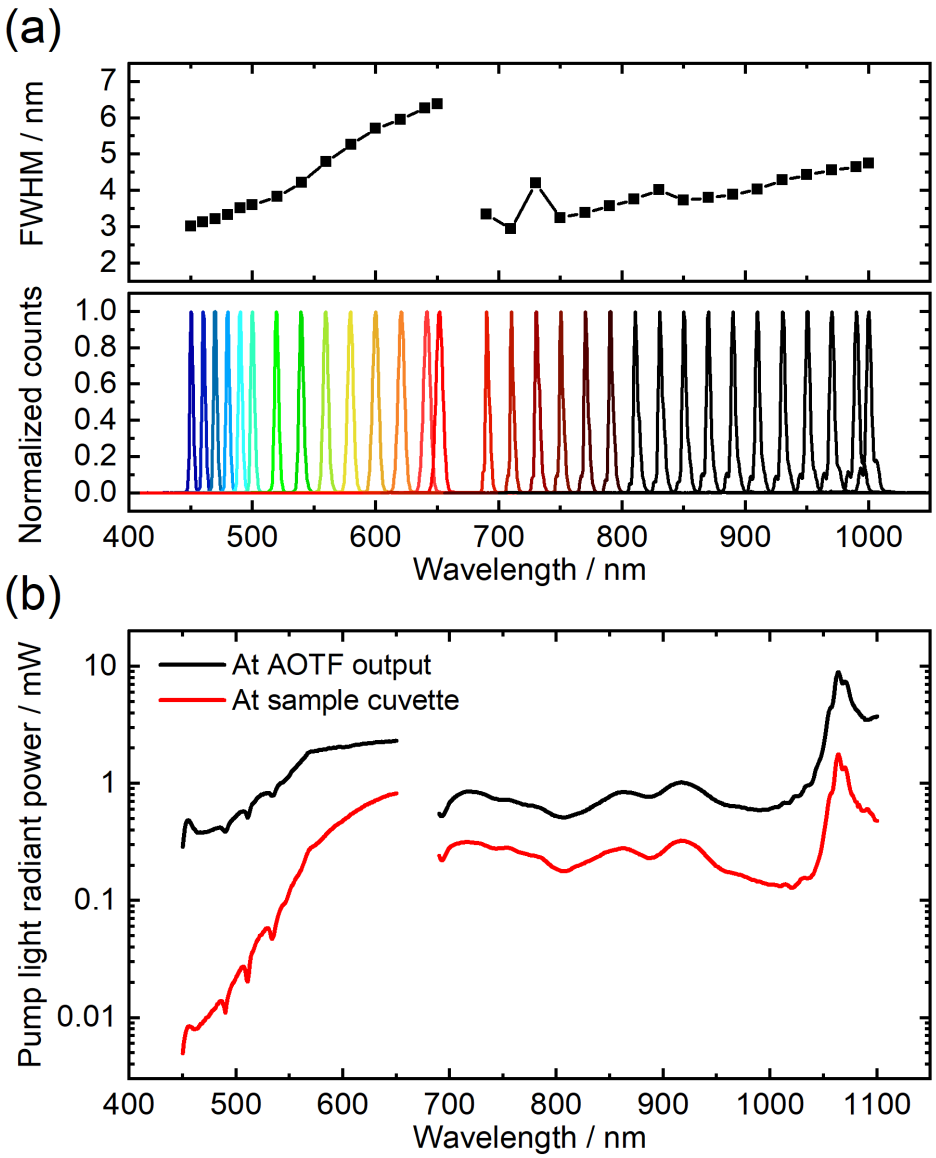

Figure 2.2. **(a)** Output spectra of the AOTF at different wavelengths in the range of 450 – 650 nm and 690 – 1000 nm with the corresponding FWHM of the pump light bands. Measured on an Andor iDus 420 Si CCD equipped with an Andor Shamrock 303i spectrograph. A pinhole aperture was used to decrease the beam diameter to the size of the beam which is coupled into the optical fiber of the PDS setup. **(b)** Comparison of the radiant power spectrum of the pump beam measured at the acuosto-optic tunable filter (AOTF) output and at the sample position at 100 % relative output power of the supercontinuum laser.

2.5.1.2. Probe Beam System

The probe beam subsystem consists of the probe beam source and light guiding and focussing optics.

A Thorlabs Kinesis K-Cube fiber coupled HeNe laser source (λ_{center} = 635 nm) with a variable output power of up to 8 mW was utilised as probe beam source. The output fiber was connected to a fiber collimator (Thorlabs CFC11X-A, f = 11.0 mm) and the output probe beam was focussed at the sample cuvette with a plano-convex lens (Thorlabs LA1509, f = 100 mm). The laser was typically operated at an output power of 2.55 mW to obtain a sum voltage signal of ca. 4 V at

the quadrant photodiode as recommended by the supplier. To reduce noise of the probe beam resulting from vibrations of the optical fiber, the fiber was decoupled from the enclosure of the setup (see Section 2.5.1.5) and supported with an optical post equipped with foam for vibration damping.

2.5.1.3. Sample and Deflection Medium

The main components of the sample system are sample stage, sample holder, cuvette, deflection medium and the experimental sample. A 3-axis translation and rotation stage fitted with a cuvette holder was used as sample stage. A square-base optical glass cuvette (Hellma OS) with 10 mm path length was used to contain the sample holder and deflection fluid. The cuvette was sealed with a polyethylene cuvette cap to avoid evaporation of the deflection fluid and ingress of dust particles. A screw was used to tightly fix the cuvette in the cuvette holder to prevent displacement during measurements and increase the reproducibility of sample positioning.

Sample Holder and Sample Dimensions

Two different custom-made sample holders, shown in Fig. 2.3, were used for the conducted PDS measurements depending on the sample type and its dimensions. Both sample holders are made from stainless steel and have a $9.8 \times 9.8\,\mathrm{mm}^2$ base to ensure a secure fit in the cuvette. In sample holder A two auxiliary flexible metal plates are implented to hold the sample holder in place and avoid tilting in the cuvette.

Sample holder A uses a hex screw to mount the sample and is limited to maximum total sample thicknesses (substrate plus film) of 2 mm. The circular notch in the holder allows transmission of incident pump light which is not absorbed or reflected by the sample to avoid back reflection of light by the metallic sample holder. Thus, the sample must have a minimal height to reach above the lower edge of the notch, while the maximal height is limited by the cuvette cap. Sample

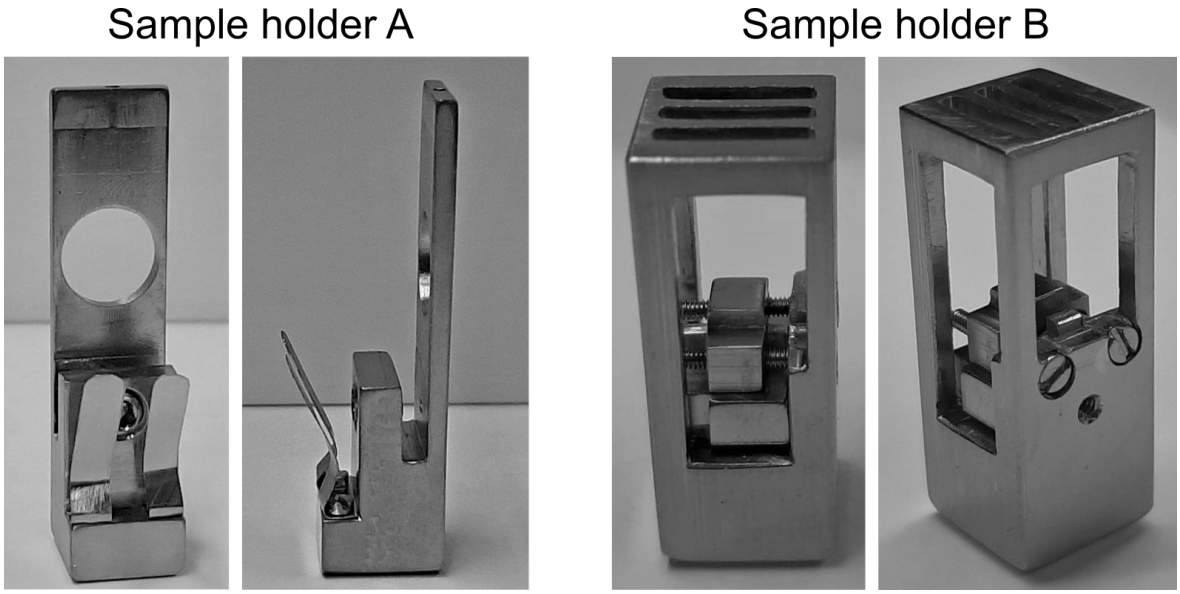

Figure 2.3. Photographs of the custom-made sample holders used in the PDS setup. Front and side view of sample holder A are shown on the left side; side and rear view of sample holder B are shown on the right side.

holder B features a stainless steel slide whose position can be adjusted by two slotted screws on the backside of the holder and can mount samples with thicknesses up to a maximum of ca. 4 mm. The maximum height of mountable samples is limited by the frame of the holder. The notches in the top surface allow additional fixation of samples by a screw mounted on the upper frame. Sample holder B therefore offers a high tolerance towards different sample geometries and allows measurement of unconventional samples including free-standing films and crystals, provided they possess a sufficiently flat surface in at least one direction which is large enough to allow placement of the pump light spot and passing of the probe laser. The possible thicknesses t, heights h and widths w of samples mountable in each sample holder are as follows:

- Sample holder A:
  - $t < 2$ mm
  - 12 mm $< h <$ 28 mm
  - $w < 10$ mm
- Sample holder B:
  - $t < 4$ mm
  - 3 mm $< h <$ 10 mm
  - $w < 10$ mm

The maximum sample width is limited by the inner cuvette side length of 10 mm, while the minimal width is in principle only restricted by the pump beam diameter at the sample. A smaller width can benefit the PDS measurement as it allows placing the probe beam closer to the sample before the converging beam is clipped at the sample edges and thus allows to reach higher deflection signals. Depending on the sample preparation method, however, typically widths of $w \geq 5$ mm were used in this work to allow a more straightforward film deposition on the corresponding substrates and enable the investigation of samples by other measurement methods which require larger sample widths.

Substrate and Sample Film Properties

In this work, thin films of sample materials on transparent substrates were investigated. To allow unproblematic measurements of thin film samples, several conditions concerning substrate and film properties need to be considered.

The substrate on which the sample films are deposited needs to be chosen carefully depending on the investigated sample. Optimal substrates for typical PDS measurements should be transparent and should possess a low thermal conductivity κ to reduce dissipation of heat over the substrate volume and consequently increase heat transfer to the deflection fluid at the pump beam spot [8]. A range of materials including inorganic glasses (e.g. soda-lime glass: $\kappa \approx 1$ W m^{-1} K^{-1} [98] or fused quartz: $\kappa \approx 1.3$ W m^{-1} K^{-1} [43]) and transparent polymers (typically $\kappa = 0.1 - 0.5$ W m^{-1} K^{-1} [99]) meet this criteria. For measurements of sample films with very low absorptance in the wavelength range of interest, the absorptance of the substrate should be as low as possible to avoid masking of the absorption profile of the film by the deflection signal resulting from light absorption of the substrate. Thus, fused quartz was used as substrate for sensitive sub-bandgap PDS measurements of semiconductor materials due to its extremely low absorption coefficient in the visible and NIR spectral regime [100]. For materials where only a highly absorbing region of the absorption spectrum is of interest, soda-lime glass (Marienfeld microscope slides) substrates with a thickness of 1 mm were used. To measure the deflection

signal contribution of different substrate materials and thus evaluate their suitability for use in PDS, measurements on bulk samples of fused quartz, soda lime glass and films of polystyrene, poly(methyl methacrylate), indium tin oxide (ITO) and PEDOT:PSS on glass were carried out as shown in section 3.1.2.

The optimal film properties of thin film samples for PDS depend on the desired measurement. For investigation of absorption features with a low absorption coefficient a high film thickness is beneficial to avoid a limitation of the minimally measurable absorption coefficient by the noise limit of the setup. If the absorption bands in a highly absorbing region are of interest, however, the film thickness should not be too high to avoid masking of the absorption profile by signal saturation (see section 1.2.2.2). Generally, high homogeneity and uniform thickness of the film are advantageous to increase consistency of the deflection spectra measured at different positions on the sample and to decrease the uncertainty of the absorption coefficient determined from PDS measurements.

Deflection Medium

The choice of deflection medium is an important parameter for the PDS setup due to its high impact on the achievable deflection signal. For an optimal implementation, a deflection medium needs to meet the following requirements [8]:

- Optical transparency in the wavelength range of interest
- Inertness towards sample and sample holder materials
- High temperature dependence of refractive index (thermo-optical coefficient)
- Low thermal conductivity

A range of different fluids have been sucessfully used in PDS setups including carbon tetrachloride [11, 91, 93], hexane [39, 63], paraffin oil [108] and acetonitrile [109], as well as liquid nitrogen for measurements at 77 K [53, 110] . While these fluids largely possess suitable thermal and thermo-optic parameters for the application as deflection fluid, they often lack inertness towards a broader range of sample materials, especially concerning organic materials, and are often not suitable for measurements over a large wavelength range due to light absorption in the NIR (e.g. in the case of hexane) [8].

An advantageous class of fluids for application in PDS are fully-fluorinated hydrocarbons (e.g. fluids of the *Fluorinert* trademark from 3M or the *Flutec* trademark from F2 Chemicals) as they are chemically highly inert, non-toxic, largely show superior thermal/thermo-optic properties and optical transparency over an extended wavelength range [8]. Among these fluids, perfluorohexane (Fluorinert FC-72) is one of the most widely used deflection fluids due to its outstanding thermo-optic properties [8]; however, it suffers from a high vapor pressure and low boiling point [101] which leads to high evaporation losses. Thus, different perfluorinated hydrocarbons with significantly lower volatility were investigated as deflection fluids in PDS measurements of a copper(II) phthalocyanine reference sample and their performance was compared to that of Fluorinert FC-72 to identify a well-performing non-volatile replacement (see section 3.1.5). The investigated fluids and

Table 2.2. Overview of the investigated deflection fluids and respective values of vapor pressure p_v at 25 °C and boiling point T_B as specified in the corresponding data sheets [101–107].

Fluid	Chemical name	Abbreviation	p_v / mbar	T_B / °C
Fluorinert FC-72	Perfluorohexane	FC-72	309	56
Flutec PP6	Perfluorodecalin	PP6	8.8	142
Perfluoro(1,3-diethylcyclohexane)		PFDiEtCy	-	142
Flutec PP9	Perfluoro(methyldecalin)	PP9	2.9	155
Flutec PP10	Perfluoroperhydrofluorene	PP10	< 1	194
Flutec PP11	Perfluoroperhydrophenathrene	PP11	< 1	215
Flutec PP24	Perfluoroperhydrofluoranthene	PP24	< 1	244

corresponding vapor pressures and boiling points are listed in Table 2.2. All further measurements were carried out using perfluoro(methyldecalin) (Flutec PP9) as deflection fluid.

2.5.1.4. Detection and Data Acquisition

The components of the detection and data aquisition subsystem are the position sensitive detector, the pump light power monitor, lock-in amplifiers and a digital multimeter.

The position sensitive detector unit consists of a quadrant photodiode (Thorlabs PDQ80A), mounted on a 3-axis translation stage and connected to a Thorlabs Kinesis K-Cube position sensing detector (PSD). The photodiode layout and the determination of the PSD voltage output signals X_{Diff}, Y_{Diff} and SUM from the photocurrents I_i generated by the incident probe beam are shown in Fig. 2.4 and eqs. (2.1) – (2.3), respectively, with the transimpedance gain $Z_f = 10\,\mathrm{kV\,A^{-1}}$ [111]. The AC modulated x-axis difference signal X_{Diff} corresponds to the photothermal probe beam deflection voltage signal and is fed into a Stanford Research Systems SR865A lock-in amplifier (LIA). As can be inferred from eqs. (2.1) and (2.2), the X_{Diff} signal is dependent on the total incident light power of the probe beam on the quadrant diode. Thus, the total light power on the quandrant photodiode was additionally monitored by measuring the SUM output signal of the PSD on a Keithley 2700 digital multimeter to facilitate the compensation of deflection signal changes

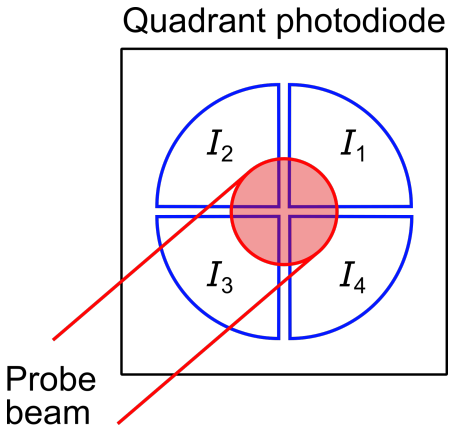

$$X_{\mathrm{Diff}} = Z_f[(I_2 + I_3) - (I_1 + I_4)] \quad (2.1)$$

$$Y_{\mathrm{Diff}} = Z_f[(I_1 + I_2) - (I_3 + I_4)] \quad (2.2)$$

$$\mathrm{SUM} = Z_f[I_1 + I_2 + I_3 + I_4] \quad (2.3)$$

Figure 2.4. Schematic representation of the quadrant photodiode layout. The incident probe beam generates a photocurrent I_i proportional to the fraction of the beam falling on each quadrant i. The output voltage signals X_{Diff}, Y_{Diff} and SUM are determined from the photocurrents and the transimpedance gain Z_f according to equations (2.1) – (2.3) [111].

caused by probe beam power fluctuations.

In order to prevent stray light (e.g. reflected pump beam light) from reaching the quadrant photodiode, a bandpass filter with a central wavelength of 635 nm (Thorlabs FL05635-10, FWHM = 10 ± 2 nm) is mounted in front of the diode. Additionally, two iris diaphragms are placed in the probe beam path to block some of the probe beam light reflected from cuvette or the quadrant photodiode to reduce probe beam stray light.

Monitoring the pump light power spectrum in situ during measurements is realized with a Si photodiode (Thorlabs SM1PD1A) onto which a fraction of the modulated pump light is sampled by a beamsplitter (see section 2.5.1.1). The AC modulated current output of the photodiode is measured via lock-in detection on a Stanford Research Systems SR830 lock-in amplifier. A reflective neutral density filter (Thorlabs NDUV20A, OD = 2) is mounted in front of the Si photodiode to prevent an input signal overload at the LIA.

A custom-made software developed in the LabVIEW development environment (National Instruments) is used for instrument control and data readout.

Beamsplitter Correction Factor

To correctly determine the spectral profile of the pump light reaching the sample from the pump light reflected onto the Si photodiode by the beam splitter, a correction factor relating the measured photocurrent at the pump power monitor to the power of the transmitted pump light at the sample cuvette must be determined. The schematic measurement setup used for the determination of the correction factor is shown in Fig. 2.5 (a). The sample cuvette was replaced with a calibrated photodiode (Hamamatsu Si photodiode) with known responsivity γ_{PD} (in A W^{-1}), connected to a variable gain transimpedance amplifier (Femto DLPCA-200) with a transimpedance gain set to $Z_{\mathrm{f}} = 10^3$ V A^{-1}. This allowed conversion of the photocurrent I_{T}, induced by the transmitted pump light, to a voltage signal V_{T} according to the relation $V_{\mathrm{T}} = I_{\mathrm{T}} \cdot Z_{\mathrm{f}}$ to avoid a signal overload at the LIA upon immediate input of the current signal. A pump light scan over the wavelength ranges of 400 – 650 nm and 690 – 1100 nm was carried out and V_{T} as well as the photocurrent I_{R} at the pump power monitor were detected at the LIAs. The correction factor C_{BS} (typically determined in units of mW μA^{-1}) for each wavelength λ was calculated according to equation (2.4) and is shown in Fig. 2.5(b).

$$C_{\mathrm{BS}}(\lambda) = \frac{V_{\mathrm{T}}}{Z_{\mathrm{f}} \gamma_{\mathrm{PD}} I_{\mathrm{R}}} \tag{2.4}$$

Since the correction factor depends on the ratio of reflected to transmitted light at the beamsplitter, the polarization of the incident pump light is a critical parameter as it determines the reflection behavior at interfaces between different media [112]. Thus, changes in the alignment of the multimode optical fiber used for guiding the pump light should be avoided throughout the use of the setup as variation of the fiber geometry can induce a change of the polarization state of the output light [113, 114]. Consequently, any major change of the fiber alignment requires remeasurement of the beamsplitter correction factor.

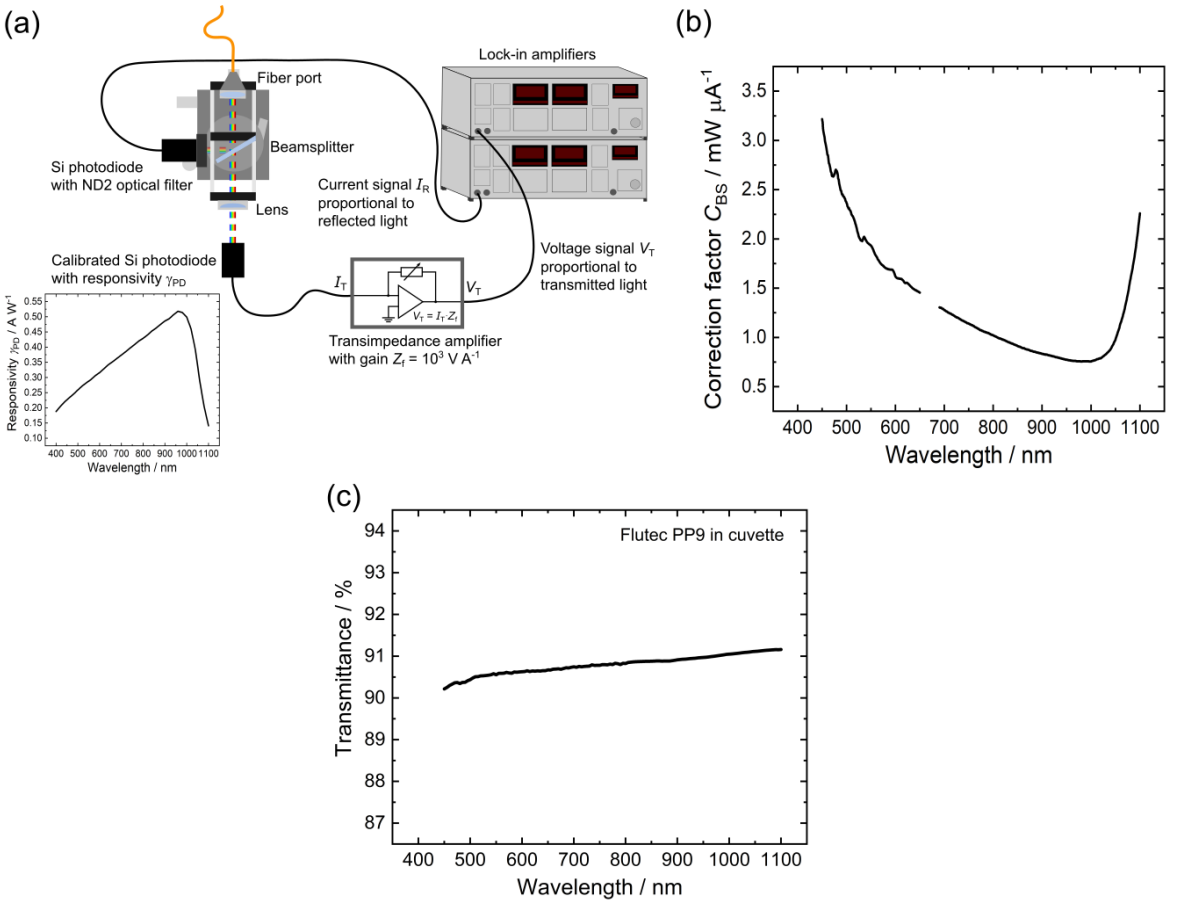

Figure 2.5. (a) Schematic representation of the setup used for determination of the beamsplitter correction factor C_{BS}. Components unchanged in comparison to the standard measurement setup (see Figure 2.1) are omitted for clarity. The graph shows the responsivity curve of the calibrated photodiode. **(b)** Correction factor C_{BS} determined for the used setup. **(c)** Transmittance spectrum of the sample cuvette filled with the deflection fluid Flutec PP9 (measured versus air).

The front surface reflectance of the sample cuvette filled with the deflection fluid PP9 is approximately constant over the spectral range of 450 – 1100 nm as deduced from the almost constant transmittance of the cuvette and deflection fluid shown in Fig. 2.5 (c). Thus, no additional correction factor was used for the cuvette reflectance since the purpose of the correction is to account for the spectral profile of the pump light and does not require knowledge of the exact radiant power of the pump light at the sample. Addtionally, the relative reflection losses can be assumed constant for all PDS measurements with the same sample cuvette and deflection medium, hence allowing quantitative comparison of the measured deflection signals with respect to the incident pump power.

2.5.1.5. Isolation of the Setup from the Environment

Highly sensitive PDS measurements require the detection of very small beam deflection signals. Thus, isolation and decoupling of the setup from its environment is necessary to avoid distortion by external disturbance factors and achieve a maximum sensitivity. The following major external noise sources can be identified [8, 91]:

- Ambient mechanical vibrations
- Air flow around the probe beam path
- External light falling on position sensitive detector

The reduction of noise due to mechanical vibrations is achieved by assembling the PDS setup on a passive vibration-isolated optical table (Melles Griot) which facilitates decoupling of the setup from ambient vibrations. Additionally, the supercontinuum laser light source and the lock-in amplifiers are placed on a separate table to avoid a contribution of vibrational noise from their cooling fans during operation.

To shield the setup from air flow and external light, the inner components of the setup are enclosed in a custom-built black plastic box with two openable lids as shown in Fig. 2.6. The significant reduction of noise due to the enclosure of the setup is shown in section 3.1.1. Additional shielding of the detector from external light is provided by the bandpass filter at the quadrant photodiode as described in section 2.5.1.4.

2.5.2. Measurement Procedure

Before regular PDS measurements were be performed after assembly of the setup, a rough alignment of the sample stage and pump beam focussing optics was carried out to ensure positioning of the sample cuvette center and the focussed pump beam spot at the focal point of

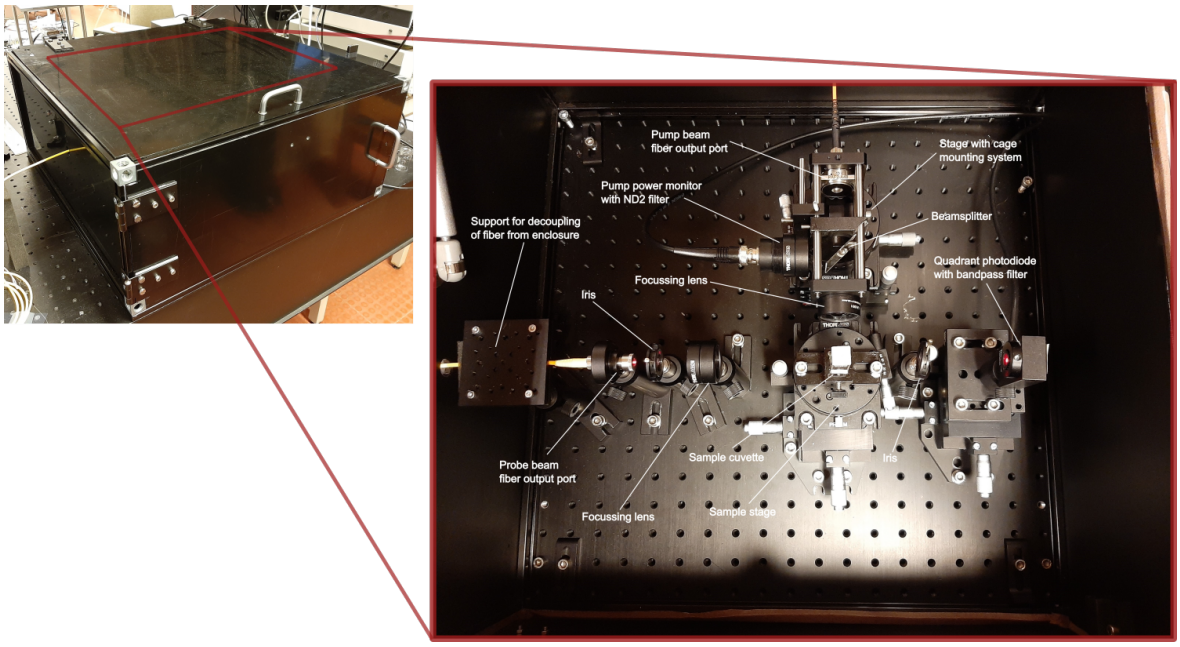

Figure 2.6. Photograph of the custom-built black plastic box used to shield the setup from air flow and external light and top-down view of the components enclosed in the box.

the probe beam.

The procedure for the PDS measurement of a sample of suitable dimensions (as described in section 2.5.1.3) can be divided into the following general steps:

- Mounting of the sample in the sample holder and insertion in cuvette
- Sample alignment
- Selection of suitable measurement parameters
- Measurement in the specified wavelength range

First the sample is loaded and tighly fixed into one of the sample holders (see section 2.5.1.3) suited for its dimensions. The loaded sample holder is carefully cleaned with compressed nitrogen to remove particles from its surface and placed into the clean and dry cuvette. The cuvette is filled with deflection fluid which is filtered through a 0.45 µm PTFE syringe filter and is sealed with a PE cuvette cap. For oxygen-insensitive samples these steps are carried out under normal laboratory atmosphere in a laminar flow cabinet. For oxygen-sensitive samples (e.g. organic semiconductor materials) the sample loading is carried out in a glovebox under nitrogen atmosphere and the deflection fluid is purged with N_2 (Linde, 5.0) prior to use.

At start-up of the setup, the HeNe probe laser is typically set to its desired output power and switched on ca. 30 minutes before the desired start of the first measurement to allow stabilization of the laser output. To set up the measurement, the loaded cuvette is placed in the cuvette holder on the sample stage and fixed by a screw using a PTFE plate as spacer to avoid damaging the cuvette. Pump laser emission is then switched on and the AOTF output is tuned to a wavelength

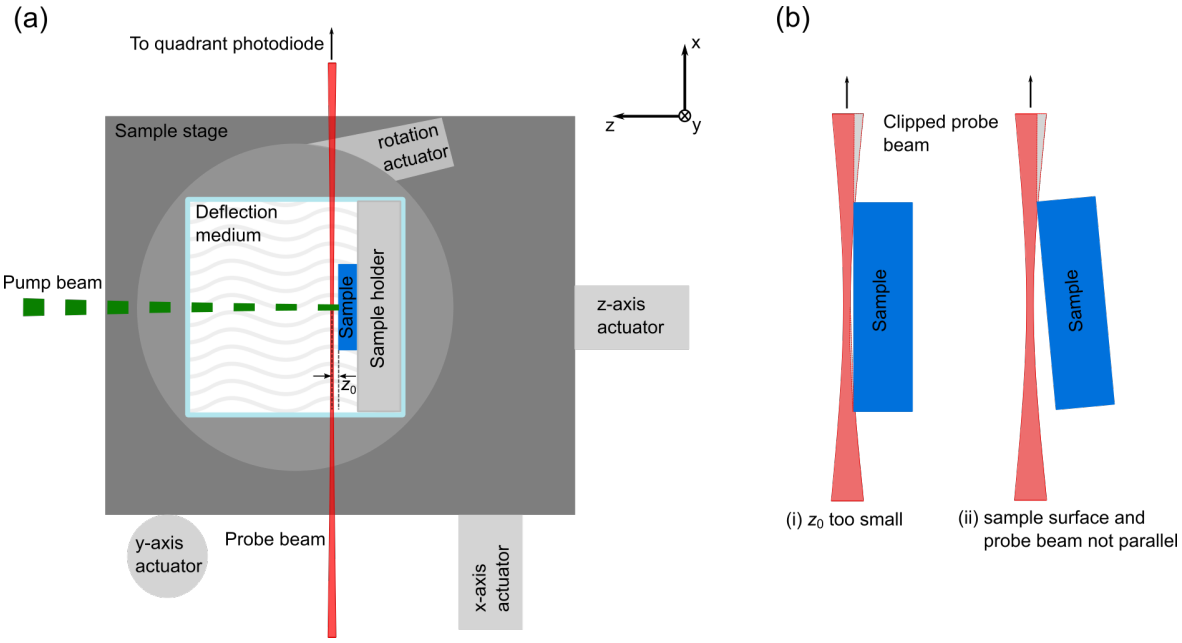

Figure 2.7. (a) Schematic representation of the sample stage with a loaded sample cuvette and incident pump and probe beams. The reference coordinate system and the positions of the actuators for adjustment of the x-, y-, z- and rotational position of the stage are shown. z_0 represents the distance between sample surface and center axis of the probe beam. **(b)** Schematic depiction of the possible causes of probe beam clipping due to sample misalignment.

where the sample exhibits medium to strong absorption. By adjusting the x- and y-positions of the sample stage the pump beam spot is moved to the desired position on the sample. The reference coordinate system and the corresponding actuators for positional adjustments of the sample stage are schematically shown in Fig. 2.7 (a). For fine-tuning of the alignment, the sample stage is moved along the z-axis (axis of pump beam propagation) to adjust the sample-probe beam distance z_0. Generally, the distance is set as low as possible to maximize the measured deflection signal (see section 1.2.2.1); however, it should not be decreased below the threshold at which probe beam clipping at the sample edges occurs, as shown in Fig. 2.7 (b) (i). This can be checked by monitoring the SUM signal at the Keithley multimeter, which decreases upon probe beam clipping. If necessary, also the rotational position of the cuvette must be adjusted to achieve parallelism of probe beam and sample surface in order to avoid beam clipping by a protruding edge which can further limit the minimal sample-probe beam distance (see Fig. 2.7 (b) (ii)).

After aligning the sample, a suitable set of parameters for the PDS measurement must be chosen. The following parameters need to be specified:

- Lock-in amplifier time constant τ
- Number N of data points averaged at each wavelength
- Waiting time t_1 before readout of the LIA output after a pump wavelength change
- Waiting time t_2 between the readout of individual data points at each wavelength
- Wavelength range
- Wavelength step size
- Relative pump laser power level

For all measurements in this work, a time constant of $\tau = 3$ s and waiting time $t_2 = \tau$ was used. The averaging number N and waiting time t_1 were chosen according to the desired wavelength step size. Typically, a step size of 5 nm with $N = 10$ and $t_1 = 10\,\tau$ was used. For PDS measurements which were used for the calculation of the photoluminescence quantum yield of samples, a wavelength step size of 1 nm and values of $N = 5$ and $t_1 = 5\,\tau$ were used to achieve a maximum wavelength resolution of the absorption profile while keeping a moderate measurement time to avoid damaging or altering the sample by prolonged irradiation. The wavelength range is set to the region of interest. To minimize a possible distortion of measured PDS spectra due to light-induced changes of the sample, the pump light is typically sweeped from wavelengths of low absorption to wavelengths of high absorption of the sample. Unless otherwise stated, all measurements included in this work were conducted at a pump laser power level of 100 % of its maximum power and a pump light chopping frequency of 1.7 Hz. A decrease of the pump laser power can be favourable for samples with low photostability.

Measurements which span the VIS and the NIR pump light spectrum (or parts thereof) of the setup, are conducted separately and require a manual change of the pump beam wavelength regime in the LabView control software and the adjustment of the slideable mirror shown in Fig. 2.1. During this change, the sample alignment should not be altered to allow the measured

VIS and NIR PDS spectra to be merged. For measurements which include the wavelength range of 1060 – 1070 nm, the large pump light power spike in this region, which leads to a signal overload of the photodiode signal at the LIA at any pump laser power, must be considered. To circumvent this signal overload, a neutral density filter (Thorlabs NDUV03A, OD = 0.3) is placed in the pump beam path after the AOTF output for measurements including this spectral range.

Before each individual measurement is started, the phase difference between the LIA reference signal and the deflection signal is zeroed by matching the reference signal phase. This allows better comparability of the phase of measured PDS signals. During the measurement, the X and Y output signals of the deflection signal lock-in amplifier, the photocurrent at the pump power monitor (signal amplitude at the photodiode lock-in amplifier) and the SUM signal of the position detector (signal on the Keithley 2700 digital multimeter) are recorded. For the measurement of the deflection signal, the X and Y output signals of the corresponding lock-in amplifier are recorded, as this allows an immediate indication if the measured signal in a certain wavelength region stems from sample light absorption or originates from noise, since the X and Y signals typically show a random oscillation around zero when the noise limit of the setup is reached.

To obtain a representative deflection spectrum for a certain sample, typically multiple measurements are carried out on different spots on the sample by varying the x- and y-positions and, if necessary, also the z-position of the sample cuvette between measurements and the individual spectra are averaged. The comparatively small pump light spot size can, however, also be used to selectively probe certain areas on the sample.

2.5.3. Data Analysis Procedure

2.5.3.1. Determination of Absorptance from PDS Measurements

From the X and Y output signals of the LIA, the amplitude S and phase θ of the raw deflection signal are calculated according to equations (2.5) and (2.6).

$$S = \sqrt{X^2 + Y^2} \tag{2.5}$$

$$\theta = \arctan2(X, Y) \tag{2.6}$$

The raw deflection spectrum must be corrected for the pump light power profile which is calculated from the photocurrent I_R measured at the pump power monitor and the beamsplitter correction factor C_BS. Additionally, the SUM signal of the PSD is included as a correction factor. The SUM- and pump light power-corrected deflection signal S_Corr is calculated according to eq. (2.7):

$$S_\mathrm{Corr} = \frac{S}{I_\mathrm{R}\, C_\mathrm{BS}\, \mathrm{SUM}} \tag{2.7}$$

Depending on the optical density of sample films, two different methods were applied to obtain absolute absorptance profiles from deflection spectra for samples with an efficiency of non-radiative decay of photoexcited states close to unity ($\eta_\mathrm{NR} \approx 1$). For an optically thick sample

which exhibits saturation of the deflection signal at a wavelength λ_{sat}, the absorptance can be determined by assuming a complete absorption of incident light with λ_{sat} which is not reflected at the sample surface, as expressed in equation (2.8).

$$A(\lambda_{\mathrm{sat}}) \approx 1 - R(\lambda_{\mathrm{sat}}) \tag{2.8}$$

Thus, the corrected deflection spectrum measured for the sample must be scaled to match the value of $1 - R(\lambda_{\mathrm{sat}})$ at wavelength λ_{sat} according to eq. (2.9) to obtain the absolute absorptance spectrum $A_{\mathrm{PDS}}(\lambda)$ from PDS data.

$$A_{\mathrm{PDS}}(\lambda) = [1 - R(\lambda_{\mathrm{sat}})] \frac{S_{\mathrm{Corr}}(\lambda)}{S_{\mathrm{Corr}}(\lambda_{\mathrm{sat}})} \tag{2.9}$$

The reflectance of the sample at λ_{sat} is determined by a separate measurement on a UV/Vis/NIR spectrophotometer (see section 2.3).

For optically thin samples that do not show saturation of the deflection signal at any wavelength, absolute absorptance spectra are determined by scaling the deflection spectra to absorptance values obtained from measurements on a UV/Vis/NIR spectrophotometer. Scaling of the deflection spectrum is performed at a wavelength λ_0 where the sample shows relatively strong light absorption and thus allows an accurate determination of its absorptance $A_{R/T}(\lambda_0)$ by conventional R and T measurements [115]. The absorptance is determined from the corrected deflection signal according to eq. (2.10).

$$A_{\mathrm{PDS}}(\lambda) = A_{R/T}(\lambda_0) \, \frac{S_{\mathrm{Corr}}(\lambda)}{S_{\mathrm{Corr}}(\lambda_0)} \tag{2.10}$$

In comparison to the determination of absorptance via signal saturation, this approach is poorly suitable for samples which exhibit significant light scattering due to the adverse effect of light scattering on the accuracy of absorptance values determined from R and T measurements.

2.5.3.2. Determination of the Absorption Coefficient

Knowledge of the absolute absorptance A and reflectance R of a sample film with thickness d allows the calculation of the absorption coefficient α. A simple expression for the approximation of α, assuming direct proportionality of α and A is shown in eq. (2.11) [8, 115].

$$\alpha = \frac{A}{d} \tag{2.11}$$

This assumption, however, is only a valid approximation for weakly absorbing regions where $\alpha d \ll 1$ applies [8]. Furthermore, eq. (2.11) disregards additional reflection effects besides the front surface reflectance. A more advanced relation which accounts for interference effects due to

multiple reflections of incident light within the film was developed by Ritter and Weiser [116]:

$$\alpha = \frac{1}{d}\ln\left(\frac{1}{2}\left[(1-R_2)(1+\frac{A}{T}) + \sqrt{(1-R_2)^2(1+\frac{A}{T})^2 + 4R_2}\,\right]\right) \tag{2.12}$$

Here T represents the transmittance ($T = 1 - A - R$) and R_2 represents the reflectance of the film-substrate interface [116]. For normal light incidence with respect to the interface, R_2 can be calculated from the complex refractive indices $n' = n - ik$ of the sample film, n'_{f}, and the substrate, n'_{s}, according to the Fresnel equation for normal light incidence shown in eq. (2.13) (derived from ref. [4]).

$$R_2 = \frac{(n_{\mathrm{s}} - n_{\mathrm{f}})^2 + (k_{\mathrm{s}} - k_{\mathrm{f}})^2}{(n_{\mathrm{s}} + n_{\mathrm{f}})^2 + (k_{\mathrm{s}} + k_{\mathrm{f}})^2} \tag{2.13}$$

For a transparent substrate and a weakly to moderately absorbing film ($k \ll n$), eq. (2.13) can be simplified to yield equation (2.14) [112, 115].

$$R_2 = \frac{(n_{\mathrm{s}} - n_{\mathrm{f}})^2}{(n_{\mathrm{s}} + n_{\mathrm{f}})^2} \tag{2.14}$$

Alternatively, if the difference between the refractive indices of film and substrate is not particularly large, the expression developed by Ritter and Weiser can be simplified by disregarding the film-substrate reflectance R_2 to yield eq. (2.15) which allows calculation of α without knowledge of the refractive indices of film and substrate.

$$\alpha = \frac{1}{d}\ln\left(1 + \frac{A}{T}\right) \tag{2.15}$$

To assess and compare the accuracies of the calculation methods, the theoretical absorptance spectrum of a methylammonium lead iodide ($MAPbI_3$) film on a quartz substrate in air (refractive index of air: $n_0 \approx 1$) was calculated from reported values of n and k of $MAPbI_3$ [117] and n_s of quartz [100] according to an equation given by Ritter and Weiser [116] (see Appendix A.1). From the calculated absorptance of films with different thicknesses, the absorption coefficient is calculated according to eqs. (2.11), (2.12) and (2.15), respectively and compared to its exact value determined from the relation $\alpha = 4\pi k\lambda^{-1}$ [116]. The comparison for films with thicknesses of 20 nm and 500 nm is shown in Fig. 2.8. While the simple expression $\alpha = Ad^{-1}$ offers a good approximation for the low film thickness, it heavily deviates from the exact α values at higher d and does not take interference phenomena into account. The expression developed by Ritter and Weiser, as well as its simplified version, show very good conformity to the exact absorption coefficient at both film thicknesses. Since for the majority of investigated materials the wavelength-dependent refractive index data were not known, eq. (2.15) was applied for calculation of α of sample films.

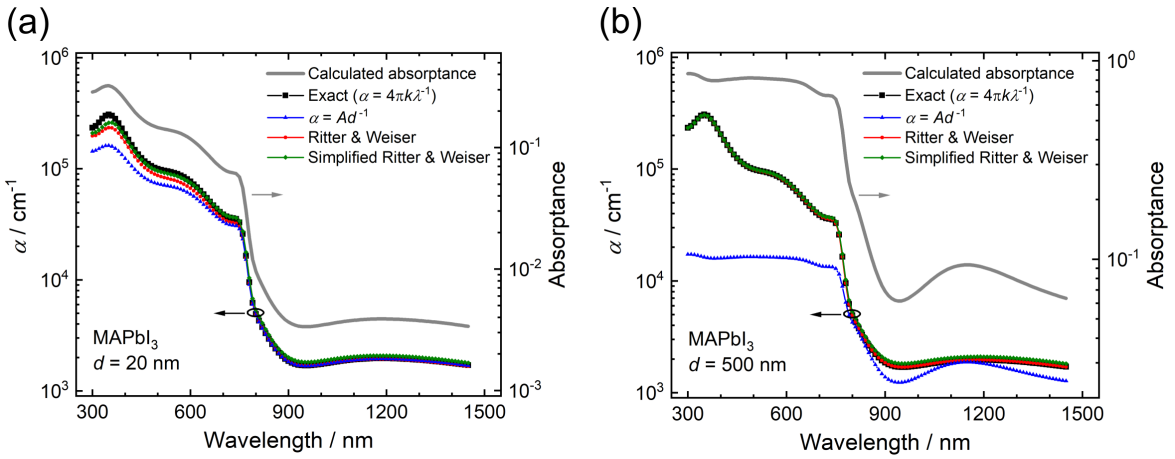

Figure 2.8. Comparison of absorption coefficient spectra determined with the formulas given in equations (2.11) (blue triangles), (2.12) (red circles) and (2.15) (green rhomboids) from absorptance spectra calculated for $MAPbI_3$ films on quartz with film thicknesses of **(a)** 20 nm and **(b)** 500 nm. Calculation of absorptance is based on the formula stated by Ritter and Weiser [116], using reported values for n and k of $MAPbI_3$ [117] and n_s of quartz [100] (see Appendix A.1). The exact values of α (black squares) are determined from k of $MAPbI_3$.

2.5.4. Validation of the PDS System

To verify the correct functionality of the assembled PDS setup and the measurement and data analysis procedure, a validation of the system was carried out by measurement of an optically well-characterized reference material and comparison of the determined absorption coefficient with values reported in literature.

Copper(II) phthalocyanine (CuPc) was used as reference material because its absorption coefficient has been reported for the wavelength range of interest (450 –1100 nm) [40, 118] and due to its high chemical and thermal stability, as well as the possibility for the straightforward preparation of high purity thin films by thermal evaporation [118, 119].

2.5.5. Photoluminescence Quantum Yield Determination

The photoluminescence quantum yields (PLQY, η_{PL}) of strongly luminescent films of methylammonium lead(II) bromide ($MAPbBr_3$) perovskite nanoparticles (PNP) and a film of PS doped with PDI, was determined by comparison of the corrected deflection spectrum with the corresponding absorptance spectrum of the films in analogy to methods reported by Jackson and Nemanich [53], Fernandez *et al.* [32] and Couch *et al.* [36].

As discussed in section 1.2.2.3, the occurence of photoluminescence as non-thermal relaxation pathway of photoexcited states leads to a PLQY- and mean PL energy-dependent deviation of the deflection spectrum from the absorptance profile of a material. From eq. (1.11) ($\frac{S}{\Phi_i}$ corresponds to the pump spectrum-corrected deflection signal) eq. (2.16) can be derived, which relates the corrected deflection signal S_{Corr}, measured at pump light photon energy E, with the relative absorptance a, the PLQY η_{PL} and the mean energy of the emitted photons $\overline{E}_{\mathrm{PL}}$ [32, 36].

$$\frac{S_{\mathrm{Corr}}(E)}{a(E)} = B'\left(1 - \eta_{\mathrm{PL}}\frac{\overline{E}_{\mathrm{PL}}}{E}\right) \tag{2.16}$$

Here, B' represents a proportionality factor. The mean PL energy $\overline{E}_{\mathrm{PL}}$ can be determined from the PL intensity Φ_i at a photon energy E_i according to eq. (2.17) [36].

$$\overline{E}_{\mathrm{PL}} = \frac{\sum\limits_i \Phi_i E_i}{\sum\limits_i \Phi_i} \tag{2.17}$$

With the relation $E = h\,c\,\lambda^{-1}$, the mean wavelength of the PL spectrum $\overline{\lambda}_{\mathrm{PL}}$ can be determined and eq. (2.16) can be transformed to equation (2.18).

$$\frac{S_{\mathrm{Corr}}(\lambda)}{a(\lambda)} = B'\left(1 - \eta_{\mathrm{PL}}\frac{\lambda}{\overline{\lambda}_{\mathrm{PL}}}\right) \tag{2.18}$$

Equation (2.18) shows a linear dependence of the quotient of corrected deflection signal and absorptance on the pump light wavelength. From the slope and intercept of a linear fitting function in a corresponding plot, the PLQY of a sample film can be determined. Since any wavelength-independent scaling factor will be contained in the multiplicative constant B', the quantity $a(\lambda)$ used for the evaluation must be directly proportional to the absolute absorptance A of the sample but does not need to correspond to its absolute values.

For the investigated PNP films, the absorption profiles $a(\lambda)$ were determined by photoluminescence excitation (PLE) measurements, due to the very strong light scattering of the samples which heavily distort transmittance spectra. PLE spectra (corrected for the excitation light quanta at each wavelength) are directly proportional to the absorptance spectrum of a material [120] under assumption of an excitation wavelength-independent PLQY in the investigated wavelength range as implied by the widely valid rule of Vavilov [26, 121]. The absorptance profile of the investigated PDI/PS film was determined by reflectance and transmittance measurements on the Lambda1050 spectrophotometer. $\overline{\lambda}_{\mathrm{PL}}$ was calculated from the mean PL energy, determined via eq. (2.17) from PL measurements of the sample films. For the transformation of the measured PL spectrum from the wavelength to the photon energy domain, the Jacobian transformation factor $h\,c\,E^{-2}$ was used to scale the signal intensity values [122].

For an accurate calculation the wavelength scales of the pump/excitation light of the PDS setup, the PTI QuantaMaster spectrofluorometer and the PerkinElmer Lambda1050 spectrophotometer must be matched. To examine the conformity, a pump wavelength sweep was carried out on the PDS setup in the configuration shown in Fig. 2.5, with a 495 nm bandpass (BP) filter placed in the pump light path. Similarily, a PLE measurement of a strongly fluorescent $MAPbBr_3$ nanoparticle film with the same BP filter placed in the excitation light path was carried out. The measured signal was corrected with the PLE spectrum of the film measured without filter. Additionally, a blank transmittance spectrum was measured on the Lambda 1050 spectrophotometer with the 495 nm BP filter placed in the light path. Figure 2.9 shows the normalized pump power spectrum of the PDS setup, the corrected PLE spectrum and the transmittance spectrum measured with bandpass filter. While the spectra measured on the PDS setup and the spectrophotometer show excellent conformity and correct position of the peak at 495 nm, the PLE spectrum shows a deviation of the

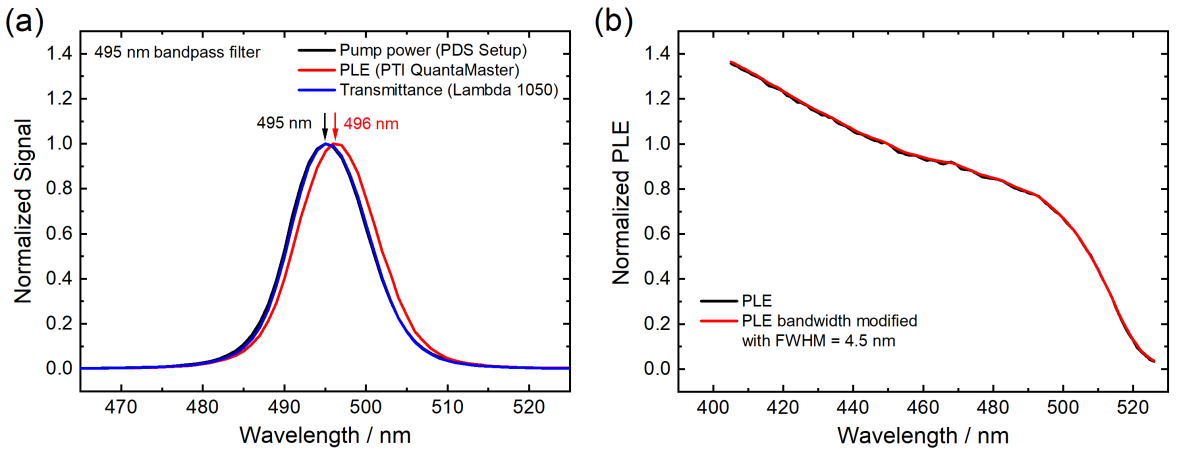

Figure 2.9. (a) Comparison of normalized pump light power (PDS setup), photoluminescence excitation spectrum of a $MAPbBr_3$ nanoparticle film (PTI QuantaMaster, emission measured at 530 nm) and transmittance spectrum (PerkinElmer Lambda 1050 spectrophotometer) measured with a 495 nm bandpass filter placed in the pump/excitation light path. The photoluminescence excitation spectrum was corrected with the PLE spectrum measured for the film under the same experimental conditions without BP filter. **(b)** Comparison of the unmodified PLE spectrum and PLE spectrum modified via equation (2.20) for an excitation light FWHM of $w = 4.5$ nm, using $\Delta\lambda^* = 0.5$ nm, of a $MAPbBr_3$ nanoparticle film.

wavelength scale of ca. 1 nm from the central wavelength of 495 nm. Thus, PLE spectra recorded on the PTI QuantaMaster spectrofluorometer were shifted by $\lambda - 1$.

In cases where the pump light output of the PDS system shows a considerably larger FWHM than the excitaton light of the used spectrofluorometer or spectrophotometer, the spectral broadening of the measured PDS spectra can be accounted for by modifying the PLE or absorptance spectra $a(\lambda)$ with a Gaussian excitation light profile with the FWHM w of the PDS pump light bands over the investigated wavelength range λ_1 to λ_n as follows [36]:

$$a_{\text{corrected}}(\lambda) = \int_{\lambda_1}^{\lambda_n} a(\lambda^*) e^{-4\ln(2)\frac{(\lambda^*-\lambda)^2}{w^2}} d\lambda^* \tag{2.19}$$

The integral in eq. (2.19) can be approximated by a finite sum with a width of summands of $\Delta\lambda^*$ to yield eq. (2.20).

$$a_{\text{corrected}}(\lambda) = \sum_{\lambda^*=\lambda_1}^{\lambda_n} a(\lambda^*) e^{-4\ln(2)\frac{(\lambda^*-\lambda)^2}{w^2}} \Delta\lambda^* \tag{2.20}$$

However, since the used PDS setup shows relatively narrow pump light bandwidths in the typically investigated wavelength range of 450 – 550 nm (see Fig. 2.2) for $MAPbBr_3$ PNP films and the PDI/PS film, the effect of this correction is negligibly small, as can be seen in Fig. 2.9 which shows a comparison of the uncorrected and the by eq. (2.20) corrected PLE spectra of a PNP film. Thus, no bandwidth correction was applied for the spectra used for the PLQY determination of the sample films. Upon change to a pump light source with a larger spectral bandwidth, the bandwidth correction should be applied though to reach a higher accuracy of the PLQY determination.

2.5.6. Determination of the Urbach Energy

The Urbach energy of a $MAPbI_{3-x}Cl_x$ film on fused quartz was determined from the absorption coefficient spectrum measured for the film by PDS and $R\,\&\,T$ measurements. The absorption coefficient spectrum $\alpha(E)$ in the band tail region at energies E below the bandgap energy can be expressed by an exponential function according to eq. (2.21), where α_0 and E_0 are material parameters and E_U is the Urbach energy [2].

$$\alpha(E) = \alpha_0 \, e^{\frac{E-E_0}{E_\mathrm{U}}} \tag{2.21}$$

Taking the natural logarithm, eq. (2.21) can be transformed to eq. (2.22).

$$\ln(\alpha(E)) = \ln(\alpha_0) - \frac{E_0}{E_\mathrm{U}} + \frac{1}{E_\mathrm{U}} E \tag{2.22}$$

The Urbach energy of a sample can thus be determined from its absorption coefficient spectrum by plotting $\ln(\alpha)$ versus the photon energy E and using a linear function to fit the data below the bandgap energy of the material. The reciprocal value of the slope of the linear fit corresponds to the Urbach energy.

3. Results

3.1. Characterization and Validation of the PDS Setup

3.1.1. Noise Measurements

In order to evaluate the influence of different measurement conditions and the impact of optimization measures on the noise limit of the assembled PDS setup, measurements of the setup noise level were carried out under different conditions by measuring the X and Y lock-in amplifier output signals of the deflection signal. The measurements were carried out under the typically used LIA measurement parameters of $\tau = 3$ s and $N = 10$ (see section 2.5.2). The first set of noise measurements were carried out without pump light and without placing a sample holder or sample in the cuvette for the measurements where the cuvette was inserted in the setup. Additional noise measurements were carried out under typical measurement conditions by inserting the sample holder mounted with a fused quartz sample in the cuvette and applying pump light at a power level of 100 %. The results of the measurements are displayed as histograms in Fig. 3.1 and Fig. 3.2 (a), respectively. On the x-axis the SUM-corrected X output signal of the LIA (SUM is the total voltage signal measured on the quadrat photodiode in V; X measured in mV) is plotted in bins with a constant width of 5×10^{-4} mV V^{-1} versus the absolute frequency of the corresponding values measured in a total of 200 measurement points. The data are fitted by a Gaussian function and the standard deviation σ is given for all fitting curves. For all measurements also the corresponding Y LIA output values were evaluated and found to show noise distributions equal to those of the X values. Thus, only the noise distributions determined for the X values are plotted for the sake of clarity.

Figure 3.1 (a) shows the noise histograms for measurements carried out at a chopping frequency of $\omega = 1.7$ Hz, without a cuvette inserted in the setup and with the top lid of the setup enclosing box opened or closed. Fig. 3.1 (b) displays the noise measured at chopping frequencies of 1.7 Hz and 7.0 Hz, respectively, measured without cuvette and with the lid of the box closed. Fig. 3.1 (c) shows the comparison of the noise level measured without the sample cuvette and with the cuvette containing the deflection medium (Flutec PP9) at closed box and at $\omega = 1.7$ Hz. Fig. 3.1 (d) shows the noise histograms obtained from measurements with an empty cuvette and with the cuvette filled with deflection medium, measured at closed box and $\omega = 1.7$ Hz. In Fig. 3.2 (a) the X/SUM noise distribution measured under typical measurement conditions of $\omega = 1.7$ Hz, closed box and 100 % pump light power, using a sample of fused quartz in the setup, is shown. Fig. 3.2 (b) shows X signal and SUM signal spectra measured in the noise measurements with the fused quartz sample.

The results in Fig. 3.1 (a) show a significantly increased spread of X values measured with an opened box as compared to a closed box, with a more than twice as large standard deviation of data around the mean value of ca. zero, as obtained from the corresponding Gaussian fits,

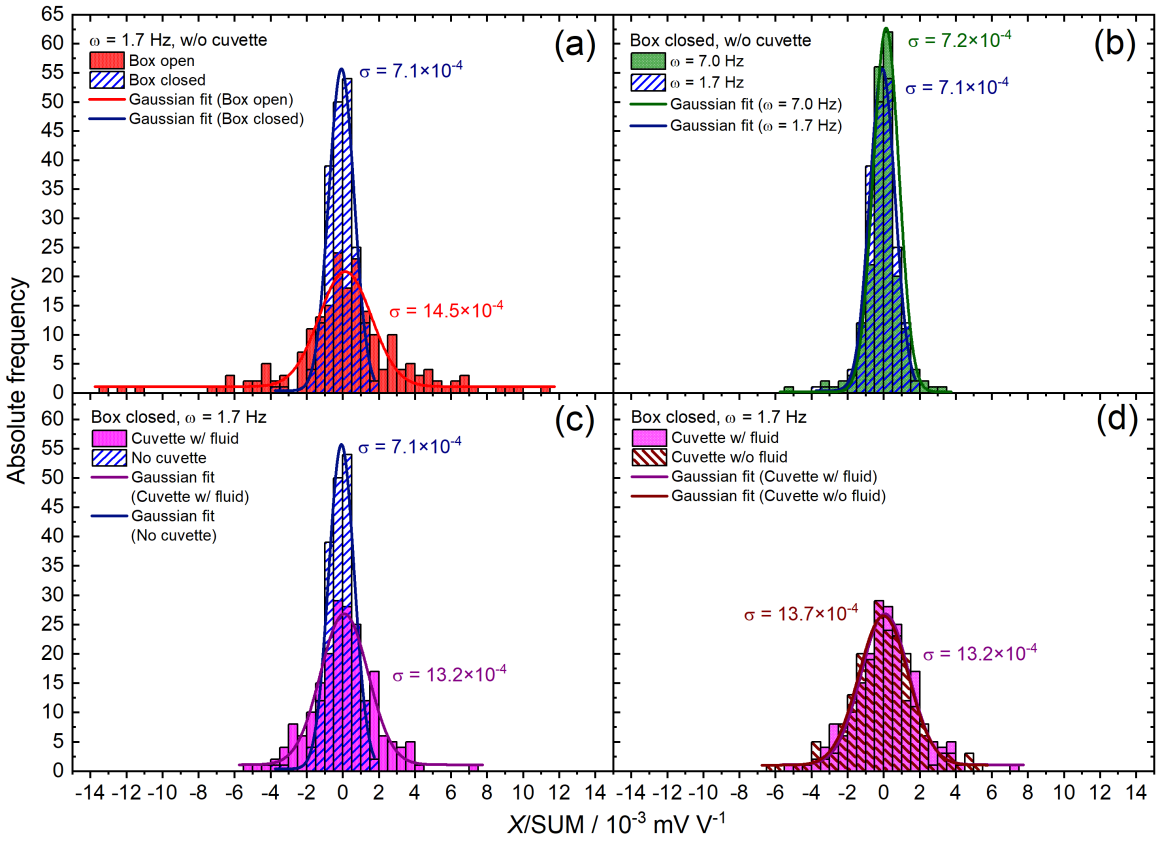

Figure 3.1. Probe beam noise histograms from measurements conducted under different conditions. The measured noise is plotted on the x-axis as the SUM-corrected X output signal of the lock-in amplifier in bins of a width of 5×10^{-4} mV V^{-1}. On the y-axis the absolute frequency of values contained in a bin among a total of 200 measurement points is plotted. The histograms are fitted with Gaussian functions and the standard deviations σ of the distribution functions are listed. The measurement conditions applied in **(a)**, **(b)**, **(c)** and **(d)** are stated in top left side of each diagram. All measurements were carried out without pump light and without a sample holder in the cuvette.

and a maximum noise value 3.7 times larger than the one measured at a closed box. This indicates the significant impact of the setup isolation by the enclosure, which can be attributed to shielding of the PDS setup from air flow, floating dust particles and external light. In contrast to the positive effect of higher chopping frequencies due to filtering of mechanical vibrations proposed in reference works [8, 95], Fig. 3.1 (b) shows that an increase of the chopping frequency from 1.7 Hz to 7.0 Hz showed no impact on the noise level of the probe beam in the PDS setup. These results support the use of the low frequency of 1.7 Hz which allows to significantly increase the maximally obtainable deflection signal during PDS measurements in comparison to $\omega = 7.0$ Hz and thus enables an increase of the signal-to-noise ratio of the setup.

A clear increase of the noise level is observed upon insertion of the deflection fluid-filled cuvette into the setup, as shown in Fig. 3.1 (c) where a broadening of the noise distribution and significant increase of the standard deviation can be observed. Initially it was assumed that this increase in noise results from small temperature gradients which can cause turbulence in the fluid or a higher susceptibility to vibrational noise of the deflection fluid. However, no significant difference in the noise distribution measured with an empty cuvette or with the cuvette filled with

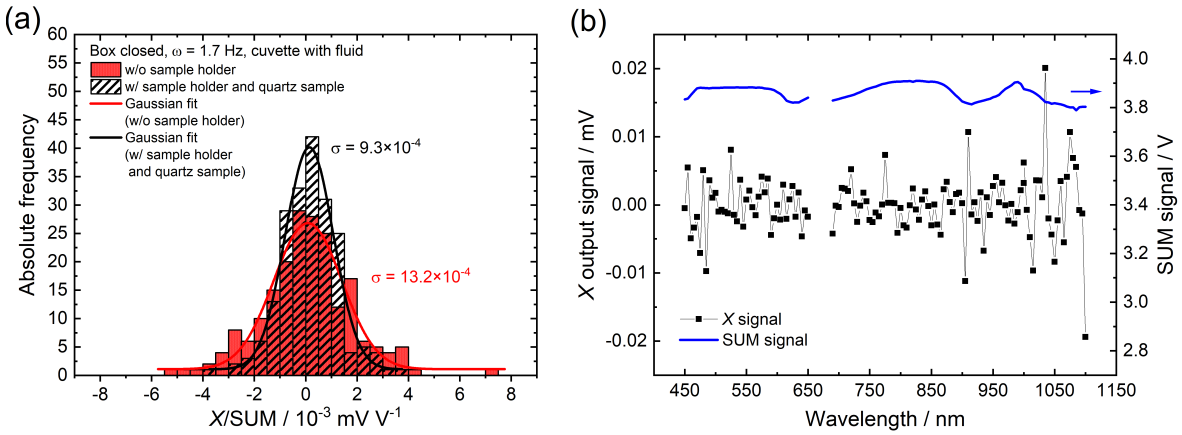

Figure 3.2. (a) Probe beam noise histograms from measurements conducted under typical measurement conditions as stated in the top left of the diagram, without a sample holder (red) and with sample holder A mounted with a fused quartz sample (black). The absolute frequency in total of 200 measurement points is plotted versus the SUM-corrected X output signal of the lock-in amplifier in bins of a width of 5×10^{-4} mV V^{-1}. **(b)** X output signal and SUM signal spectra of a noise measurement with a fused quartz sample under the measurement conditions stated in (a).

deflection fluid was observed, as displayed in Fig. 3.1 (d). This suggests that the increase in probe beam noise is induced by the cuvette alone and might be due to stray light from probe light reflections on the cuvette. Interestingly, however, the noise measurements with a fused quartz sample and with pump light illumination displayed in Fig. 3.2 (a), show a reduction of noise upon introduction of a sample in the cuvette. This supports the assumption that the initial increase in noise upon introduction of the cuvette stems from turbulence in the deflection fluid since a restriction of the fluid flow and decrease of the fluid volume inside the cuvette is proposed to decrease the susceptibility of the fluid to turbulence [8]. However, a detailed elucidation of this phenomenon requires further investigation.

The noise measurements with a quartz sample displayed in Fig. 3.2 represent the noise limit of the PDS setup under typical measurement conditions, which correspond to a raw X output signal of typically $\pm\,0.002-0.005$ mV at a SUM signal of ca. 3.85 V, with single spikes to values of up to $\pm\,0.02$ mV which are probably due to external disturbances of the setup.

3.1.2. Comparison of Substrates for PDS

In preliminary PDS measurements it was observed that certain transparent substrate materials show weak light absorption over a broad wavelength range, which can mask sample light absorption and limit the lowest measurable absorptance of sample films. Thus, several commonly used substrate materials for thin films were investigated by PDS to determine the deflection signal resulting from their residual light absorption and allow the evaluation of their suitability for specific PDS measurement tasks. The investigated materials comprise fused quartz, soda lime glass (Marienfeld microscope slides), ca. 900 nm thick films of PS and PMMA deposited on fused quartz via blade coating, as well as films of indium tin oxide (ITO) and PEDOT:PSS on glass. Fig. 3.3 (a) shows the average corrected deflection signal determined for the investigated materials. In Fig. 3.3 (b) the corresponding average raw X output signals of the lock-in amplifier recorded in the PDS measurements of fused quartz, soda lime glass, PS and PMMA are displayed.

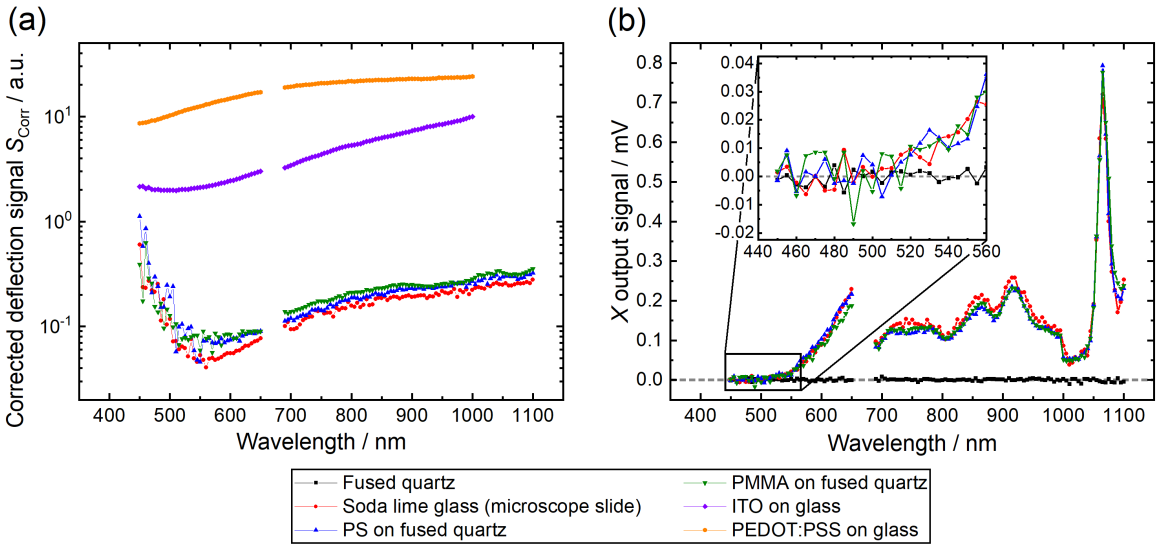

Figure 3.3. **(a)** Corrected deflection signal S_{Corr} of different substrate materials determined from PDS measurements of soda lime glass (Marienfeld microscope slides), bladecoated films of PS and PMMA on fused quartz and films of ITO and PEDOT:PSS on glass. No reliable determination of S_{Corr} was possible for fused quartz since its deflection signal was below the noise limit of the setup as shown in figure (b). **(b)** Raw X output signal of the deflection signal lock-in amplifier from the PDS measurements of fused quartz, soda lime glass as well as PS and PMMA films on fused quartz. The *inset* shows a magnification of the region from 450 nm to 560 nm, in which the limitation of the measurements by the noise limit of the setup is observable as variation of the X value around zero.

While films of PEDOT:PSS and ITO show a much stronger light absorption than the other investigated materials and thus gave significantly higher corrected deflection signals, comparatively high signals were also measured for PMMA, PS and soda lime glass, which show relatively similar values of S_{Corr}, that increase from wavelengths of 560 nm to 1100 nm. Fused quartz, on the other hand, showed no measureable deflection signal above the noise level of the PDS setup as is shown by the oscillation of the measured X output signal of the LIA around zero over the whole investigated wavelength range, displayed in Fig. 3.3 (b). An analogous behavior was observed for the Y LIA output signal. Thus, no accurate deflection signal could be determined for fused quartz.

The inset of Figure 3.3 (b) shows that the limitation of the measurement by the noise level of the setup, and thus variation of X around zero, also occurred for soda lime glass, PS and PMMA at wavelengths of 450 nm to 520 nm. This behavior can be attributed to the relatively low pump light power in this wavelength region (see Fig. 2.2) which could likely be insufficient to generate a measureable deflection signal from the weakly absorbing materials. Consequently, also the corresponding S_{Corr} profiles at 450 – 520 nm displayed in Fig. 3.3 (a) for soda lime glass, PS and PMMA show heavy fluctuations and are inaccurate. The form of the S_{Corr} profiles determined for this wavelength regime roughly resemble the inverted pump light power spectrum and result from the pump light power profile correction in the calculation of S_{Corr} (see section 2.5.3.1). Reliable spectra for these materials were obtained at wavelengths of $\lambda \geq 560$ nm. In the region between 520 nm and 560 nm, exclusively positive, with the wavelength increasing values of the LIA X signal were measured, which are however roughly at or only slightly above the maximum noise level,

as shown in the inset of Fig. 3.3 (b). Thus, the reliability of the S_{Corr} values determined for this wavelength region is low.

The measured deflection spectra show that no detectable light absorption was found for fused quartz, making it an ideal substrate for highly sensitive measurements of weakly absorbing sample materials. For soda lime glass, PS and PMMA a considerable residual light absorption was found, resulting in an accurately measurable corrected deflection signal at wavelengths above 560 nm. These materials thus are suitable as substrate or matrix materials for PDS measurements of samples that show moderate to strong light absorption in the wavelength range of interest, can however be a limiting factor for measurement of low sample absorptances. For sample films deposited onto ITO or PEDOT:PSS, the relatively high deflection signal contribution of both materials must be considered. The S_{Corr} spectra determined for ITO and PEDOT:PSS match the shapes of the absorption profiles which have been reported for these materials [123, 124].

3.1.3. Determination of the Sensitivity Limit of the Setup

To allow the estimation of the sensitivity limit (lowest measureable absorptance) of the assembled PDS setup for the measurements of thin films, a spin coated film of the material IT-4F with a thickness of 25 nm on fused quartz (see Table 2.1) was investigated via PDS and $R\,\&\,T$ measurements.

Figure 3.4 (a) shows the amplitude S and phase θ of the raw deflection signal (see eqs. (2.5) and (2.6)) measured for the IT-4F film together with S calculated from measurements of fused quartz. It must be considered that, as discussed in section 3.1.2, fused quartz shows no measureable deflection signal above the setup noise level, thus the value of S merely represents the root of the sum of squared noise but was calculated for the sake of comparability. Comparison of the $S(\lambda)$ spectra of IT-4F on fused quartz and neat fused quartz shows that the deflection signal of

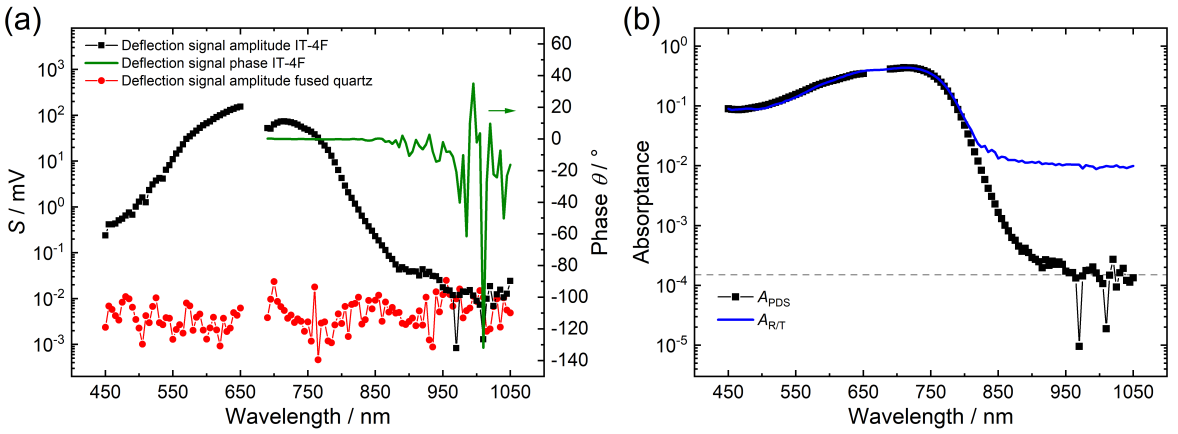

Figure 3.4. **(a)** Amplitude S and phase θ of the deflection signal spectrum measured for a 25 nm thick film of IT-4F spin coated on fused quartz and signal S determined from PDS measurements of neat fused quartz. In the case of fused quartz and for IT-4F at wavelengths above 950 nm, S represents the root of the sum of squared noise values and not an actual deflection signal as the positive values would suggest. **(b)** Absorptance spectra as determined from $R\,\&\,T$ measurements ($A_{\mathrm{R/T}}$) and PDS (A_{PDS}). A_{PDS} was determined by scaling the corrected deflection signal measured for the film to $A_{\mathrm{R/T}}$ at 720 nm. The sensitivity limit of the PDS setup corresponds to a minimal absorptance value of ca. 1.5×10^{-4} as shown by the dashed grey line.

IT-4F decreases roughly down to the level of fused quartz at wavelengths of 950 – 1050 nm, thus reaching the noise limit of the PDS setup. This is also clearly indicated by the considerable more fluctuating values of S and the strongly varying phase θ of the deflection signal in this wavelength region.

To determine the absolute absorptance value at which the noise limit is reached in the measurement of the film, the raw deflection spectrum $S(\lambda)$ was corrected according to eq. (2.7) and scaled to the absorptance spectrum $A_{\mathrm{R/T}}$, determined from reflectance and transmittance measurements, at a wavelength of 720 nm. The scaled absorptance spectrum A_{PDS} from PDS and $A_{\mathrm{R/T}}$ are displayed in Fig. 3.4 (b) and show very high conformity in the regions of high absorption, but deviate strongly in the high wavelength (sub-bandgap) region of the spectra above 815 nm. This can be attributed to the limitation of the accuracy of $A_{\mathrm{R/T}}$ at low absorptance values due to the far lower sensitivity of the R and T method as compared to PDS. The region where the spectrum of the IT-4F film reaches the noise level occurs at absorptance values of ca. 1.5×10^{-4}. This level is in very good agreement with the minimal absorptance measured for other samples (see section 3.3). Thus, the PDS setup shows a sensitivity limit of $A \approx 10^{-4}$. The lowest measureable absorption coefficient for sample films depends on the film thickness but can reach down to values of 1 cm^{-1} for films prepared by drop casting or blade coating, as shown in section 3.4.1.

3.1.4. Validation of the PDS Setup

For the validation of the PDS setup, the absorptance spectrum of a CuPc film deposited on fused quartz by thermal evaporation was measured on the PDS setup and a UV/Vis/NIR spectrophotometer. Figure 3.5 (a) shows the absorptance spectrum $A_{\mathrm{R/T}}(\lambda)$ of the film determined via R and T measurements, as well as the corresponding reflectance spectrum and the absorptance

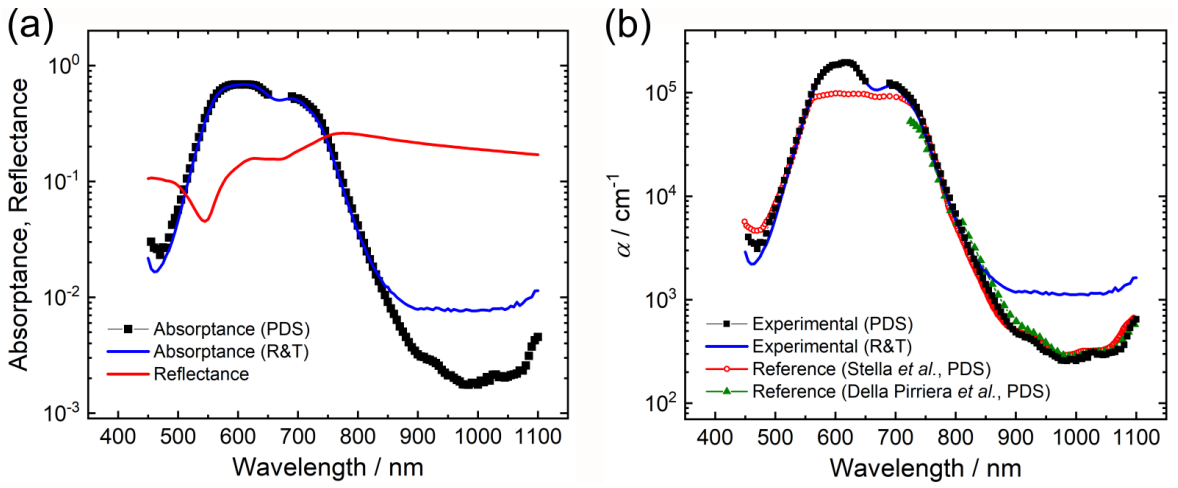

Figure 3.5. (a) Experimentally measured absorptance and reflectance spectra of a CuPc film on fused quartz, determined from reflectance (red solid curve) and transmittance measurements on a spectrophotometer ($A_{\mathrm{R/T}}$, blue solid curve) and from PDS (A_{PDS}, black squares). A_{PDS} was obtained by scaling the corrected deflection signal to match the $A_{\mathrm{R/T}}$ value at a wavelength of 610 nm. **(b)** Comparison of the experimentally determined absorption coefficient $\alpha(\lambda)$ spectra calculated via eq. (2.15) from A_{PDS} and $A_{\mathrm{R/T}}$, with reference data determined from PDS measurements by Stella *et al.* [40] and Della Pirriera *et al.* [118].

spectrum $A_{\mathrm{PDS}}(\lambda)$ determined from PDS measurements. $A_{\mathrm{PDS}}(\lambda)$ was obtained from the corrected deflection signal measured for the film by scaling to match $A_{\mathrm{R/T}}$ at the peak wavelength of 610 nm. The scaled deflection spectrum shows very good conformity with the absorptance spectrum determined from R and T measurements around the region of the intense absorption bands of the material. At wavelengths larger than 840 nm the absorptance spectra heavily deviate from each other, which can be attributed to the large difference in sensitivity of the R and T method in comparison to PDS, as discussed before.

From R, A_{PDS} or $A_{\mathrm{R/T}}$ and the mean film thickness d = 85 nm, the absorption coefficient of the CuPc film was calculated via eq. (2.15). The absorption coefficient spectra $\alpha(\lambda)$ determined from PDS and R & T measurements, respectively are shown in Fig. 3.5 (b). For the validation of the used PDS setup, the experimentally measured absorption coefficient spectrum was compared to values of α determined by Stella *et al.* [40] and Della Pirriera *et al.* [118] from PDS measurements.

The measured $\alpha(\lambda)$ spectrum shows very high conformity to the reference data in the regions of moderate to low absorption at $\lambda \geq 740$ nm and from 490 nm to 560 nm. A significant deviation of the experimental data and the absorption coefficient reported by Stella *et al.* [40] can be observed in the central wavelength region of 560 –730 nm around the intense absorption peaks at 615 nm and 690 nm. Since the data in ref. [40] were determined from PDS measurements, the discrepancy between the experimentally measured values and the reference data could result from the masking of the actual α profile due to deflection signal saturation in this wavelength region, which is suggested by the flat absorption profile of the reference spectrum. This is plausible due to the high thickness of 1 µm of the film used in ref. [40], which in conjunction with the high absorption coefficient of CuPc at its intense absorption bands is very likely to lead to a PDS signal saturation. An indication for the validity of the experimentally measured α profile in this wavelength region is the excellent conformity with the spectrum determined from R and T measurements. Furthermore, the measured absorption coefficient at 615 nm of $\alpha_{\mathrm{PDS}} = 1.96 \times 10^5$ cm^{-1}, shows good agreement with the value of $\alpha = 1.84 \times 10^5$ cm^{-1}, calculated from the imaginary part of the refractive index, k(615 nm) = 0.90, determined by Liu *et al.* [125] from spectroscopic ellipsometry measurements.

The high conformity of the experimentally determined α spectra with corresponding literature data indicates validity and correct functionality of the assembled PDS setup and the measurement and data analysis procedure.

3.1.5. Comparison of Deflection Fluids

The perfluorinated hydrocarbons listed in Table 2.2 were examined for their suitability as deflection fluids in the assembled PDS setup. The different fluids were tested in PDS measurements of a copper(II) phthalocyanine film. Since the measured deflection signal is highly dependent on the sample alignment and the sample-probe beam offset, particular attention was paid to reproduce a constant alignment in each measurement. This was done by keeping the position of the measured spot on the sample (x- and y-position of the cuvette) constant throughout all measurements and by carefully maximizing the deflection signal by varying the sample-probe beam offset without probe beam clipping before each measurement. For each fluid, several measurements were conducted

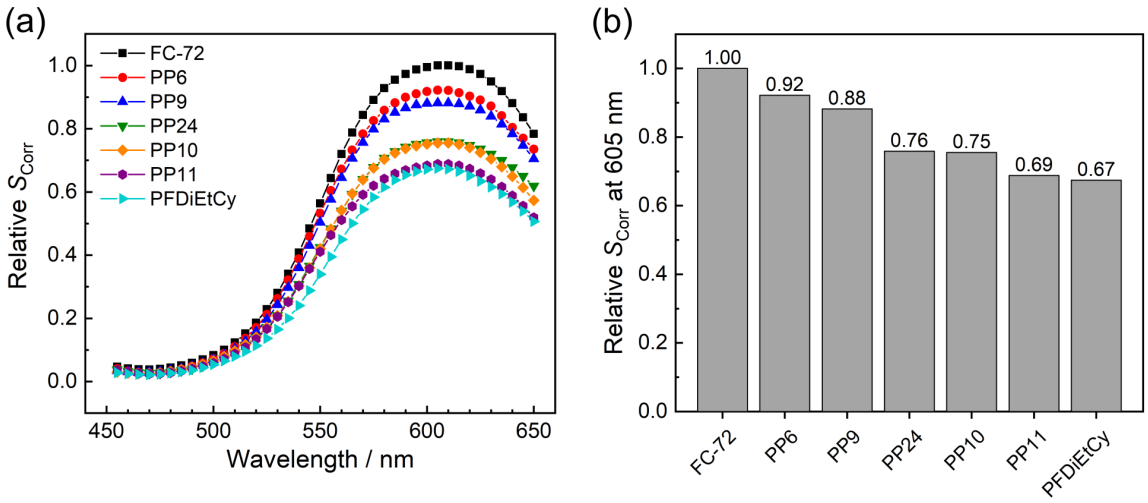

Figure 3.6. **(a)** Comparison of the corrected deflection spectra $S_{\mathrm{Corr}}(\lambda)$ of a CuPc film measured with different deflection fluids (see Table 2.2). Values of S_{Corr} are given relative to the peak corrected deflection signal determined for Fluorinert FC-72 at 605 nm. **(b)** Comparison of the corrected deflection signal amplitudes of the PDS spectra shown in (a) at the peak wavelength of 605 nm.

in this manner and the spectra with the highest signal were used for the comparison.

The corrected deflection spectra (S_{Corr}) that were determined using the different fluids are shown in Fig. 3.6 (a). For better comparability, the corrected deflection spectra are given relative to the peak signal of Fluorinert FC-72. Figure 3.6 (b) shows the relative corrected deflection signals at the peak wavelength of 605 nm, extracted from the corresponding spectra. The comparison shows that the highest deflection signal was obtained with the highly volatile FC-72 fluid. In comparison to FC-72, the Flutec variants with high boiling point and very low vapor pressure (PP10, PP11 and PP24) and the intermediate fluid perfluoro(1,3-diethylcyclohexane) displayed a clearly reduced deflection signal, whereas the perfluorinated decalin derivatives PP6 and PP9 show only slightly lower performances. While the differences in S_{Corr} between the two fluids are only small, a slightly higher volatility was found for PP6 in comparison to PP9. A noticeable evaporation loss of liquid after six days occured in the case of PP6, whereas no visible decrease of the liquid level in the cuvette over a period of more than 12 days was observed for PP9. Thus, Flutec PP9 was chosen as the deflection fluid for further measurements on the setup due to its superior balance between performance and low volatility.

3.2. Photoluminescence Quantum Yield Determination

3.2.1. Perovskite Nanoparticle Films

Four different highly luminescent $MAPbBr_3$ perovskite nanoparticle (PNP) films were investigated with photoluminescence spectroscopy and photothermal deflection spectroscopy (PDS). Three of the films were measured shortly (one day) after preparation and deposition of the corresponding PNPs, whereas one of the three films and a fourth film were measured after a considerable ageing time of 195 and 215 days under ambient conditions, respectively.

Normalized photoluminescence excitation (PLE) and photoluminescence (PL) spectra of the sample films are displayed in Fig. 3.7. For each film, several PLE and PL spectra were recorded at different emission and excitation wavelengths and averaged to yield the displayed spectra. An overview of the investigated PNP films including the their ageing time, wavelength of absorption onset and their PL characteristics is given in Table 3.1. The PLE spectra of the films generally show a similar shape with some differences in the steepness of the increase of absorption towards low wavelengths and in the slope of the spectra at the band edges. A clear difference between all films can be observed, however, in the wavelength at which the absorption edge occurs in the PLE spectra, as can be seen from Table 3.1. Along with the absorption onsets, also the maxima of the PL peaks of the films are shifted similarly. The typical size of the nanoparticles manufactured by the used preparation method was reported as ca. 6 nm [90], which is comparable to the reported value of the exciton Bohr radius of 2 nm for $MAPbBr_3$ crystals [126]. Thus, an

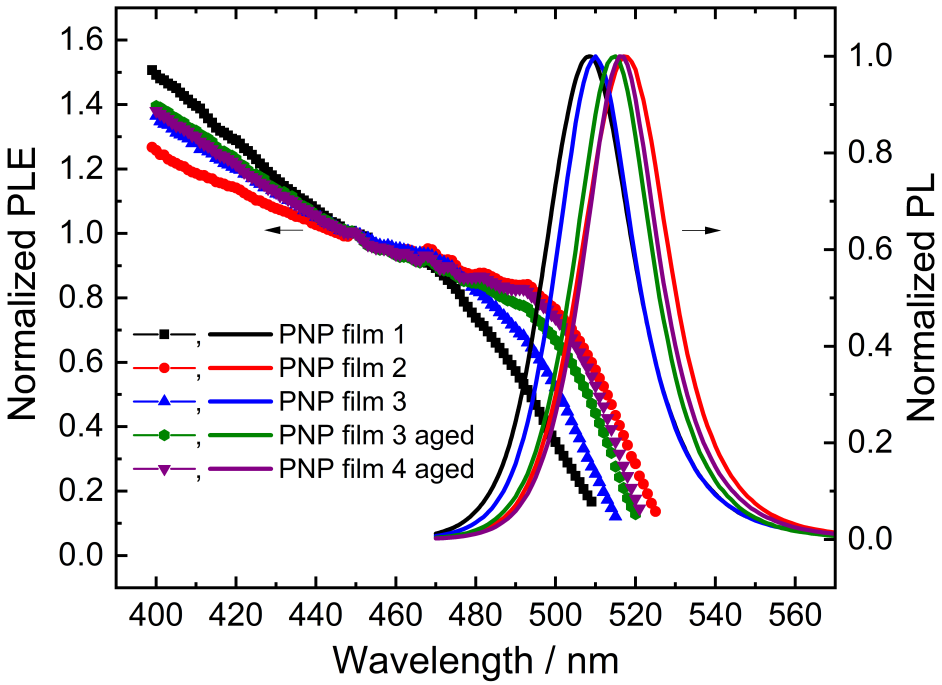

Figure 3.7. Photoluminescence excitation (PLE) and photoluminescence (PL) spectra of the investigated perovskite nanoparticle films. PLE spectra are normalized to the respective values at 450 nm, while PL spectra are normalized to their respective maxima. The plotted spectra represent averages of normalized PLE and PL spectra measured at different emission/excitation wavelengths. The wavelength scales of all recorded PLE spectra were shifted by $\lambda - 1$, as discussed in section 2.5.5.

Table 3.1. Overview of the investigated perovskite nanoparticle films including the ageing time under atmospheric conditions (time between film preparation and measurement), the absorption onset λ_{og} as determined from Tauc plot in Appendix A.2.1, the PL maximum wavelength $\lambda_{\mathrm{PL\ max}}$ and the full width at half maximum of the PL band.

Film	Ageing time / d	λ_{og} / nm	$\lambda_{\mathrm{PL\ max}}$ / nm	$\mathrm{FWHM_{PL}}$ / nm
PNP film 1	1	504	508	26
PNP film 2	1	521	517	25
PNP film 3	1	510	510	23
PNP film 3 aged	195	519	515	23
PNP film 4 aged	215	519	516	22

intermediate to strong quantum confinement effect can be expected for these nanoparticles, which leads to a particle size-dependence of the energy of excitonic absorption and photoluminescence and manifests as a blue-shift of the corresponding spectra at decreasing particle size [127, 128]. Differences in the mean diameters of the nanoparticles constituting the investigated films can thus account for the spectral shift of the PLE and PL spectra.

The PL spectra of the films show a narrow shape with low full widths at half maximum (FWHM) of 22 to 26 nm. Since the width of the emission spectra of nanoparticles is typically considerably influenced by the particle size distribution, the relatively small FWHM of the PNP film emission indicates a rather narrow size distribution of the deposited $MAPbBr_3$ nanoparticles [129]. The PL spectra of all investigated films show a slight tailing towards higher wavelengths (lower energies) which conforms to the spectral shapes previously reported for $MAPbBr_3$ nanocrystals [129, 130] and leads to an offset of the mean PL wavelength towards higher wavelengths relative to the PL maximum.

To allow the determination of the photoluminescence quantum yields η_{PL} of the PNP films according to the method described in section 2.5.5, PDS measurements of the films were carried out. For all measurements the measurement parameters stated in section 2.5.2 were used. For each film, 4 to 6 PDS spectra were measured on different positions on the film and averaged to obtain the final mean PDS spectrum. For comparison, the PL quantum yields of the investigated films were additionally measured on a Hamamatsu external quantum efficiency measurement system equipped with an integrating sphere. The integrating sphere measurements were carried out at an excitation wavelength of 405 nm.

3.2.1.1. Photoluminescence Quantum Yield of PNP Film 1

The deflection spectrum and the wavelength-corrected PLE spectrum measured for PNP film 1 are shown in Fig. 3.8 (a). Comparison of the two curves shows the strong deviation of the corrected deflection signal spectrum $S_{\mathrm{Corr}}(\lambda)$ from the absorption profile $a(\lambda)$ of the film resembled by the PLE spectrum, which indicates a high photoluminescence quantum yield of the sample as discussed in section 1.2.2.3. To determine the PLQY of the sample according to the method described in section 2.5.5, the quotient of $S_{\mathrm{Corr}}(\lambda)$ and $a(\lambda)$ is plotted versus λ and fitted by a linear function. The resulting graphs and the normalized PL spectrum of PNP film 1 measured at an excitation wavelength of 450 nm are shown in Fig. 3.8 (b). To establish a repeatable and

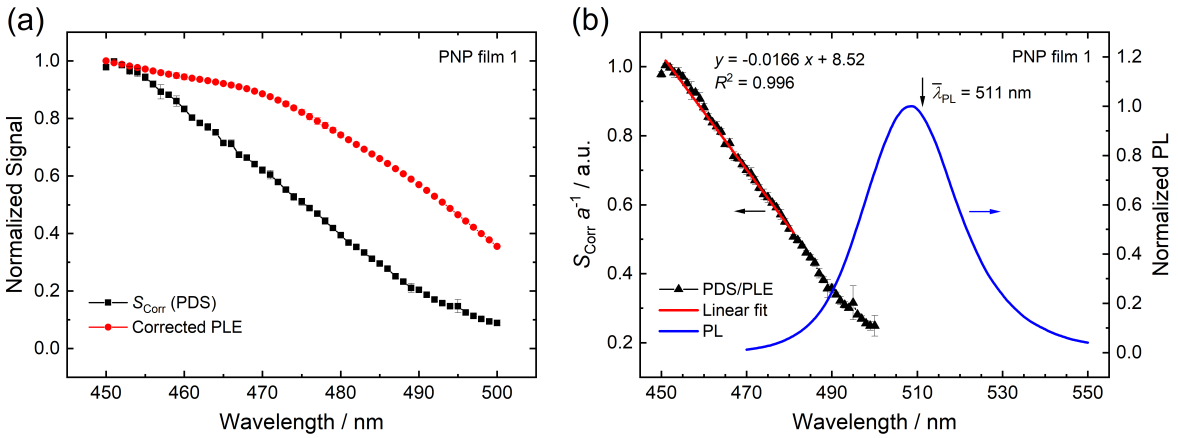

Figure 3.8. (a) Normalized corrected deflection spectrum and normalized wavelength-corrected PLE spectrum of PNP film 1. **(b)** Plot of the quotient of $S_{\mathrm{Corr}}(\lambda)$ and the PLE spectrum (which is assumed proportial to the absorptance $a(\lambda)$) versus wavelength and a linear fit of the data points with the corresponding equation and goodness of fit R^2. Additionally, the normalized PL spectrum is shown and the mean PL wavelength $\overline{\lambda}_{\mathrm{PL}}$ is indicated. From $\overline{\lambda}_{\mathrm{PL}}$ and the slope and intercept of the linear fit and their standard errors, the PLQY of the film was calculated according to eq. (3.1) as $\eta_{\mathrm{PL}} = -\frac{-0.0166 \pm 0.0002}{8.52 \pm 0.09}$ nm^{-1} $\times$ 511 nm = 0.996 $\pm$ 0.023.

unbiased fitting procedure, the wavelengths corresponding to the 1/e-values of the maximum deflection signal ($\approx 0.37 \times S_{\mathrm{Corr\ max}}$) were chosen as upper wavelength boundaries for the linear fit in analogy to ref. [36]. Thus, the linear fit for PNP film 1 was applied in the wavelength range of 450 – 481 nm. The standard deviations of the S_{Corr}/a data points were calculated from the standard deviations of the PDS and PLE spectra and were used as weighting factors for the fitting function. The linear fit for PNP film 1 shows a very good conformity to the quotient of the measured data. The slope and intercept of the linear fit and the mean PL wavelength $\overline{\lambda}_{\mathrm{PL}}$, as determined via eq (2.17) from the PL spectrum, are specified in Fig. 3.8 (b). From these values, the PLQY η_{PL} of the film can be calculated via eq. (3.1), which was deduced from equation (2.18).

$$\eta_{\mathrm{PL}} = -\frac{\mathrm{slope}}{\mathrm{intercept}}\,\overline{\lambda}_{\mathrm{PL}} \tag{3.1}$$

From eq. (3.1), a PLQY of $\eta_{\mathrm{PL}} = 99.6 \pm 2.3$ % was determined for PNP film 1. The spread of the values of ± 2.3 % was determined from the standard error of slope and intercept of the linear fitting function. From the PLQY determination on the integrating sphere measurement system, a value of $\eta_{\mathrm{PL}} = 98.2 \pm 6.9$ % was measured for PNP film 1 which closely matches the value calculated from PDS measurements.

To assess the differences between the two values with respect to the measured deflection spectrum, the theoretical shape of the S_{Corr} spectrum was calculated via eq. (2.18) from the measured PLE spectrum for $\eta_{\mathrm{PL}} = 99.6$ % and $\eta_{\mathrm{PL}} = 98.2$ %. The calculated curves and the experimentally measured PLE and deflection spectra are shown in Fig. 3.9 (a). For comparison, also the PDS spectrum calculated for a PLQY of 90 % is shown. The spectrum calculated for $\eta_{\mathrm{PL}} = 90.0$ % fits the measured PDS spectrum in a small range at low wavelengths but deviates strongly from the experimental data above wavelengths of 458 nm. In contrast, the spectra calculated for 99.6 % and 98.2 % PLQY fit the experimental S_{Corr} spectrum reasonably well.

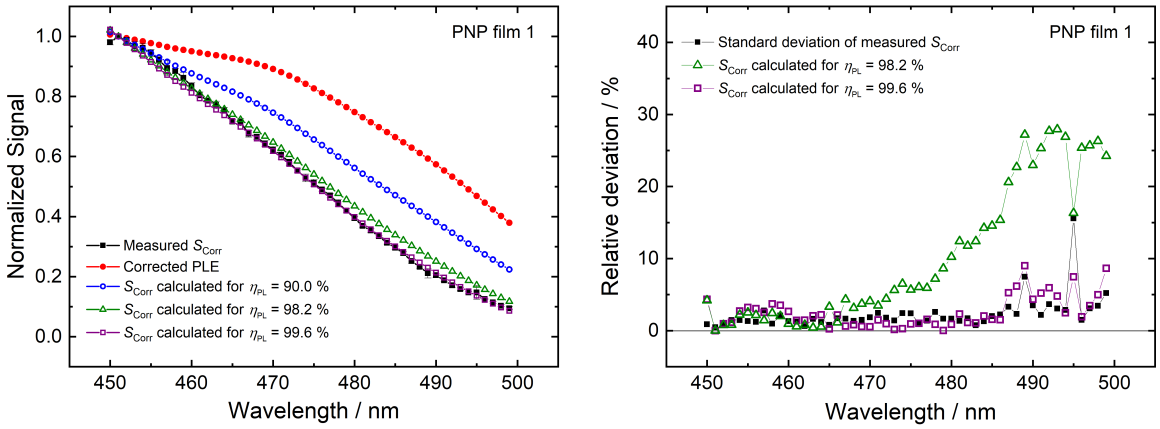

Figure 3.9. **(a)** Normalized plots of the experimentally measured corrected deflection spectrum, the wavelength-corrected PLE spectrum and $S_{\mathrm{Corr\ calc}}$ spectra theoretically calculated from PLE for PLQYs of $\eta_{\mathrm{PL}} = 99.6\,\%$, 98.2 % and 90.0 % via eq. (2.18) for PNP film 1. **(b)** Relative derivation of the deflection spectra calculated for $\eta_{\mathrm{PL}} = 99.6\,\%$ and 98.2 % from the experimental deflection spectrum calculated according to $|S_{\mathrm{Corr\ calc}} - S_{\mathrm{Corr\ exp}}|\ S^{-1}_{\mathrm{Corr\ exp}}$.

Fig. 3.9 (b) shows the relative deviation of the calculated PDS spectra from the measured corrected deflection signal, as well as the relative deviation determined from the standard deviation of the measured PDS spectra. Comparison of the relative deviations reveals that despite the small difference of the two PLQY values, the spectrum calculated for $\eta_{\mathrm{PL}} = 99.6\,\%$ matches the experimentally measured PDS spectrum with noticeably higher accuracy over the majority of the spectrum, as shown by the considerably lower relative deviation which is on the order of the standard deviation of the measured S_{Corr} values. This demonstrates the capability of the method to resolve small differences in PLQY. It must be considered however, that the resolution and accuracy of the method are dependent on the magnitude of the PLQY since the difference between absorptance (or PLE) and PDS spectra is less pronounced for lower values of η_{PL} and thus more prone to distortion by measurement variance.

3.2.1.2. Photoluminescence Quantum Yields of PNP Films 2, 3 and 4

The photoluminescence quantum yields of PNP films 2 to 4 were determined analoguous to film 1. The corresponding graphs are displayed in Fig. 3.10. The mean PL wavelengths, the PLQY values calculated from the linear fits of the $S_{\mathrm{Corr}}\,a^{\text{-}1}$ curves and the PLQY determined from integrating sphere measurements are summarized in Table 3.2. As can be seen in Fig. 3.10 (b), the linear fitting function for PNP film 2 shows very high conformity to the data. The calculated PLQY of $96.7 \pm 1.9\,\%$ conforms excellently to the mean PLQY of 96.4 % determined on the integrating sphere setup. In the case of film 3, measured one day after its preparation, the plot of PDS/PLE versus wavelength (Fig. 3.10 (d)) displays a slight curvature and consequently shows a slightly higher deviation of the experimental data from the linear fitting function. This could be a result of the higher standard deviation of the measured deflection signal due to the higher differences in the shape of the single PDS spectra measured on different positions on the film, which leads to large error margins in the $S_{\mathrm{Corr}}\,a^{\text{-}1}$ curve. Consequently, the calculated PLQY of 91.5 % has a larger spread of $\pm 4.4\,\%$ as compared to films 1 and 2. The mean value however, conforms very well to the mean PLQY of 90.5 % measured on the integrating sphere setup.

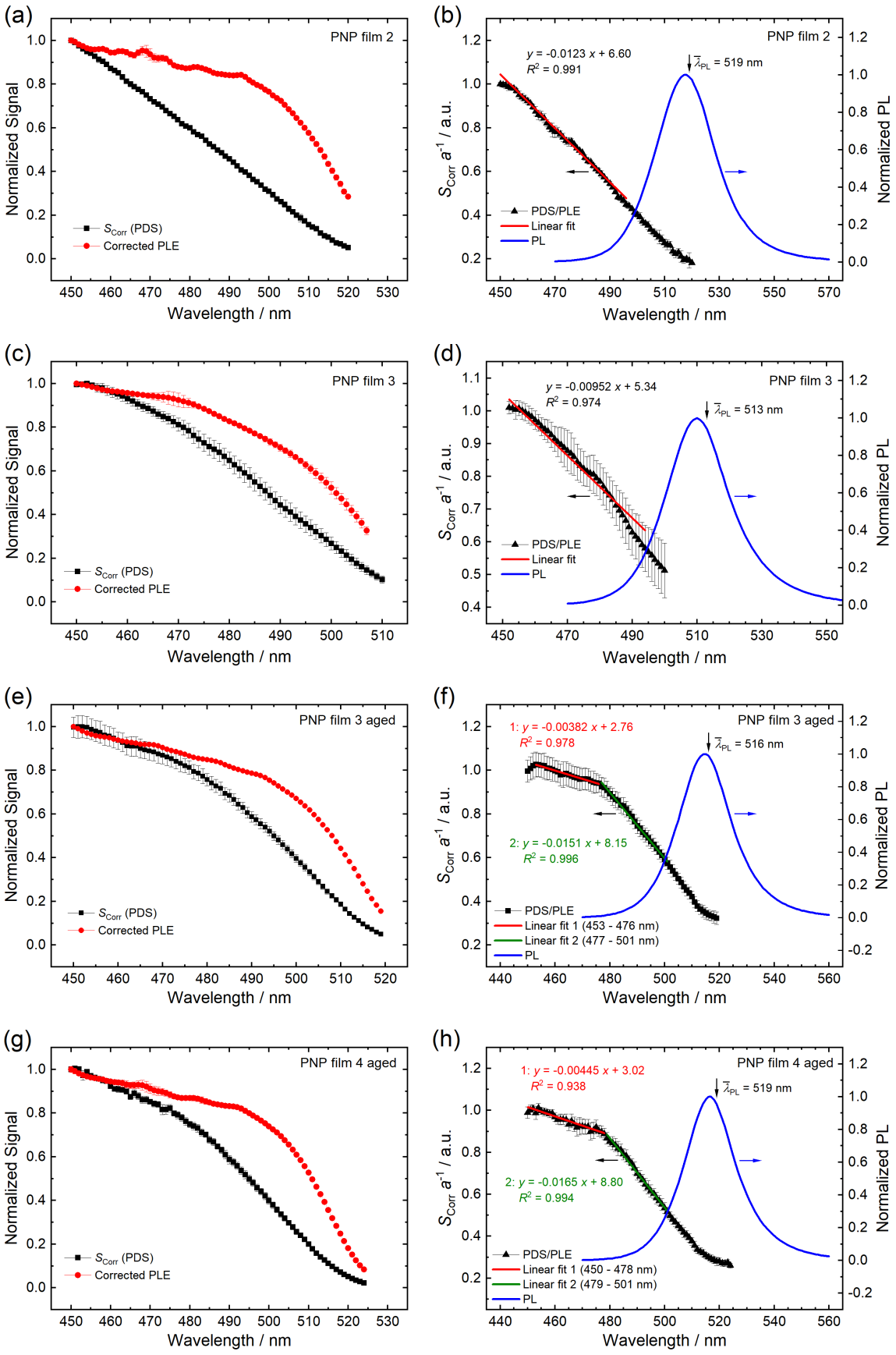

Figure 3.10. Comparison of normalized corrected deflection spectra $S_{\mathrm{Corr}}(\lambda)$ and wavelength-corrected PLE spectra ($\propto a(\lambda)$), as well as quotient of $S_{\mathrm{Corr}}(\lambda)$ and $a(\lambda)$ with the corresponding linear fits and PL spectra of PNP film 2 **(a)**, **(b)**, PNP film 3 as-prepared **(c)**, **(d)** and aged **(e)**, **(f)** and PNP film 4 **(g)**, **(h)**.

Table 3.2. Mean photoluminescence wavelength $\overline{\lambda}_{\mathrm{PL}}$ and comparison of photoluminescence quantum yields η_{PL} determined for the investigated PNP films from PDS measurements and on an integrating sphere measurement setup. The spread of the PLQY values from the integrating sphere measurements were calculated from the typical relative measurement uncertainty of the method and instrument of ± 7 % as reported by Würth *et al.* [131].

Film	$\overline{\lambda}_{\mathrm{PL}}$ / **nm**	η_{PL} / **%**	
		PDS	**Integrating sphere**
PNP film 1	511	99.6 ± 2.3	98.2 ± 6.9
PNP film 2	519	96.7 ± 1.9	96.4 ± 6.7
PNP film 3	513	91.5 ± 4.4	90.5 ± 6.3
PNP film 3 aged	516	71.4 ± 3.6 *	73.0 ± 5.1
PNP film 4 aged	519	76.5 ± 6.0 *	68.8 ± 4.8

*determined from the linear fit in the low wavelength region of the spectra

The $S_{\mathrm{Corr}}\, a^{-1}$ curves determined for the aged PNP films 3 and 4 both show a similar shape with a clearly visible kink in the curves which separate the data points into two approximately linear regimes with different slopes and intercepts as can be seen from the two linear fitting functions applied in each diagram in Fig. 3.10 (f) and (h), respectively. The PL quantum yields determined from the linear fits in the lower wavelength regions are in good agreement with the η_{PL} values measured on the integrating sphere measurement setup (see Table 3.2). In the higher wavelength region the curves show a much steeper decrease with the wavelength, which suggests an increase of the PLQY of the aged films near their absorption edges. It must be considered however that the photoluminescence excitation spectrum used for calculation of η_{PL} according to eq. (2.18) is related to the absorptance of the sample film by the photoluminescene quantum yield. Thus, a direct proportionality of the two quantities in a certain wavelength range exists only at constant PLQY within this range. If an excitation wavelength-dependence of the PLQY exists, a correct determination of the PLQY from PLE with the method described in section 2.5.5 requires modifications to the underlying equations. The occurence of this phenomenon exclusively in the aged PNP films suggests that it results from ageing of the nanoparticles under ambient conditions.

Contrary to the widely valid rule of Vavilov [26, 121], an excitation wavelength-dependence of the PLQY has been reported for colloidal dispersions of different semiconductor nanostructures including nanocrystals of $MAPbX_3$ (X = Br, I) [25], $CsPbX_3$ (X = Br, I) [121], CdSe [121, 132–134] and Si [135], as well as CdTe nanowires [133] and CdSe/CdS core/shell quantum dots [136]. In their studies on dispersions of methylammonium and cesium lead halide perovskite nanocrystals, Righetto *et al.* [25] and Li *et al.* [121] found that the PLQY of the nanocrystals was maximal at excitation energies closest to their bandgap energy and decreased with increasing excitation energy (lower excitation light wavelength). This observation was attributed to the increased trapping of hot carriers in shallow traps at higher excess energies of the excited carriers [25, 121]. In view of these findings, the increase of PLQY towards the absorption edge as indicated by the results found for the aged PNP films 3 and 4 could be due to an increasing occurence of shallow traps upon nanoparticle ageing. This could potentially induce a significant excitation wavelength-dependence

of PL efficiency and lead to a decreased PLQY especially at lower excitation wavelengths as is found by comparison of PNP film 3 as-prepared and aged. The as-prepared PNP films 1, 2 and 3, showed no or only a very small change of PLQY between the excitation wavelength of 405 nm used in the integrating sphere PLQY measurements and the wavelength regions near their absorption onsets which were investigated for the PLQY calculation from PDS and PLE measurements. However, a precise determination and detailed elucidation of this apparent change in PLQY requires further investigation which is outside the scope of this work.

3.2.2. Film of a Perylene Diimide Dye in a PS Matrix

To verify the applicability of the PL quantum yield determination method via PDS to other fluorescent samples, a thin film of a PS matrix incorporating *N*,*N*'-bis(2,6-diisopropylphenyl)-3,4,9,10-perylene diimide (PDI) was investigated by $R\,\&\,T$ measurements, PL spectroscopy and PDS. The film was prepared with a mass ratio of PDI to PS of 1:10. Dispersion of the fluorophore in a solid matrix was carried out to increase the photoluminescence quantum yield of the molecules by decreasing the concentration of the dye in the solid film and thus reduce π–π stacking interactions that can suppress its photoluminescence [137, 138].

The corrected deflection spectrum, the absorptance spectrum determined from $R\&T$ measurements and the wavelength-corrected PLE spectrum measured for the film are shown in Fig. 3.11 (a). All spectra were obtained by averaging multiple measurements and were normalized to their respective maxima. Comparison of the normalized absorptance and PLE spectra of the film show a very high conformity of the two curves, which suggests that there is no change of PLQY with wavelength over the investigated spectral region [121]. The S_{Corr} spectrum displays a clearly visible deviation from the absorptance and PLE spectra indicating the influence of photoluminescence. Due to the normalization of the spectra to their maxima at 526 – 527 nm, the absorption bands at 490 nm and 459 nm appear more pronounced and slightly blue-shifted in the deflection spectra since the influence of the PL leads to a decrease of the relative intensity of the peak closer to the mean PL wavelength with respect to the peaks at lower wavelengths.

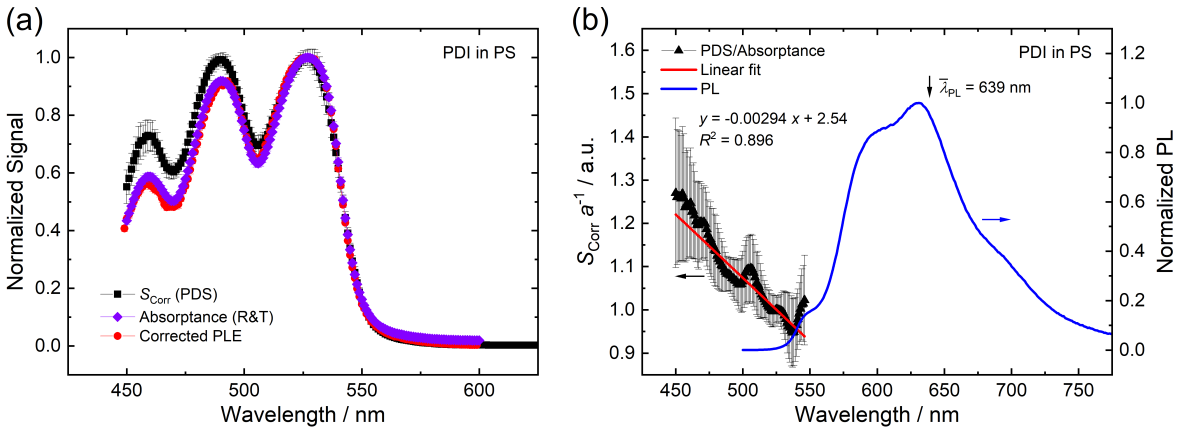

Figure 3.11. (a) Corrected deflection spectrum, absorptance spectrum and wavelength-corrected PLE spectrum of a film of PDI dispersed in a PS matrix at a mass ratio of 1:10. Each spectrum is normalized to its maximum. **(b)** Quotient of normalized corrected deflection spectrum and normalized absorptance spectrum together with the normalized PL spectrum of the film of PDI in PS.

For the calculation of the PLQY the quotient of S_{Corr} and normalized absorptance (from R and T measurements) versus wavelength was determined and is displayed in Fig. 3.11 (b) together with the PL spectrum of the film. The linear function used to fit the data points shows only a moderate goodness of fit due to a strong fluctuation of the data around the expected linear degression. Analogous to the PNP films, the wavelength corresponding to the $1/e$-values of the maximum deflection signal was used as upper limit for the fit and the standard deviations of the data were used as weighting factors. From the mean PL wavelength and the equation and standard errors of the fitting function, a PLQY of $\eta_{\mathrm{PL}} = 74.0 \pm 4.0\,\%$ was determined via eq. (3.1). This value conforms reasonably well to the PLQY of $68.3 \pm 4.8\,\%$ determined for the film in the integrating sphere measurement system at an excitation wavelength of 490 nm. The high uncertainty of the $S_{\mathrm{Corr}}\,a^{-1}$ data, as shown by the large error bars in Fig. 3.11 (b), results from a comparatively large variance of the shapes of the individual deflection spectra measured at different spots on the film. This indicates an inhomogeneous distribution of the fluorescent PDI molecules in the PS matrix. These inhomogeneities can potentially lead to differences in the local PLQY of the measured spots and can thus result in slightly different shapes of the measured normalized PDS spectra.

3.3. Urbach Energy of a Mixed-Halide Lead Perovskite Film

A film of $MAPbI_{3-x}Cl_x$ with a thickness of $d = 600$ nm on fused quartz was investigated by PDS and $R\,\&\,T$ measurements to determine its absorption coefficient spectrum and allow the calculation of its Urbach energy.

The corrected deflection signal obtained for the film from PDS measurements was scaled via signal saturation to match the value of $1 - R$ at a wavelength of 720 nm. The $A_{\mathrm{PDS}}(\lambda)$ spectrum, $A_{\mathrm{R/T}}(\lambda)$ spectrum as determined from $R\,\&\,T$ measurements and the reflectance spectrum $R(\lambda)$ of the film are displayed in Fig. 3.12 (a). The absorption coefficient of the film was calculated from the two absorptance spectra and the $R(\lambda)$ spectrum via eq. (2.15) for the film thickness of 600 nm. The resulting $\alpha(\lambda)$ spectra are shown in Fig. 3.12 (b). The spectra show a very large difference between $A_{\mathrm{PDS}}(\lambda)$ and $A_{\mathrm{R/T}}(\lambda)$. Remarkably, the $R\,\&\,T$ absorptance spectrum shows a considerably large value of the absorptance far above its typical sensitivity limit (see section 3.1.3) even at wavelengths above the bandgap while in the case of PDS a sharp decline of the absorptance towards the setup noise limit can be observed at the band edge (see section 3.1.3). This suggests that the measurement at the spectrophotometer was significantly distorted by a disturbance such as scattering. The results also show that the perovskite film shows no optical transitions with significant strength below its band tail, which suggests a very low density of trap states and defects.

From the absorption coefficient spectrum, an optical bandgap energy of the film of $E_{\mathrm{og}} = 1.60$ eV was determined (see Appendix A.2.1). Additionally, the absorption coefficient spectrum determined from PDS was used for the calculation of the Urbach energy of the film. As described in section 2.5.6, the natural logarithm of α was plotted versus the photon energy E, which was calculated from the wavelength scale with the relation $E = h\,c\,\lambda^{-1}$. The Urbach energy was determined by fitting the resulting data points at energies below the bandgap energy with a linear function. From the reciprocal value of its slope an Urbach energy of $E_{\mathrm{U}} = 15$ meV was determined for the film.

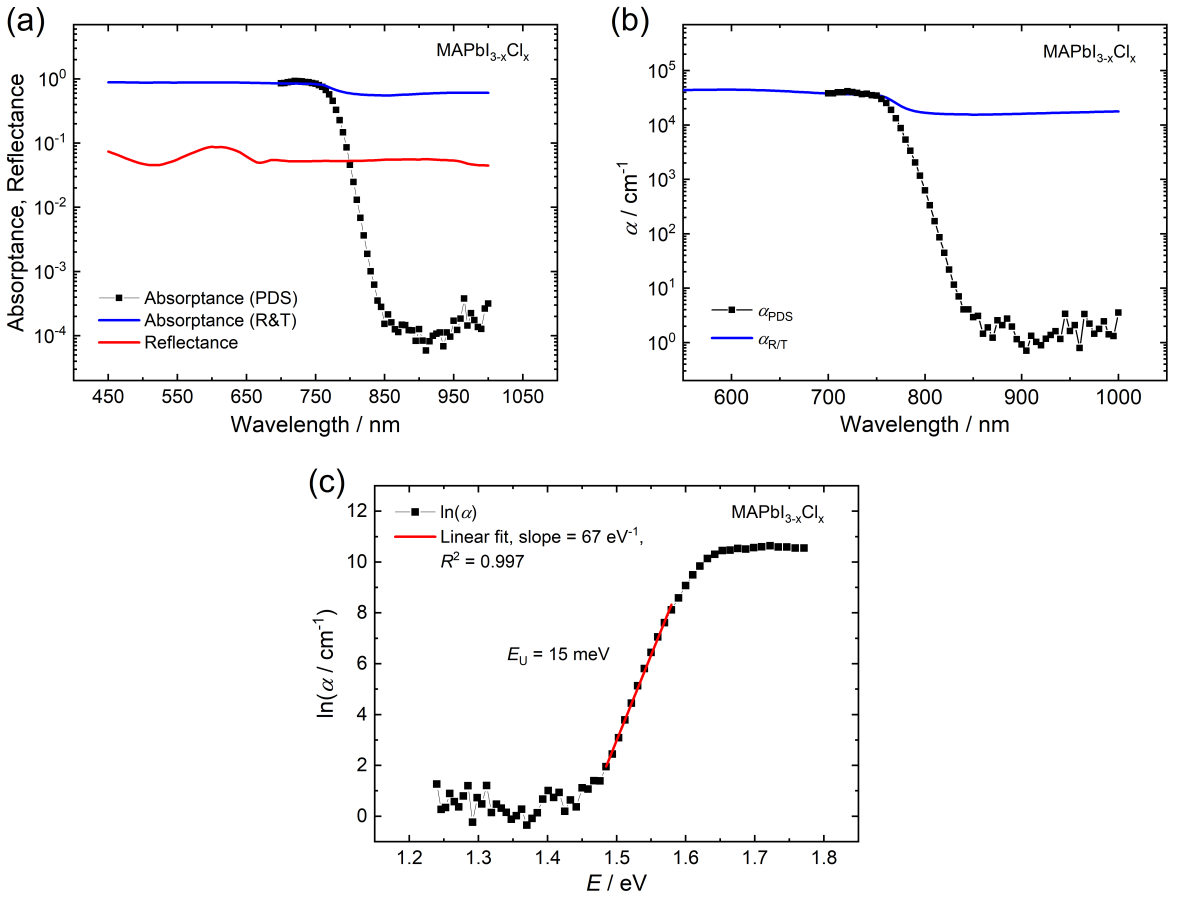

Figure 3.12. **(a)** Absorptance spectra $A_{\mathrm{PDS}}(\lambda)$ and $A_{\mathrm{R/T}}(\lambda)$, as well as reflectance spectrum $R(\lambda)$ determined for the film $MAPbI_{3-x}Cl_x$ on fused quartz. **(b)** Absorption coefficient spectra of the $MAPbI_{3-x}Cl_x$ film ($d = 600$ nm) determined from $A_{\mathrm{PDS}}(\lambda)$ and $A_{\mathrm{R/T}}(\lambda)$, respectively, via eq. (2.15). **(c)** Plot of $\ln(\alpha)$ vs. the photon energy E and the corresponding linear fit of the data points in the band tail. According to eq. (2.22), an Urbach energy of $E_{\mathrm{U}} = 15$ meV was calculated from the inverse value of the slope of 67 eV^{-1} of the linear fit function.

This is identical to the value reported for a similar $MAPbI_{3-x}Cl_x$ mixed-halide lead perovskite by De Wolf *et al.* [58]. The low value of E_{U} is close to the Urbach energies reported for typical high purity inorganic semiconductor materials such as monocrystalline GaAs and monocrystalline Si and suggests a very high quality of the film and material, as it indicates a very low degree of disorder [8, 58].

3.4. Investigation of Organic Photovoltaic Materials

Pristine films and films of donor-acceptor blends of the donor materials PBDB-T-2F and PTB7-Th and the acceptor materials IT-4F and $PC_{71}BM$, used in high-efficiency bulk-heterojunction (BHJ) organic solar cells [139–141], were investigated. PDS and $R\,\&\,T$ measurements were carried out to reveal absorption features in the sub-bandgap spectral region of the materials which can arise from D-A interaction and can provide insight into the expected properties of the corresponding organic solar cells.

3.4.1. Determination of the Absorption Coefficient Spectra

For an universal comparability of the investigated blends and pristine materials, independent of the thicknesses of the individual films, the absorption coefficient spectra $\alpha(\lambda)$ of the investigated films were determined from the measured deflection spectra. With the exception of the blade coated film of PTB7-Th, all PDS measurements were carried out with the measurement parameters stated in section 2.5.2. In preliminary PDS measurements at 100 % pump laser power, photodegradation of PTB7-Th resulting in decoloration of the film at the measurement spots was found. To avoid this degradation and a possible distortion of the measured spectra as a result thereof, a pump light power variation was used in the measurements of the blade coated PTB7-Th film: In the region of 800 – 735 nm the pump laser power was decreased from 100 % to 35 % in steps of 5 % per 5 nm wavelength step; above 800 nm and below 735 nm constant pump laser powers of 100 % and 35 %, respectively, were used.

Since the assembled PDS setup shows a limitation of the measurement sensitivity down to absorptance values of $A \approx 10^{-4}$, films with comparatively high thicknesses fabricated by blade coating or drop casting were used to allow precise measurement of sub-bandgap absorption coefficient. Thick and non-uniform films however, often lead to deflection signal saturation in spectral regions of higher α. Furthermore, their transmittance spectra can often not be accurately measured on spectrophotometers due to measurement distortion by the thickness inhomogeneity and the typically limited sensitivities of the instruments at very low transmittances. Thus, complementary measurements of thinner films deposited by spin coating were carried out for several investigated materials and combined with the higher film thickness measurements to obtain full spectra of the absorption coefficients. All films were deposited on fused quartz to avoid a measurement limitation by substrate absorption.

The used procedure for determining and combining the spectra measured for films prepared by different film deposition methods, is discussed in the following by the example of a dropcast ($d \approx 6000$ nm) and spin coated film ($d = 35$ nm) of a 1:1 (w/w) blend of PBDB-T-2F:IT-4F. Fig. 3.13 (a) and (b) show the corrected deflection spectra $S_{\mathrm{Corr}}(\lambda)$ obtained for the dropcast and spin coated films from averaging the corrected deflection spectra measured on multiple different spots of the films, respectively. Additionally the reflectance spectrum of the dropcast film and the reflectance and absorptance ($A_{\mathrm{R/T}}$) spectra of the spin coated film are displayed. The different shapes and signal magnitudes of the corrected deflection spectra clearly indicate the variations in the PDS measurements due to the substantial difference of the thicknesses of the two films. While the

$S_{\mathrm{Corr}}(\lambda)$ spectrum measured for the spin coated film conforms to the shape of the absorptance spectrum determined from $R\,\&\,T$ measurements on the spectrophotometer which clearly shows the occurrence of peaks at ca. 580 nm, 625 nm and 710 nm, the dropcast film shows an approximately constant deflection signal over the wavelength range of 690 – 800 nm. This is a clear indication for a signal saturation during the PDS measurement which masks the actual absorption profile of the film in this wavelength region. In the high wavelength region ($\lambda \geq 850$ nm) strong fluctuations of the data can be observed for the spin coated film, indicating a heavy influence of noise which limits the measurement while the spectrum measured for the dropcast film shows no fluctuations and much higher S_{Corr} values above the noise level of the setup. To determine the absorptance A_{PDS} from the corrected deflection signal, the $S_{\mathrm{Corr}}(\lambda)$ spectrum of the dropcast film was scaled via signal saturation according to eq. (2.9) to match the value of $1-R$ at a wavelength of 745 nm. The corrected deflection spectrum of the spin coated film was scaled to match the $R\,\&\,T$ absorptance spectrum at 630 nm according to eq. (2.10).

The absorptance spectra obtained for the films from the scaling procedure are displayed in Fig. 3.13 (c). While the $A_{\mathrm{PDS}}(\lambda)$ of the dropcast film shows generally much larger values, the

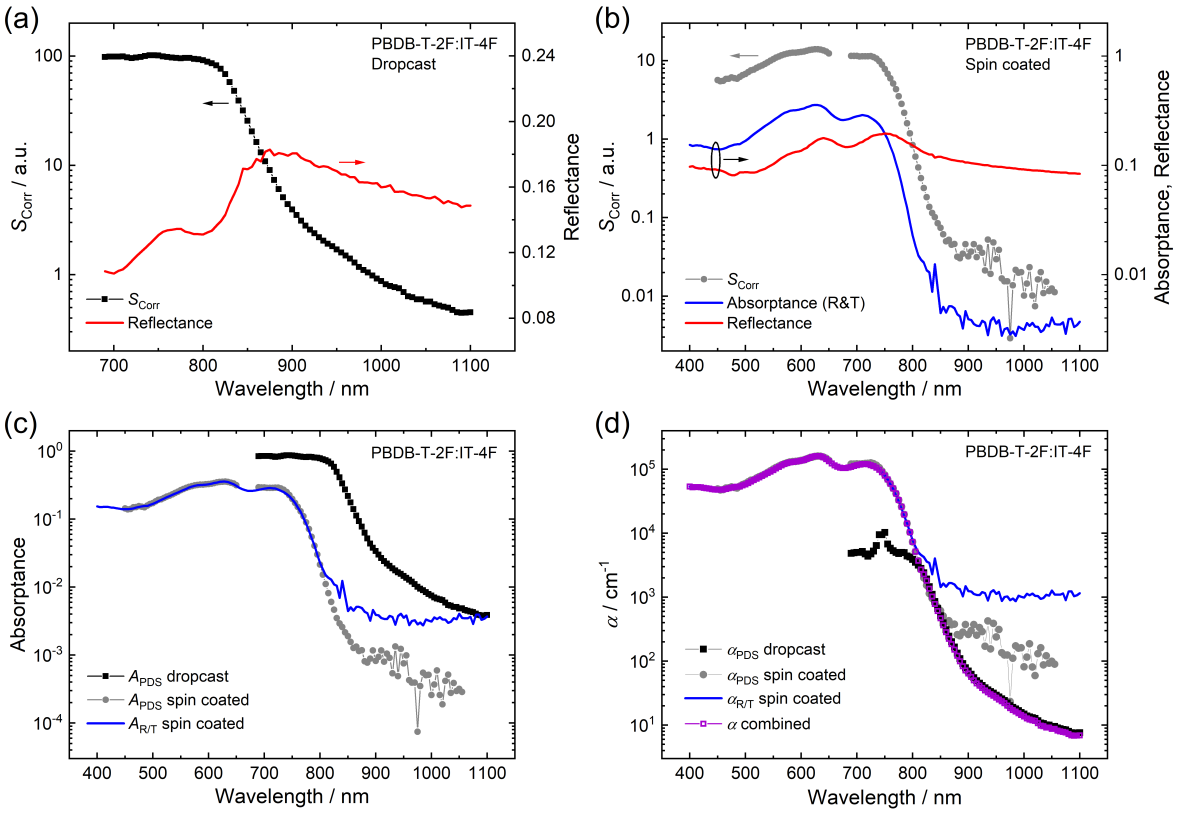

Figure 3.13. (a) Corrected deflection spectrum $S_{\mathrm{Corr}}(\lambda)$ and reflectance spectrum $R(\lambda)$ of the drop casted PBDB-T-2F:IT-4F blend film. **(b)** $S_{\mathrm{Corr}}(\lambda)$, $R(\lambda)$ and absorptance spectrum $A_{\mathrm{R/T}}(\lambda)$, determined from reflectance and transmittance measurements, of the spin coated PBDB-T-2F:IT-4F blend film. **(c)** Absorptance spectra $A_{\mathrm{PDS}}(\lambda)$ of the spin coated film, obtained by scaling to $A_{\mathrm{R/T}}$ at 630 nm, and $A_{\mathrm{PDS}}(\lambda)$ of the dropcast film obtained by scaling to the value of $1-R$ at 745 nm. **(d)** Absorption coefficient spectra $\alpha(\lambda)$ determined via eq. (2.15) from $A_{\mathrm{PDS}}(\lambda)$ and $A_{\mathrm{R/T}}(\lambda)$ for the dropcast ($d \approx 6000$ nm) and spin coated films ($d \approx 35$ nm) of PBDB-T-2F:IT-4F. Due to the excellent agreement of the spectra, they were merged into a combined $\alpha(\lambda)$ spectrum (purple open squares).

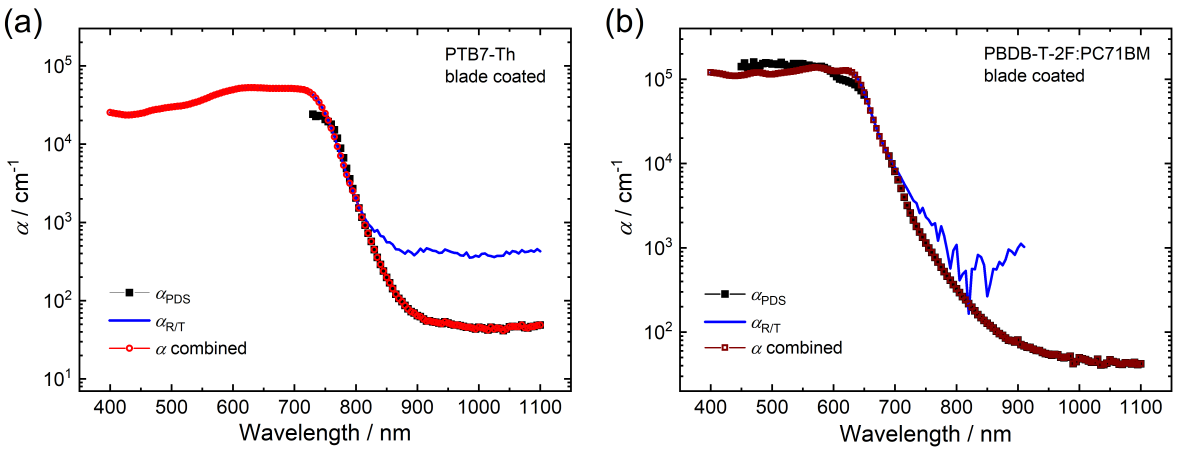

Figure 3.14. Absorption coefficient spectra of the blade coated films of **(a)** PTB7-Th and **(b)** PBDB-T-2F:$PC_{71}BM$. Combined $\alpha(\lambda)$ spectra of the films were obtained by merging $\alpha_{\mathrm{PDS}}(\lambda)$, determined from PDS measurements and $\alpha_{\mathrm{R/T}}(\lambda)$, determined from R & T measurements.

$A_{\mathrm{PDS}}(\lambda)$ spectrum of the spin coated PBDB-T-2F:IT-4F film shows excellent confomity with the absorptance $A_{\mathrm{R/T}}(\lambda)$ spectrum measured via the spectrophotometer at 450 –800 nm and displays absorptance values of ca. 1/5 of those of $A_{\mathrm{R/T}}(\lambda)$ above 800 nm before reaching the limiting noise level. From the $A_{\mathrm{PDS}}(\lambda)$ or $A_{\mathrm{R/T}}(\lambda)$ spectra, the reflectance spectra and film thicknesses, the absorption coefficients of the films were determined via equation (2.15) and are plotted in Figure 3.13 (d). The absorption coefficient determined from the dropcast film conforms very well to the values determined from the spin coated film in the overlapping intermediate region from 810 nm to 850 nm. This demonstrates that both methods yield comparable results and indicates their validity. For films deposited via drop casting, the typically observed large film thickness inhomogeneities must be considered, however, since they can significantly affect the accuracy of the calculated absorption coefficient. These inhomogeneities can account for the observed small differences between α determined for drop casted and spin coated films. Due to its homogeneous thickness, the absorption coefficient spectrum of the spin coated film is expected to be more reliable. Consequently, the $\alpha(\lambda)$ spectrum of the dropcast film was scaled to match the spectrum of the spin coated film at 815 nm yielding the combined $\alpha(\lambda)$ spectrum for the PBDB-T-2F:IT-4F blend shown in Fig. 3.13 (d).

This procedure was carried out analogously for the other investigated OPV films with the exceptions of pristine PTB7-Th and the PBDB-T-2F:$PC_{71}BM$ blend for which only blade coated films were measured. For these films the $\alpha(\lambda)$ spectra were determined by combination of the absorption coefficient determined from $A_{\mathrm{PDS}}(\lambda)$ and $A_{\mathrm{R/T}}(\lambda)$ as shown in Fig. 3.14. It must be noted that for the donor-acceptor (D-A) blends of the investigated OPV materials an influence of the film preparation method on the morphology of the blends is probable [142–144]. Differences in the morphology of the blend films can, among other effects, lead to changes of crystallinity of the domains and changes of the D-A interfacial area and geometry and can thus have a significant impact on the electronic interaction of the D and A molecules and consequently change the intensities and spectral positions of optical transitions arising from those interactions [76, 79, 145].

3.4.2. Absorption Coefficient Spectra of D-A Blends and Pristine Components

The absorption coefficient spectra determined for films of the neat materials PBDB-T-2F, PTB7-Th, IT-4F and $PC_{71}BM$ and their 1:1 (w/w) blends (see Table 2.1) were determined by the procedure described in section 3.4.1 and are shown in Fig. 3.15.

Fig. 3.15 (a) displays the absorption coefficient spectra determined for the three investigated donor-acceptor blends. Figures 3.15 (b) to (d) show the $\alpha(\lambda)$ spectra of the blend films together with the spectra of the corresponding pristine donor and acceptor materials. In the low wavelength regions before the absorption edges of the D-A blends, all films show distinct absorption profiles resembling roughly averages of the $\alpha(\lambda)$ spectra of the pristine constituents of the blends, with absorption coefficients on the order of 0.3×10^5 –$1.6 \times 10^5\,cm^{-1}$. Remarkable differences of the blends can be observed at wavelengths below the band edges. While the PBDB-T-2F:IT-4F blend (Fig. 3.15 (c)) shows no absorption features different from a simple combination of the spectra of PBDB-T-2F and IT-4F, the other two blends show the occurrence of an additional absorption band at wavelengths of 715 – 860 nm for PBDB-T-2F:$PC_{71}BM$ (Fig. 3.15 (d)) and 850 – 1000 nm for PTB7-Th:IT-4F (Fig. 3.15 (d)) with absorption coefficients higher than in both pristine materials of the blends in the respective spectral regions. These absorption bands can be assigned to the

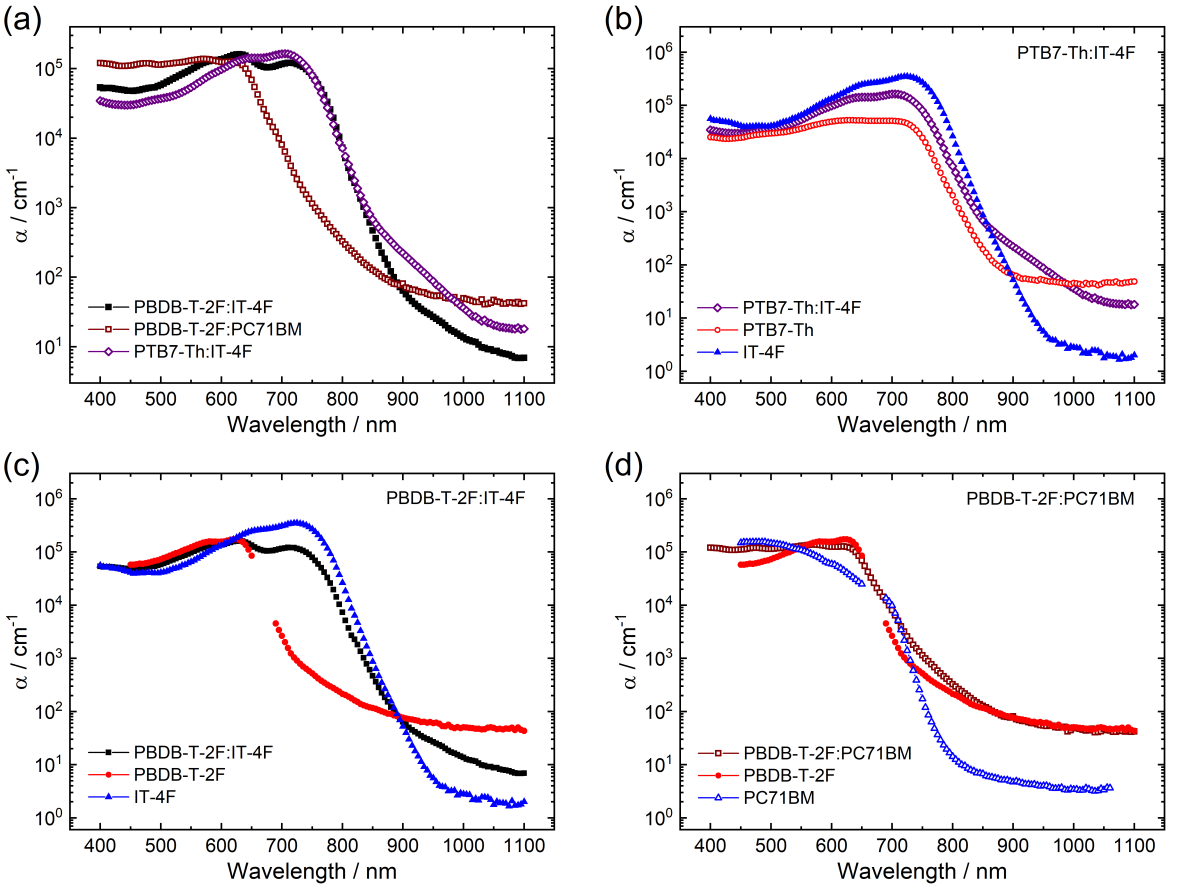

Figure 3.15. (a) Absorption coefficient spectra $\alpha(\lambda)$ determined for the blends of PBDB-T-2F:IT-4F, PBDB-T-2F:$PC_{71}BM$ and PTB7-Th:IT-4F. Comparison of the $\alpha(\lambda)$ spectra of the blends with the corresponding absorption coefficient spectra of the pristine donor and acceptor materials for **(b)** PTB7-Th:IT-4F, **(c)** PBDB-T-2F:IT-4F and **(d)** PBDB-T-2F:$PC_{71}BM$.

photoexcitation of the CT state (CT absorption), formed due to the electronic interactions of donor and acceptor at the D-A interface [19, 75, 76, 78, 79, 146]. The typically low oscillator strength of the CT absorption bands as compared to the excitonic absorptions at energies above the bandgap energy of the blends [66], results in low absorption coefficients of the CT absorption shoulder in the $\alpha(\lambda)$ spectra of ca. 2000 cm^{-1} for PBDB-T-2F:$PC_{71}BM$ and ca. 300 cm^{-1} for PTB7-Th:IT-4F, thus can typically only be precisely measured by sensitive techniques like PDS. The sub-bandgap region of the spectra also reveals that the donor materials PBDB-T-2F and PTB7-Th show a broad sub-bandgap absorption with an approximately constant absorption coefficient of ca. 50 cm^{-1} in the region of 900 – 1100 nm, as compared to the negligible sub-bandgap absorption of the acceptor materials IT-4F and $PC_{71}BM$ of ca. 2 – 5 cm^{-1} in the high wavelength region. Sub-bandgap absorption of a similar order as the values measured for PBDB-T-2F and PTB7-Th has been reported for other conjugated polymer donor materials [18, 19, 64, 81] and was attributed to absorption from trap states [18, 64] or polaron species present due to residual doping of the material [19, 147]. These light absorbing sub-bandgap states could also potentially obscure weak CT absorption upon low donor-acceptor interfacial area or weak ground-state electronic interaction between donor and acceptor.

3.4.3. Comparison with Organic Solar Cell Devices

In order to investigate the relation of the absorption coefficient spectra measured for the OPV blends to the performance and properties of corresponding OPV devices, the spectra determined from PDS measurements were compared to data from bulk-heterojunction organic solar cells (OSCs) fabricated and measured by Christoph Putz (Johannes Kepler University, Linz) [148]. An inverted architecture with the layer composition glass substrate/ITO/ZnO/active layer/MoO_3/Ag was used for the devices. The investigated 1:1 (w/w) blends of PBDB-T-2F:IT-4F and PTB7-Th:IT-4F were used as active layers deposited via spin coating [148]. The results reported for the device using a PBDB-T-2F:$PC_{71}BM$ blend as active layer were not used for comparison due to the different donor:acceptor mass ratio of 1:1.5 [148].

To investigate the relation of the $\alpha(\lambda)$ spectra of the blends with the wavelength-dependent efficiency of charge generation from incident light on the corresponding OSCs, the absorption coefficient spectra are compared to the external quantum efficiency (EQE) spectra (see section 1.2.3.2) of the devices. For the comparison it must be considered that the EQE spectrum is proportional to the absorptance spectrum of the active layer of the device [80]. As was discussed in section 2.5.3.2 and shown in Fig. 2.8, a direct proportionality of absorptance and absorption coefficient can be assumed with reasonable accuracy only for regions of weak absorption ($\alpha d \ll 1$). Thus, an accurate direct comparison of the shapes of the EQE(λ) and $\alpha(\lambda)$ spectra can be made only in the low absorbing band edge and sub-bandgap regions. The absorption coefficient spectra of the blends and EQE spectra of the corresponding devices from ref. [148] are displayed in Figure 3.16. To allow better comparability of the spectra in the sub-bandgap region, the $\alpha(\lambda)$ values were normalized to match the EQE(λ) spectra at the band edge.

For the blend of PBDB-T-2F:IT-4F, the EQE spectrum in Fig. 3.16 (a) confirms the findings from the absorption coefficient spectra as it also shows no clearly visible shoulder of the spectrum

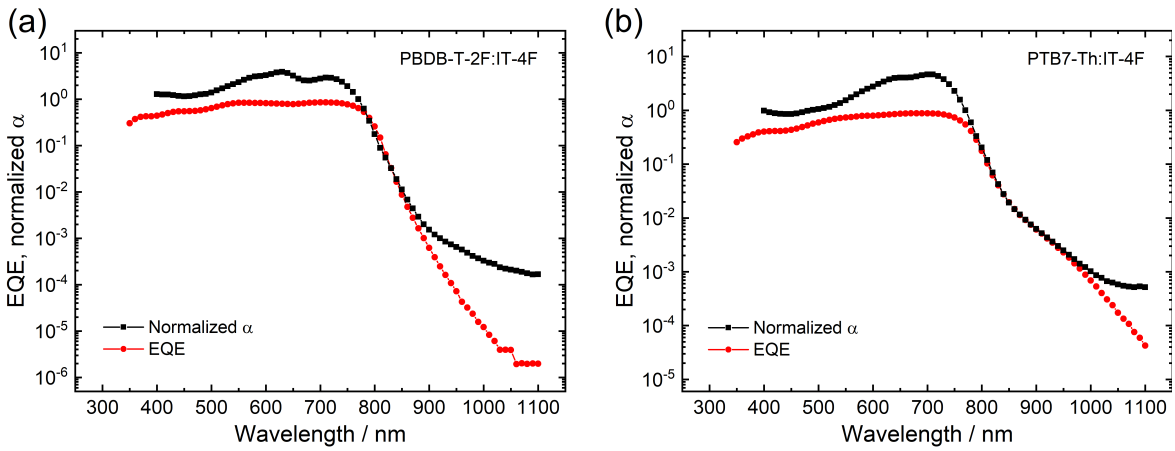

Figure 3.16. Comparison of the absorption coefficient spectra $\alpha(\lambda)$ of the donor-acceptor blends with the external quantum efficiency (EQE) spectra of corresponding organic solar cells for the materials **(a)** PBDB-T-2F:IT-4F and **(b)** PTB7-Th:IT-4F. The EQE spectra were obtained from ref. [148] and were measured on organic solar cells with an inverted architecture with the composition: glass substrate/ITO/ZnO/active layer/MoO_3/Ag. For better comparability, the $\alpha(\lambda)$ spectra were normalized to match the EQE(λ) spectra at the band edge.

in the sub-bandgap region and confirms that the weak absorption found for the wavelength region above ca. 900 nm stems mainly from optical transitions which do not contribute to the photocurrent generated in the OSC by incident light. In the EQE spectrum of PTB7-Th:IT-4F, displayed in Fig. 3.16 (b), the distinct and broad additional absorption shoulder, as observed in the absorption coefficient spectrum, is clearly visible and the two spectra show excellent agreement in the sub-bandgap spectral region, up to a wavelength of 970 nm where absorption from trap states appears to prevail in the $\alpha(\lambda)$ spectrum. This corroborates the assignment of this band to charge-transfer light absorption, as direct excitation of the charge-transfer state typically contributes to the measured photocurrent of the device [66, 75]. The excellent agreement of the $\alpha(\lambda)$ and EQE spectrum for PTB7-Th:IT-4F also suggest that the deposition of the layer via blade coating did not yield a significantly different blend morphology in comparison to spin coating, since a morphological change typically effects the D-A interfacial area, which has been reported to directly correlate with the CT absorption intensity [79]. For other D-A blends for BHJ OSCs, however, considerable morphology differences between blade coated and spin coated films have been reported [144] and would have to be considered for a comparison of the CT absorption.

Knowledge of the absorption coefficients of the donor-acceptor blends in the sub-bandgap region could be used in further studies for the modelling of the fraction of incident light absorbed in the active layer which would allow the determination of the internal quantum efficiency of the corresponding devices (see section 1.2.3.2) to gain insight into the efficiency of charge carrier generation and extraction [80, 83].

4. Conclusion

In this work, the assembly, optimization, basic characterization and validation of an experimental measurement setup for transverse photothermal deflection spectroscopy was carried out. The effect of different optimization measures, such as shielding of the setup from the environment and the influence of variable parameters such as the pump light modulation frequency of the setup, choice of deflection fluid and substrate for thin film samples on the setup performance were investigated. This allowed to identify an optimal set of parameters for the maximization of the signal-to-noise ratio while providing an unproblematic handling of the setup and to establish guidelines for the conduction of different measurement tasks and to identify possible pitfalls. Noise measurements and reference deflection measurements were carried out to quantify and compare the effects of a variation of the parameters on the setup. The correct functionality of the setup and data analysis procedure was verified by the very high conformity of an experimentally determined absorption coefficient spectrum of CuPc with reported spectra. Thus, a fully functional transverse PDS setup with a measurement sensitivity down to absorptance values of ca. 10^{-4} could be implemented. Furthermore, the assembled setup was used for the optical characterization of different organic-inorganic hybrid perovskite materials, as well as organic semiconductors.

PDS measurements on strongly luminescent $MAPbBr_3$ nanoparticle films and a film of a PS matrix doped with a perylene diimide derivative, demonstrated that the distortion of the deflection signal with respect to the absorptance or PLE spectrum due to photoluminescence could be successfully used for the determination of the photoluminescence quantum yield of investigated materials. The perovskite nanoparticle films showed very large mean quantum yields of 91.5 % up to 99.6 % for the as-prepared films and still impressive values of 71.4 % and 76.5 % after a considerable ageing time under atmospheric conditions. The results were verified by the generally good agreement with PLQY values determined on a commercial integrating sphere measurement system. The findings also suggest the potential use of PDS for the measurement of a wavelength-dependence of PLQY, as an apparent increase of the PL quantum yield at excitation wavelengths towards the band edge was indicated for the aged PNP films. However, a detailed quantification by the applied measurement methods requires further investigation and modifications of the underlying calculations.

The investigation of a $MAPbI_{3-x}Cl_x$ mixed-halide perovskite film showed the suitability of the built PDS setup for the sensitive measurement of the light absorption by states in the band tail of semiconductors and the determination of the Urbach energy which can yield valuable insight into the defects and disorder of the material which is a crucial parameter for its implementation in photovoltaic devices. For the investigated film of $MAPbI_{3-x}Cl_x$, a low Urbach energy of 15 meV and no measureable absorption above the PDS setup noise limit at wavelengths beyond the band tail were found, which suggest a very low extent of disorder and defects in the material.

Additionally, the PDS setup was employed for the spectroscopic investigation of donor-acceptor blend films of PBDB-T-2F:IT-4F, PBDB-T-2F:$PC_{71}BM$ and PTB7-Th:IT-4F, as well as the corre-

sponding pristine D/A components. In the absorption coefficient spectra of the PBDB-T-2F:$PC_{71}BM$ and PTB7-Th:IT-4F blends the occurence of an additonal weak absorption band at photon energies below the bandgap energies of the components was observed, which could not be explained as a superposition of the spectra of the pristine components. Thus, this band was attributed to the optical transitions of a charge-transfer state formed at the donor-acceptor interface in these blends. This assignment was supported by comparison of the sub-bandgap regions of the $\alpha(\lambda)$ spectra with the external quantum efficiency (EQE) spectra reported for bulk-heterojunction organic solar cells, which use the investigated blends PBDB-T-2F:IT-4F and PTB7-Th:IT-4F as active layers. An identical shape of $\alpha(\lambda)$ and EQE(λ) was observed for PTB7-Th:IT-4F, while PBDB-T-2F:IT-4F showed no distinct CT absorption in both spectra. While the CT absorption in the $\alpha(\lambda)$ and EQE(λ) spectra of PTB7-Th:IT-4F showed an identical shape, suggesting a similar morphology of the films prepared by blade coating and spin coating, the influence of the deposition technique and parameters must be generally considered for the comparison, as it can potentially have a significant impact on the donor-acceptor interfacial area and thus on the strength of the CT absorption.

Appendix

A.1. Theoretical Calculation of the Absorptance of a $MAPbI_3$ Film

The transmittance and reflectance at a certain wavelength λ of a film with the known complex refractive index $n' = n - ik$ and film thickness d on a substrate can be calculated according to the equations stated by Ritter and Weiser [116], as shown in eq. (A.1) and (A.2), upon neglecting the phase of the complex Fresnel coefficient for simplification analogous to ref. [115].

$$T = \frac{(1 - R_1)(1 - R_2)(1 + \frac{k^2}{n^2})}{e^{\alpha d} + R_1 R_2 e^{-\alpha d} - 2\sqrt{R_1 R_2}\cos(2\beta)} \tag{A.1}$$

$$R = \frac{R_1 e^{\alpha d} + R_2 e^{-\alpha d} - 2\sqrt{R_1 R_2}\cos(2\beta)}{e^{\alpha d} + R_1 R_2 e^{-\alpha d} - 2\sqrt{R_1 R_2}\cos(2\beta)} \tag{A.2}$$

Here, R_1 and R_2 represent the reflectances of the surrounding medium-film interface and the film-substrate interface, respectively, and can be calculated from refractive indices of surrounding medium, film and substrate via the Fresnel equation given in eq. (2.13) under assumption of normal angle of incidence of light [4]. α represents the absorption coefficient of the film and can be calculated from the imaginary part k of the refractive index of the material via eq. (1.5). β represents the phase angle given by [116]:

$$\beta = \frac{2\pi n d}{\lambda} \tag{A.3}$$

From T and R, the absorptance of the film can be calculated according to $A = 1 - T - R$. Additionally, it must be noted that equations (A.1) and (A.2) disregard reflections at the substrate-surrounding medium interface by assuming a semi-infinite substrate [115, 116], hence can only deliver a rough approximation to the real case of a film on a substrate with finite thickness.

For the theoretical calculation of the absorptance of films of methylammonium lead(II) iodide ($MAPbI_3$) with thicknesses of $d = 20$ nm and 500 nm on quartz and surrounded by air, literature data of n and k reported for $MAPbI_3$ [117] and n reported for quartz [100] were used. The corresponding wavelength-dependent refractive indices are shown in Fig. A.1 (a). For air, a constant refractive index of 1 in the wavelength range of 300 – 1500 nm was assumed. The absorptance, transmittance and reflectance of films with thicknesses of 20 nm and 500 nm calculated from the refractive indices via eqs. (A.1)–(A.3) are shown in Fig. A.1 (b).

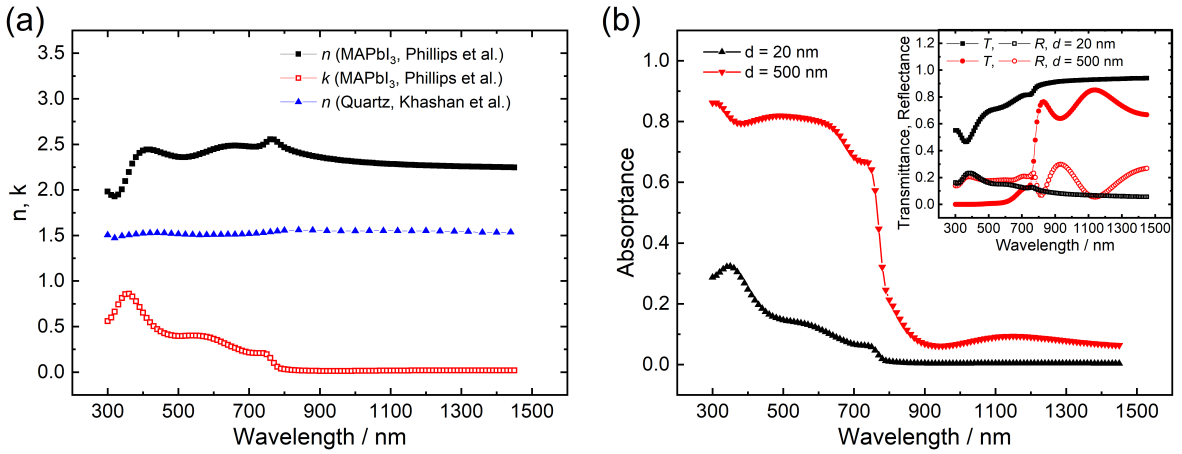

Figure A.1. (a) Spectra of the real and imaginary part of the refractive index of methylammonium lead(II) iodide ($MAPbI_3$) reported by Phillips *et al.* [117] and the real part of the refractive index of quartz reported by Khashan *et al.* [100]. **(b)** Absorptance spectra for films of $MAPbI_3$ with thicknesses of 20 nm (black curves) and 500 nm (red curves) on quartz in air, determined from transmittance and reflectance spectra calculated via equations (A.1)–(A.3) from the refractive index data shown in (a). The *inset* shows the calculated T and R spectra. All calculations were performed assuming light incidence normal to the film surface.

A.2. Determination of the Absorption Onset from Tauc Plot

The absorption onset (optical bandgap energy E_{og}) of a semiconductor material can be determined from its absorption coefficient α at the photon energy E according to the relation shown in eq. (A.4), where C is a constant and the value of ξ depends on the type of optical transition in the investigated material with $\xi = 2$ or 0.5 for direct or indirect transitions, respectively [149].

$$(\alpha\, E)^{\xi} = C\,(E - E_{\mathrm{og}}) \tag{A.4}$$

According to eq. (A.4), E_{og} can be determined by plotting $(\alpha\, E)^{\xi}$ versus the photon energy E (Tauc plot) and extrapolating the linear part of the plot at the absorption edge of the material to $(\alpha\, E)^{\xi} = 0$ to obtain the value of E_{og} on the E-axis [149].

A.2.1. Optical Bandgap Energies of Perovskite Films

Organic-inorganic hybrid perovskite semiconductors like $MAPbX_3$ (X = Cl, Br, I) are considered direct bandgap semiconductors, thus a value of $\xi = 2$ is typically used for the determination of the optical bandgap energy according to eq. (A.4) [150, 151]. Since the absorption coefficients of the PNP films investigated in this work (see Table 3.1) were not determined, the normalized photoluminescence excitation spectra of the films as shown in Fig. 3.7 were used for the approximation of the absorption onset. The Tauc plots for the investigated PNP films and the corresponding optical bandgap energies E_{og} are shown in Fig. A.2. For the determination of the optical bandgap of the $MAPbI_{3-x}Cl_x$ film on fused quartz the determined absorption coefficient spectrum was used (see section 3.3). The corresponding Tauc plot is shown in Fig. A.3.

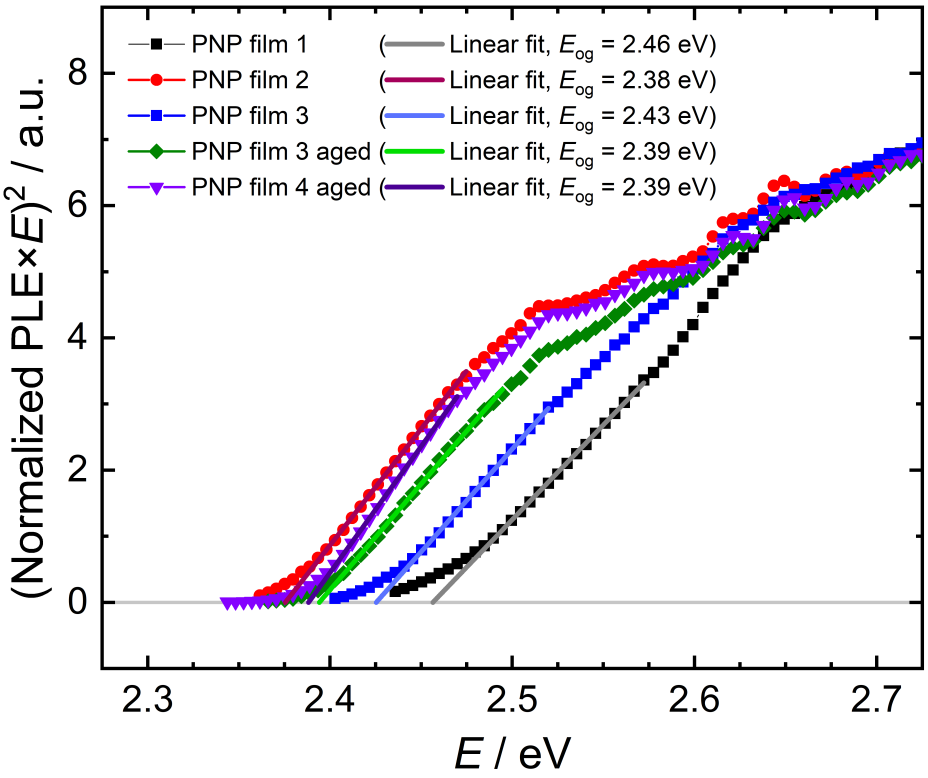

Figure A.2. Determination of the optical bandgap energy of the investigated $MAPbBr_3$ perovskite nanoparticle (PNP) films via a Tauc plot for a direct bandgap semiconductor according to equation (A.4) with $\xi = 2$, using the normalized PLE of the films as shown in Fig. 3.7 instead of the absorption coefficient α.

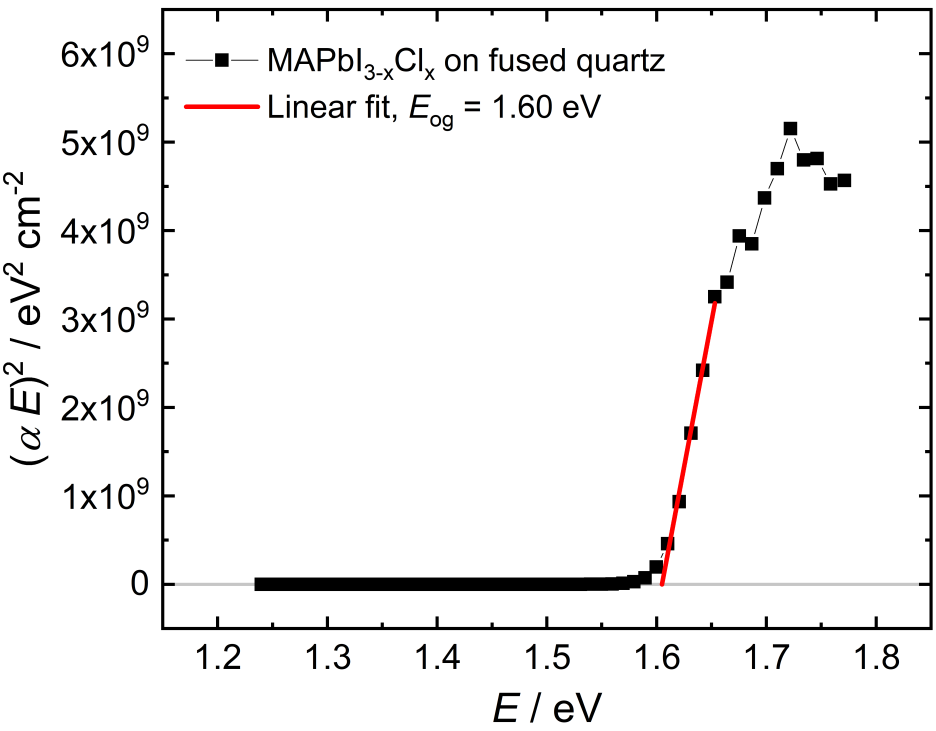

Figure A.3. Determination of the optical bandgap energy of the investigated $MAPbI_{3-x}Cl_x$ perovskite film via a Tauc plot for a direct bandgap semiconductor according to equation (A.4) with $\xi = 2$.

References

[1] S. J. Sweeney, J. Mukherjee in *Springer Handbook of Electronic and Photonic Materials*, (Eds.: S. Kasap, P. Capper), Springer Handbooks, Springer, Cham, **2017**, Chapter 35, pp. 897–932.

[2] J. Jimenez, J. W. Tomm, *Spectroscopic Analysis of Optoelectronic Semiconductors*, Springer, Basel, **2016**, pp. 1–76.

[3] J. Davis, C. Jagadish in *Optical Techniques for Solid-State Materials Characterization*, (Eds.: R. P. Prasankumar, A. J. Taylor), CRC Press, Boca Raton, **2012**, Chapter 2, pp. 39–78.

[4] H. Kuzmany, *Solid-State Spectroscopy*, Second edition, Springer, Heidelberg, **2009**, pp. 107–215, 473.

[5] W. J. Padilla in *Optical Techniques for Solid-State Materials Characterization*, (Eds.: R. P. Prasankumar, A. J. Taylor), CRC Press, Boca Raton, **2012**, Chapter 1, pp. 3–38.

[6] J. Räty, K. Peiponen, T. Asakura, *UV-Visible Reflection Spectroscopy of Liquids*, Springer, Berlin, **2004**, pp. 92–96.

[7] J. I. Pankove, *Optical Processes in Semiconductors*, Dover Publications, New York, **1971**, pp. 87–95.

[8] J. Jean, PhD thesis, Massachusetts Institute of Technology (Massachusetts), **2017**.

[9] A. Hordvik, *Appl. Opt.* **1977**, *16*, 2827–2833.

[10] M. Commandre, P. Roche, *Appl. Opt.* **1996**, *35*, 5021–5034.

[11] K. Meykens, PhD thesis, Limburgs Universitair Centrum (Belgium), **2000**.

[12] M. Nesladek, K. Meykens, L. M. Stals, *Phys. Rev. B* **1996**, *54*, 5552–5561.

[13] X. Bi, P. C. Eklund, J. G. Zhang, A. M. Rao, T. A. Perry, C. P. Beetz, *J. Mater. Res.* **1990**, *5*, 811–817.

[14] M. Commandre, P. J. Roche, G. Albrand, E. P. Pelletier, *Proc. SPIE* **1990**, *1270*, 82–93.

[15] B. Bohnert, W. Faubel, H. J. Ache, *Fresenius J. Anal. Chem.* **1992**, *343*, 513–517.

[16] W. B. Jackson, N. M. Amer, *Phys. Rev. B* **1982**, *25*, 5559–5562.

[17] N. M. Amer, W. B. Jackson in *Hydrogenated Amorphous Silicon*, (Ed.: J. I. Pankove), Semiconductors and Semimetals, Elsevier, London, **1984**, Chapter 3, pp. 83–112.

[18] M. B. Upama, M. Wright, B. Puthen-Veettil, N. K. Elumalai, M. A. Mahmud, D. Wang, K. H. Chan, C. Xu, F. Haque, A. Uddin, *RSC Adv.* **2016**, *6*, 103899–103904.

[19] L. Goris, K. Haenen, M. Nesladek, P. Wagner, D. Vanderzande, L. De Schepper, J. D'haen, L. Lutsen, J. V. Manca, *J. Mater. Sci.* **2005**, *40*, 1413–1418.

[20] S. E. Bialkowski, N. G. C. Astrath, M. A. Proskurnin, *Photothermal Spectroscopy Methods*, 2nd edition, Wiley, **2019**.

[21] J. K. Katahara, H. W. Hillhouse, *J. Appl. Phys.* **2014**, *116*, 173504.

[22] H. Perkampus, *UV-VIS Spectroscopy and Its Applications*, Springer, Berlin, **1992**, pp. 120–127.

[23] E. Daub, P. Würfel, *Phys. Rev. Lett.* **1995**, *74*, 1020–1023.

[24] C. Barugkin, J. Cong, T. Duong, S. Rahman, H. T. Nguyen, D. Macdonald, T. P. White, K. R. Catchpole, *J. Phys. Chem. Lett.* **2015**, *6*, 767–772.

[25] M. Righetto, S. S. Lim, D. Giovanni, J. W. M. Lim, Q. Zhang, S. Ramesh, Y. K. E. Tay, T. C. Sum, *Nat. Commun.* **2020**, *11*, 2712.

[26] S. J. Wawilow, *Z. Physik* **1927**, *42*, 3.

[27] S. E. Braslavsky, *Pure Appl. Chem.* **2007**, *79*, 293–465.

[28] W. B. Jackson, N. M. Amer, A. C. Boccara, D. Fournier, *Appl. Opt.* **1981**, *20*, 1333–1344.

[29] M. A. Proskurnin in *Laser Spectroscopy for Sensing: Fundamentals, Techniques and Applications*, (Ed.: M. Baudelet), Electronic and Optical Materials, Elsevier, **2014**, Chapter 11, pp. 313–361.

[30] A. C. Boccara, D. Fournier, J. Badoz, *Appl. Phys. Lett.* **1980**, *36*, 130–132.

[31] J. D. Spear, R. E. Russo, R. J. Silva, *Appl. Opt.* **1990**, *29*, 4225–4234.

[32] J. Fernández, A. Mendioroz, A. J. Garcia, R. Balda, J. L. Adam, *J. Alloys Compd.* **2001**, *323*, 239–244.

[33] W. Dickmann, J. Dickmann, F. F. Bruns, S. Kroker, *J. Appl. Phys.* **2019**, *126*, 025106.

[34] R. S. Fontenot, V. K. Mathur, J. H. Barkyoumb, *J. Quant. Spectrosc. Radiat. Transfer* **2018**, *204*, 1–6.

[35] D. Fournier, A. C. Boccara, N. M. Amer, R. Gerlach, *Appl. Phys. Lett.* **1980**, *37*, 519–521.

[36] B. Couch, A. Meyer, B. Heller, S. L. Johnson, *Methods Appl. Fluoresc.* **2019**, *7*, 015004.

[37] Q. E. Khuen, W. Faubel, H. J. Ache, *J. Phys. IV* **1994**, *4*, C7-361–364.

[38] M. A. Proskurnin, D. Korte, O. B. Rogova, D. S. Volkov, M. Franko, *Int. J. Thermophys.* **2018**, *39*, 81.

[39] M. Sumiya, K. Fukuda, S. Takashima, S. Ueda, T. Onuma, T. Yamaguchi, T. Honda, A. Uedono, *J. Cryst. Growth* **2019**, *511*, 15–18.

[40] M. Stella, M. Della Pirriera, J. Puigdollers, J. Bertomeu, C. Voz, J. Andreu, R. Alcubilla, *Mater. Res. Soc. Symp. Proc.* **2009**, *1154*, 45–50.

[41] A. Rosencwaig, A. Gersho, *J. Appl. Phys.* **1976**, *47*, 64–69.

[42] *CRC Handbook of Chemistry and Physics*, 97th edition, (Eds.: W. M. Haynes, D. R. Lide, T. J. Bruno), CRC Press, Boca Raton, **2017**, pp. 4-1–4-139.

[43] I. M. Abdulagatov, S. N. Emirov, T. A. Tsomaeva, K. A. Gairbekov, S. Y. Askerov, N. A. Magomedova, *J. Phys. Chem. Solids* **2000**, *61*, 779–787.

[44] V. V. Tarassov, *Phys. Stat. Sol.* **1967**, *20*, 37–43.

[45] G. S. Nolas, H. J. Goldsmid in *Thermal Conductivity*, (Ed.: T. M. Tritt), Physics of Solids and Liquids, Springer, **2004**, Chapter 1.4, pp. 105–121.

[46] S. Hiura, N. Okada, J. Wakui, H. Narita, S. Kanehashi, T. Shimomura, *Materials* **2017**, *10*, 468.

[47] J. C. Duda, P. E. Hopkins, Y. Shen, M. C. Gupta, *Appl. Phys. Lett.* **2013**, *102*, 251912.

[48] J. Pöhls, M. B. Johnson, M. A. White, *Phys. Chem. Chem. Phys.* **2016**, *18*, 1185–1190.

[49] C. C. Stoumpos, C. D. Malliakas, M. G. Kanatzidis, *Inorg. Chem.* **2013**, *52*, 9019–9038.

[50] R. Heiderhoff, T. Haeger, N. Pourdavoud, T. Hu, M. Al-Khafaji, A. Mayer, Y. Chen, H. Scheer, T. Riedl, *J. Phys. Chem. C* **2017**, *121*, 28306–28311.

[51] T. A. Tyson, W. Gao, Y. Chen, S. Ghose, Y. Yan, *Sci. Rep.* **2017**, *7*, 9401.

[52] J. D. Spear, R. E. Russo, *J. Appl. Phys.* **1991**, *70*, 580–586.

[53] W. B. Jackson, R. J. Nemanich, *J. Non-Cryst. Solids* **1983**, *59*, 353–356.

[54] E. V. Anslyn, D. A. Dougherty, *Modern Physical Organic Chemistry*, University Science Books, Sausalito, **2006**, pp. 945–953.

[55] A. Meeder, D. Fuertes Marron, A. Rumberg, M. C. Lux-Steiner, V. Chu, J. P. Conde, *J. Appl. Phys.* **2002**, *92*, 3016–3020.

[56] J. H. Werner, J. Mattheis, U. Rau, *Thin Solid Films* **2005**, *480–481*, 399–409.

[57] J. Jean, T. S. Mahony, D. Bozyigit, M. Sponseller, J. Holovsky, M. G. Bawendi, V. Bulovic, *ACS Energy Lett.* **2017**, *2*, 2616–2624.

[58] S. De Wolf, J. Holovsky, S. Moon, P. Löper, B. Niesen, M. Ledinsky, F. Haug, J. Yum, C. Ballif, *J. Phys. Chem. Lett.* **2014**, *5*, 1035–1039.

[59] L. Chahed, M. L. Theye, D. Fournier, J. P. Roger, A. C. Boccara, Y. M. Li, W. A. Turner, W. Paul, *Phys. Rev. B* **1991**, *43*, 14488–14497.

[60] S. Abroug, F. Saadallah, N. Yacoubi, *Phys. B Condens. Matter* **2007**, *400*, 163–167.

[61] U. Zammit, F. Gasparrini, M. Marinelli, R. Pizzoferrato, F. Scudieri, S. Martellucci, *Appl. Phys. A* **1991**, *52*, 112–114.

[62] T. Y. Leung, W. F. Man, S. K. So, P. K. Lim, W. C. Chan, F. Gaspari, S. Zukotynski, *J. Non-Cryst. Solids* **1999**, *254*, 151–155.

[63] P. Guyot-Sionnest, E. Lhuillier, H. Liu, *J. Chem. Phys.* **2012**, *137*, 154704–154709.

[64] C. H. Y. Ho, S. H. Cheung, H. Li, K. L. Chiu, Y. Cheng, H. Yin, M. H. Chan, F. So, S. Tsang, S. K. So, *Adv. Energy Mater.* **2017**, *7*, 1602360.

[65] T. Markvart, L. Castaner in *Practical Handbook of Photovoltaics: Fundamentals and Applications*, (Eds.: T. Markvart, L. Castaner), Elsevier, Oxford, **2003**, Chapter IIa-2, pp. 95–121.

[66] K. Vandewal, S. Albrecht, E. T. Hoke, K. R. Graham, J. Widmer, J. D. Douglas, M. Schubert, W. R. Mateker, J. T. Bloking, G. F. Burkhard, A. Sellinger, J. M. J. Frechet, A. Amassian, M. K. Riede, M. D. McGehee, D. Neher, A. Salleo, *Nat. Mater.* **2014**, *13*, 63–68.

[67] F. Kahle, A. Rudnick, H. Bässler, A. Köhler, *Mater. Horiz.* **2018**, *5*, 837–848.

[68] N. S. Sariciftci, L. Smilowitz, A. Heeger, F. Wudl, *Science* **1992**, *258*, 1474–1476.

[69] M. C. Scharber, N. S. Sariciftci, *Prog. Polym. Sci.* **2013**, *38*, 1929–1950.

[70] W. Yin, M. Dadmun, *ACS Nano* **2011**, *5*, 4756–4768.

[71] N. C. Miller, E. Cho, R. Gysel, C. Risko, V. Coropceanu, C. E. Miller, S. Sweetnam, A. Sellinger, M. Heeney, I. McCulloch, J. Bredas, M. F. Toney, M. D. McGehee, *Adv. Energy Mater.* **2012**, *2*, 1208–1217.

[72] C. Deibel, T. Strobel, V. Dyakonov, *Adv. Mater.* **2010**, *22*, 4097–4111.

[73] V. Coropceanu, X. Chen, T. Wang, Z. Zheng, J. Bredas, *Nat. Rev. Mater.* **2019**, *4*, 689–707.

[74] R. S. Mulliken, *J. Phys. Chem.* **1952**, *56*, 801–822.

[75] K. Vandewal, K. Tvingstedt, A. Gadisa, O. Inganäs, J. V. Manca, *Phys. Rev. B* **2010**, *81*, 125204.

[76] D. Becker-Koch, B. Rivkin, F. Paulus, H. Xiang, Y. Dong, Z. Chen, A. A. Bakulin, Y. Vaynzof, *J. Phys.: Condens. Matter* **2019**, *31*, 124001.

[77] K. Vandewal, *Annu. Rev. Phys. Chem.* **2016**, *67*, 113–113.

[78] J. J. Benson-Smith, L. Goris, K. Vandewal, K. Haenen, J. V. Manca, D. Vanderzande, D. D. C. Bradley, J. Nelson, *Adv. Funct. Mater.* **2007**, *17*, 451–457.

[79] E. Buchaca-Domingo, K. Vandewal, Z. Fei, S. E. Watkins, F. H. Scholes, J. H. Bannock, J. C. de Mello, L. J. Richter, D. M. DeLongchamp, A. Amassian, M. Heeney, A. Salleo, N. Stingelin, *J. Am. Chem. Soc.* **2015**, *137*, 5256–5259.

[80] C. Kaiser, S. Zeiske, P. Meredith, A. Armin, *Adv. Optical Mater.* **2020**, *8*, 1901542.

[81] C. H. Y. Ho, H. Cao, Y. Lu, T. Lau, S. Cheung, H. Li, H. Yin, K. L. Chiu, L. Ma, Y. Cheng, S. Tsang, X. Lu, S. K. So, B. S. Ong, *J. Mater. Chem. A* **2017**, *5*, 23662–23670.

[82] A. Weu, J. A. Kress, F. Paulus, D. Becker-Koch, V. Lami, A. A. Bakulin, Y. Vaynzof, *ACS Appl. Energy Mater.* **2019**, *2*, 1943–1950.

[83] A. Armin, M. Velusamy, P. Wolfer, Y. Zhang, P. L. Burn, P. Meredith, A. Pivrikas, *ACS Photonics* **2014**, *1*, 173–181.

[84] G. Dennler, K. Forberich, M. C. Scharber, C. J. Brabec, I. Tomis, K. Hingerl, T. Fromherz, *J. Appl. Phys.* **2007**, *102*, 054516.

[85] A. Loges, S. Herberger, D. Werner, T. Wetzel, *J. Power Sources* **2016**, *325*, 104–115.

[86] C. Wetzel, V. Petrova-Koch, F. Koch, D. Grützmacher, *Semicond. Sci. Technol.* **1990**, *5*, 702–706.

[87] A. F. S. Penna, J. Shah, A. E. DiGiovanni, A. Y. Cho, A. C. Gossard, *Appl. Phys. Lett.* **1985**, *47*, 591–593.

[88] J. D. Rudnicki, R. E. Russo, D. W. Shoesmith, *J. Electroanal. Chem.* **1994**, *372*, 63–74.

[89] B. Hailegnaw, G. Adam, D. Wielend, J. D. Pedarnig, N. S. Sariciftci, M. C. Scharber, *J. Phys. Chem. C* **2019**, *123*, 23807–23816.

[90] A. Jancik Prochazkova, Y. Salinas, C. Yumusak, M. C. Scharber, O. Brüggemann, M. Weiter, N. S. Sariciftci, J. Krajcovic, A. Kovalenko, *ACS Appl. Nano Mater.* **2020**, *3*, 1242–1249.

[91] M. S. Ahmed, PhD thesis, University of Western Ontario (Canada), **2013**.

[92] M. Elouneg-Jamroz, MA thesis, University of British Columbia (Canada), **2006**.

[93] J. H. Barkyoumb, PhD thesis, Dartmouth College (New Hampshire), **1988**.

[94] A. J. A. B. Seeley, PhD thesis, University of Cambridge (United Kingdom), **2003**.

[95] S. Martani, MA thesis, Polytechnic University of Milan (Italy), **2018**.

[96] C. E. Mungan, M. I. Buchwald, B. C. Edwards, R. I. Epstein, T. R. Gosnell, *Appl. Phys. Lett.* **1997**, *71*, 1458–1460.

[97] SuperK EXTREME/FIANIUM High Power Supercontinuum fiber laser series, NKT Photonics, Birkerød (Denmark), **2019**.

[98] Chemical and physical properties - Microscope slides made of soda lime glass 1 mm, Paul Marienfeld GmbH & Co. KG, Lauda-Königshofen (Germany), **2019**.

[99] C. Huang, X. Qian, R. Yang, *Mater. Sci. Eng. R* **2018**, *132*, 1–22.

[100] M. A. Khashan, A. Y. Nassif, *Opt. Commun.* **2001**, *188*, 129–139.

[101] 3M Fluorinert Electronic Liquid FC-72 Technical Data, 3M, St. Paul (Minnesota), **2019**.

[102] Flutec PP6 Data Sheet, F2 Chemicals, Preston (United Kingdom).

[103] Perfluoro-1,3-diethylcyclohexane Product Safety Information Sheet, F2 Chemicals, Preston (United Kingdom), **2018**.

[104] Flutec PP9 Product Safety Information Sheet, F2 Chemicals, Preston (United Kingdom), **2018**.

[105] Flutec PP10 Data Sheet, F2 Chemicals, Preston (United Kingdom).

[106] Flutec PP11 Data Sheet, F2 Chemicals, Preston (United Kingdom).

[107] Flutec PP24 Data Sheet, F2 Chemicals, Preston (United Kingdom).

[108] S. Ilahi, F. Saidi, R. Hamila, N. Yacoubi, L. Auvray, H. Maaref, *Curr. Appl. Phys.* **2013**, *13*, 610–613.

[109] D. Korte, H. Cabrera, J. Toro, P. Grima, C. Leal, A. Villabona, M. Franko, *Laser Phys. Lett.* **2016**, *13*, 125701–125712.

[110] S. Nonomura, H. Hayashi, S. Nitta, *Rev. Sci. Instrum.* **1989**, *60*, 657–660.

[111] Position-Sensing Detector PDQ80A Specification Sheet, Thorlabs, Newton (New Jersey), **2019**.

[112] R. A. Chipman, W. T. Lam, G. Young, *Polarized Light and Optical Systems*, CRC Press, Boca Raton, **2019**, pp. 295–321.

[113] J. N. Ross, *Opt. Quantum Electron.* **1984**, *16*, 455–461.

[114] W. Xiong, C. W. Hsu, Y. Bromberg, J. E. Antonio-Lopez, R. A. Correa, H. Cao, *Light: Sci. Appl.* **2018**, *7*, 54–63.

[115] K. Driss-Khodja, A. Gheorghiu, M.-L. Theye, *Opt. Commun.* **1985**, *55*, 169–173.

[116] D. Ritter, K. Weiser, *Opt. Commun.* **1986**, *57*, 336–338.

[117] L. J. Phillips, A. M. Rashed, R. E. Treharne, J. Kay, P. Yates, I. Z. Mitrovic, A. Weerakkody, S. Hall, K. Durose, *Data In Brief* **2015**, *5*, 926–928.

[118] M. Della Pirriera, J. Puigdollers, C. Voz, M. Stella, J. Bertomeu, R. Alcubilla, *J. Phys. D: Appl. Phys.* **2009**, *42*, 145102–145106.

[119] S. Ambily, C. S. Menon, *Thin Solid Films* **1999**, *347*, 284–288.

[120] F. T. Vasko, A. V. Kuznetsov, *Electronic States and Optical Transitions in Semiconductor Heterostructures*, Springer, New York, **1999**, pp. 159–162.

[121] B. Li, P. J. Brosseau, D. P. Strandell, T. G. Mack, P. Khambhampati, *J. Phys. Chem. C* **2019**.

[122] J. Mooney, P. Kambhampati, *J. Phys. Chem. Lett.* **2013**, *4*, 3316–3318.

[123] A. A. Serkov, H. V. Snelling, S. Heusing, T. Martins Amaral, *Sci. Rep.* **2019**, *9*, 1773–1781.

[124] J. Luo, D. Billep, T. Waechtler, T. Otto, M. Toader, G. Ovidiu, E. Sheremet, J. Martin, M. Hietschold, D. R. T. Zahn, T. Gessner, *J. Mater. Chem. A* **2013**, *1*, 7576–7583.

[125] Z. T. Liu, H. S. Kwok, A. B. Djurisic, *J. Phys. D: Appl. Phys.* **2004**, *37*, 678–688.

[126] K. Tanaka, T. Takahashi, T. Ban, T. Kondo, U. Kazuhito, N. Miura, *Solid State Commun.* **2003**, *127*, 619–623.

[127] I. Pelant, J. Valenta, *Luminescence Spectroscopy of Semiconductors*, Oxford University Press, Oxford, **2012**, pp. 339–378.

[128] L. Polavarapu, B. Nickel, J. Feldmann, A. S. Urban, *Adv. Energy Mater.* **2017**, *7*, 1700267.

[129] S. Bonabi Naghadeh, S. Sarang, A. Brewer, A. Allen, Y. Chiu, Y. Hsu, J. Wu, S. Ghosh, J. Z. Zhang, *J. Chem. Phys.* **2019**, *151*, 154705.

[130] L. C. Schmidt, A. Pertegas, S. Gonzalez-Carrero, O. Malinkiewicz, S. Agouram, G. Minguez Espallargas, H. J. Bolink, R. E. Galian, J. Perez-Prieto, *J. Am. Chem. Soc.* **2014**, *136*, 850–853.

[131] C. Würth, C. Lochmann, M. Spieles, J. Pauli, K. Hoffmann, T. Schüttrigkeit, T. Franzl, U. Resch-Genger, *Appl. Spectrosc.* **2010**, *64*, 733–741.

[132] J. Hoy, P. J. Morrison, L. K. Steinberg, W. E. Buhro, R. A. Loomis, *J. Phys. Chem. lett.* **2013**, *4*, 2053–2060.

[133] W. M. Sanderson, J. Hoy, C. Morrison, F. Wang, Y. Wang, P. J. Morrison, W. E. Buhro, R. A. Loomis, *J. Phys. Chem. Lett.* **2020**, *11*, 3249–3256.

[134] W. Hoheisel, V. L. Colvin, C. S. Johnson, A. P. Alivisatos, *J. Chem. Phys.* **1994**, *101*, 8455.

[135] D. Timmerman, J. Valenta, K. Dohnalova, W. D. A. M. de Boer, T. Gregorkiewicz, *Nat. Nanotechnol.* **2011**, *6*, 710–713.

[136] I. V. Martynenko, A. S. Baimuratov, V. A. Osipova, V. A. Kuznetsova, F. Purcell-Milton, I. D. Rukhlenko, A. V. Fedorov, Y. K. Gun'ko, U. Resch-Genger, A. V. Baranov, *Chem. Mater.* **2018**, *30*, 465–471.

[137] B. Zhang, H. Soleimaninejad, D. J. Jones, J. M. White, K. P. Ghiggino, T. A. Smith, W. W. H. Wong, *Chem. Mater.* **2017**, *29*, 8395–8403.

[138] A. Miasojedovas, K. Kazlauskas, G. Armonaite, V. Sivamurugan, S. Valiyaveettil, J. V. Grazulevicius, S. Jursenas, *Dyes Pigm.* **2012**, *92*, 1285–1291.

[139] R. Hu, X. Su, H. Liu, Y. Liu, M. Huo, W. Zhang, *J. Mater. Sci.* **2020**, *55*, 11403–11410.

[140] Q. Wan, X. Guo, Z. Wang, W. Li, B. Guo, W. Ma, M. Zhang, Y. Li, *Adv. Funct. Mater.* **2016**, *26*, 6635–6640.

[141] X. Dong, P. Shi, L. Sun, J. Li, F. Qin, S. Xiong, T. Liu, X. Jiang, Y. Zhou, *J. Mater. Chem. A* **2019**, *7*, 1989–1995.

[142] K. Weng, L. Ye, L. Zhu, J. Xu, J. Zhou, X. Feng, G. Lu, S. Tan, F. Liu, Y. Sun, *Nat. Commun.* **2020**, *11*, 2855.

[143] G. Li, V. Shrotriya, J. Huang, Y. Yao, T. Moriarty, K. Emery, Y. Yang, *Nat. Mater.* **2005**, *4*, 864–868.

[144] J. Chang, Y. Chen, H. Lin, Y. Lin, H. Meng, E. Chen, *Org. Electron.* **2012**, *13*, 705–709.

[145] Y. L. Lin, M. A. Fusella, B. P. Rand, *Adv. Energy Mater.* **2018**, *8*, 1702816.

[146] X. Chen, V. Coropceanu, J. Bredas, *Nat. Commun.* **2018**, *9*, 5295.

[147] A. E. Mansour, D. Lungwitz, T. Schultz, M. Arvind, A. M. Valencia, C. Cocchi, A. Opitz, D. Neher, N. Koch, *J. Mater. Chem. C.* **2020**, *8*, 2870.

[148] C. Putz, MA thesis, Johannes Kepler University Linz (Austria), **in preparation**.

[149] M. B. Hernandez, M. A. Garcia-Ramirez, Y. Dan, J. A. Aguilar-Martinez, B. Krishnan, S. Shaji in *Semiconductors: Synthesis, Properties and Applications*, (Eds.: M. I. Pech-Canul, N. M. Ravindra), Springer, Cham, **2019**, Chapter 3, pp. 102–105.

[150] I. E. Castelli, J. M. Garcia-Lastra, K. S. Thygesen, K. W. Jacobsen, *APL Mater.* **2014**, *2*, 081514.

[151] L. Kong, G. Liu, J. Gong, Q. Hu, R. D. Schaller, P. Dera, D. Zhang, Z. Liu, W. Yang, K. Zhu, Y. Tang, C. Wang, S. Wei, T. Xu, H. Mao, *Proc. Natl. Acad. Sci. U. S. A.* **2016**, *113*, 8910–8915.